9-16-2016

Robust Algorithms for Unattended Monitoring of Cardiovascular Health

Nicholas J. Conn
nxc9827@rit.edu

Recommended Citation

Conn, Nicholas J., "Robust Algorithms for Unattended Monitoring of Cardiovascular Health" (2016). Thesis. Rochester Institute of Technology. Accessed from

R·I·T

Robust Algorithms for Unattended Monitoring of Cardiovascular Health

by

Nicholas J. Conn

A dissertation submitted in partial fulfillment of the requirements
for the degree of Doctorate of Philosophy in Microsystems Engineering

Microsystems Engineering Program
Kate Gleason College of Engineering

Rochester Institute of Technology
Rochester, New York
September 16, 2016

Robust Algorithms for Unattended Monitoring of Cardiovascular Health

by

Nicholas J. Conn

Committee Approval:

We, the undersigned committee members, certify that we have advised and/or supervised the candidate on the work described in this dissertation. We further certify that we have reviewed the dissertation manuscript and approve it in partial fulfillment of the requirements of the degree of Doctor of Philosophy in Microsystems Engineering.

David A. Borkholder, PhD Date
Bausch and Lomb Professor, Microsystems Engineering

Karl Q. Schwarz, MD Date
Director, Echocardiography Laboratory, University of Rochester Medical Center

---

Daniel B. Phillips, PhD Date
Associate Professor, Electrical and Microelectronic Engineering

---

Raymond W. Ptucha, PhD Date
Assistant Professor, Computer Engineering

Certified by:

Bruce W. Smith, PhD Date
Director, Microsystems Engineering

Doreen D. Edwards, PhD Date
Dean, Kate Gleason College of Engineering

ABSTRACT

Kate Gleason College of Engineering
Rochester Institute of Technology

Degree: Doctor of Philosophy **Program:** Microsystems Engineering
Author: Nicholas J. Conn
Advisor: David A. Borkholder

Dissertation Title: Robust Algorithms for Unattended Monitoring of Cardiovascular Health

Cardiovascular disease is the leading cause of death in the United States. Tracking daily changes in one's cardiovascular health can be critical in diagnosing and managing cardiovascular disease, such as heart failure and hypertension. A toilet seat is the ideal device for monitoring parameters relating to a subject's cardiac health in his or her home, because it is used consistently and requires no change in daily habit. The present work demonstrates the ability to accurately capture clinically relevant ECG metrics, pulse transit time based blood pressures, and other parameters across subjects and physiological states using a toilet seat-based cardiovascular monitoring system, enabled through advanced signal processing algorithms and techniques. The algorithms described herein have been designed for use with noisy physiologic signals measured at non-standard locations. A key component of these algorithms is the classification of signal quality, which allows automatic rejection of noisy segments before feature delineation and interval extractions. The present delineation algorithms have been designed to work on poor quality signals while maintaining the highest possible temporal resolution. When validated on standard databases, the custom QRS delineation algorithm has best-in-class sensitivity and precision, while the photoplethysmogram delineation algorithm has best-in-class temporal resolution. Human subject testing on normative and heart failure subjects is used to evaluate the efficacy of the proposed monitoring system and algorithms. Results show that the accuracy of the measured heart rate and blood pressure are well within the limits of AAMI standards. For the first time, a single device is capable of monitoring long-term trends in these parameters while facilitating daily measurements that are taken at rest, prior to the consumption of food and stimulants, and at consistent times each day. This system has the potential to revolutionize in-home cardiovascular monitoring.

I can do all things through Christ who strengthens me.

Philippians 4:13

Acknowledgments

To my wife Amanda, thank you for your unconditional love and support. Thank you for always believing in me and always trusting me. Thank you for keeping me calm, no matter what stresses my PhD studies brought. In my deepest ruts, your insights and help allowed me to overcome every single challenge that I have faced. I especially thank you for your patience throughout the course of my PhD and your willingness to stay by my side and support me throughout all of the adventures life has and will throw at us.

To my parents, for instilling in me at an early age that I am capable of anything and that nothing is out of reach. Thank you for teaching me integrity and the core values that I live my life by, and for always encouraging my God given talents. Knowing that I can never disappoint you and that you will always love me, has given me the confidence to take the kind of risks that allow me to achieve such great things. This is just as much your PhD, as it is mine.

To John and Debbie for always supporting both Amanda and I throughout the course of my PhD. Thank you for always being there and for treating me like your own son.

To Dave, my advisor. I would not have pursued a PhD had it not been for you. I could not imagine having any other advisor in the whole world. The opportunities and experiences you have given me over these years have set the stage for my entire career. I thank you reinforcing what I was taught as a child, which is to always have pride in your work and to always give it your best. It would be truly impossible for me to list out of all the things that I have learned from you. I especially thank you for treating me as an equal, even though I often did not deserve to be treated as such. I would not be where I am today without your guidance and support. You have given me such amazing opportunities, for which I will be forever grateful. I look forward to sharing my professional future and career with you, as a lifelong friend.

To Karl, thank you for your tireless work on and passion for the FIT seat. Thank you for always having my back, no matter what kind of sticky situation we found ourselves in. Thank you for always keeping things light hearted throughout the course of our research, no matter how much of it ended up in the toilet. Also, thank you for providing your medical expertise, without which, my research would be severely lacking and not of the same caliber. Your insights and helped guide the course of my research. For all of this, I sincerely thank you.

To Dr. Phillips, thank you for being a constant role model and support figure throughout my entire time at RIT. You helped foster the love I have for my field as my professor, senior design advisor, and friend. Much of the knowledge I leveraged throughout the course of my PhD research came from the classes you taught during my undergraduate degree.

I would like to also thank Jennifer for truly believing in my work and for being always available and willing to lend your imaging expertise during the course subject testing. Thank you Marie for playing such a key role in seat assembly, and for not being afraid to get your hands dirty. Additionally, I would like to thank Kim and Dean for their industry design and mechanical expertise, without which, the seat would not be what it is today. Thank you to all of the co-ops and students who have worked in the Borkholder Lab, for augmenting my work and aiding in my research.

Finally, I would like to thank my entire committee, my department, and Lisa Zimmerman. It has been a pleasure to be part of the microsystems department. As the final chapter of my time at RIT comes to a close, I could not be more grateful for all that I have experienced and learned.

Contents

List of Figures

List of Tables

Chapter 1

Introduction

1.1 Cardiovascular Disease

Cardiovascular disease (CVD) is the leading cause of death both in the United States (US) and internationally. CVD consists of many diseases that impact the structure or function of the heart, including heart failure, coronary artery disease, heart attack, heart arrhythmias, vascular disease, and many more. It accounted for over 30% of all reported deaths in the US in 2011. Cardiovascular disease is expected to remain the single leading cause of death internationally, and it is expected to reach 23.3 million deaths a year by 2030 [1]. The direct costs associated with cardiovascular disease is expected to rise to over $1.2 trillion a year in the US by 2030, detailed in Figure 1.1 [2].

There are currently many challenges with detecting, diagnosing, and managing cardiovascular disease. It is very common for cardiovascular disease to be detected well after

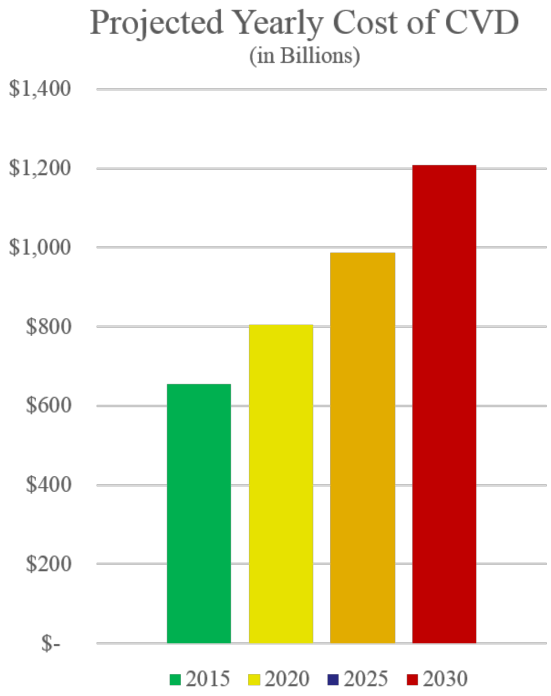

Figure 1.1: Direct medical costs associated with CVD in the US are expected to continually increase from $656 billion a year in 2015 [2].

the initial onset of the disease. Diagnosis often requires many doctor and hospital visits, a stress test, and an echocardiogram, which results in delayed diagnosis and large direct costs. By the time a subject is diagnosed with cardiovascular disease they may require an implantable cardiac device, such as a pacemaker, an implantable cardiac defibrillator, a stent, or a ventricular assist device.

Once a subject has been diagnosed with cardiovascular disease, there can be significant cost associated with continued care. The Centers for Medicare and Medicaid Services (CMS) makes a single, prospectively determined bundled payment to the hospital that encompasses all services furnished by the hospital, physicians, and other practitioners during the episode of care, which lasts the entire inpatient stay [3] for a single heart failure subject. This payment includes all hospital and professional services for 90 days after the index admission. The hospital has a loss if it spends more than the bundled payment. The program is currently voluntary, but will eventually be required and associated with penalties for non-compliance nation wide.

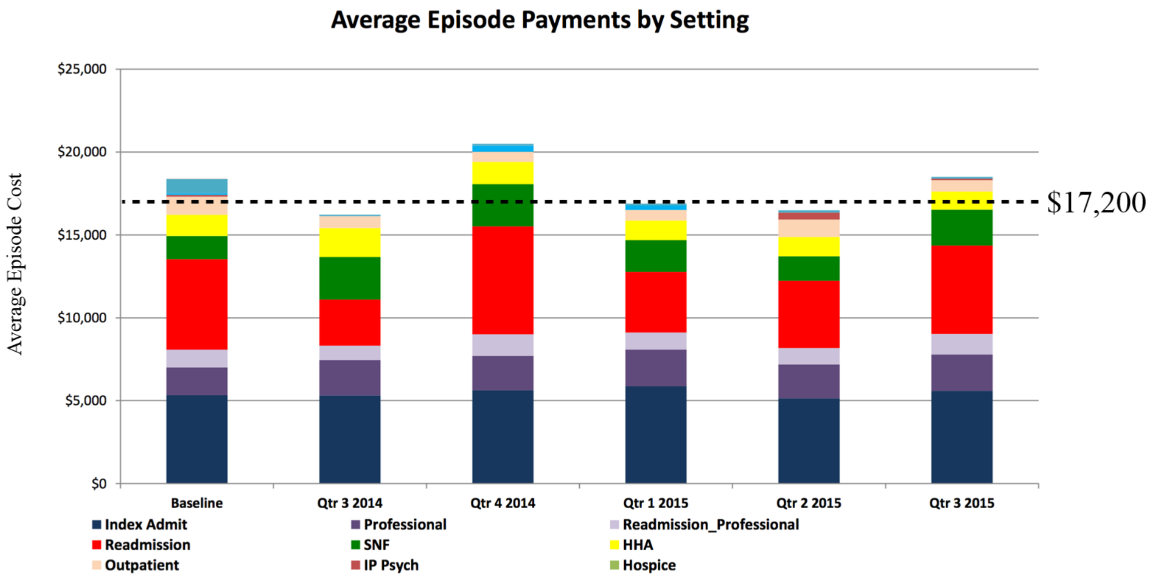

Figure 1.2: The costs per setting for heart failure subjects is often greater than the bundled payment provided by the Centers for Medicare and Medicaid Services. This data indicates that readmission is often the largest percentage of costs per patient. Courtesy of Karl Q. Schwarz, MD.

In a real life example, the predetermined bundled payment for the University of Rochester Medical Center is $17,200 per patient. The average episode cost for five fiscal quarters is compared to the CMS bundled rate in Figure 1.2. Readmission is the most important cost, sometimes exceeding the index admission. Readmission rates for heart failure patients are 7.5% within the first 7 days after discharge and 28% after the first 30 days. 90% of readmission is due to either patient non-compliance, medical management issues, or disease exacerbation as illustrated in Figure 1.3. Consistent monitoring of these subjects is required to ensure a subject’s health is not declining.

As an example, when a subject is diagnosed with heart failure they must track their weight and blood pressure daily in order to keep monitor of their cardiac health. Despite a subject’s best intentions patient compliance can be very low, which can significantly reduce the

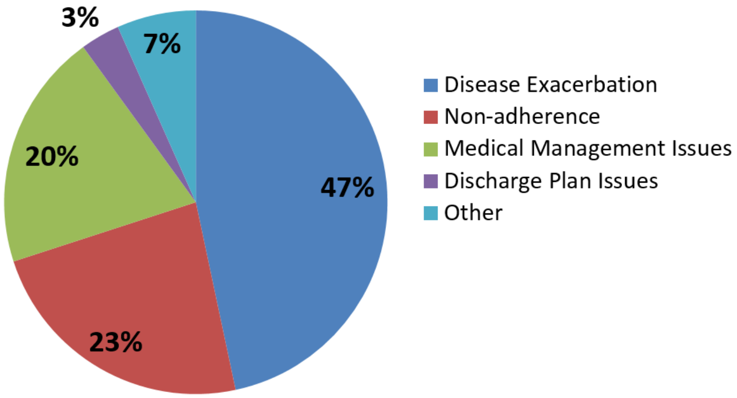

Figure 1.3: Readmission statistics for the University or Rochester Medical Center indicate that 90% of readmissions are due to non-compliance, management issues, or disease exacerbation. Courtesy of Karl Q. Schwarz, MD.

chances of recovery and add to costs associated with continued disease management [4]. Patient compliance is the extent to which a patient or subject consistently and accurately follows medically relevant instructions. Any lapse in diligence results in unreliable data with reduced clinical value. Something as simple as eating before measuring blood pressure in the morning can result in drastically inconsistent blood pressures.

1.2 Opportunities for In-Home Trend Monitoring

There are many devices that a subject can use to monitor their cardiac health in the home. The two most prevalent devices are a blood pressure monitor and a bathroom scale, both of which heart failure patients should use on a daily basis. The blood pressure monitor determines an individual's systolic and diastolic blood pressure, providing insights into cardiac function and overall cardiovascular health. Similarly, tracking a subject's weight over time is extremely important for heart failure patients, as a sharp increase in weight can indicate water retention and deteriorating condition.

Blood pressure and weight can change drastically throughout the day as a subject eats, drinks caffeine, smokes, exercises, or becomes stressed, confounding trend analysis. If blood pressure and weight are only monitored at the hospital or during doctor visits, important trends could easily be obscured by the natural variation of these parameters throughout the day.

Another medical device often used for in-home cardiovascular monitoring is a Holter monitor, which is an ambulatory electrocardiogram that is typically worn for short period of time as prescribed by a physician. Holter monitors are worn for 24, 48, 72 hours etc., up to a total of 7 days, and are not practical for long-term use [5, 6]. Typically, it is used for at least 24 hours in order to determine if a subject has any arrhythmias throughout the day or night. It can also allow a cardiologist to determine if a certain medication is working effectively [7]. While a Holter monitor can provide invaluable information about a subject's cardiac health for a short period, it can be uncomfortable and very disruptive to a subject's lifestyle.

Alternately, the single lead ECG can play an important role in the diagnosis and management of cardiovascular disease. The ECG is clinically important because it is used to diagnose myocardial ischemia and infarction, atrial fibrillation, left ventricular hypertrophy/dilatation, left bundle branch block and intraventricular conduction delays, and left atrial abnormality [8]. These disease states can be diagnosed by monitoring rhythm and morphology changes in a single lead ECG. Daily, long-term monitoring of a single lead ECG has the potential to augment the type of information provided by a Holter monitor and if done correctly, can increase the quality of life for subjects.

The following example highlights the need for accurate in-home monitoring:

Subjects that are diagnosed with heart failure are often required to measure their weight every day as rapid weight gain due to water retention can signify a further decline in ones cardiovascular health. The data shown in Figure 1.4 provides an example of a subject's daily weight immediately before he was diagnosed with heart failure [9]. From July to October the subject did their best to be active and lose weight, as can be seen by their steady weight loss throughout these months.

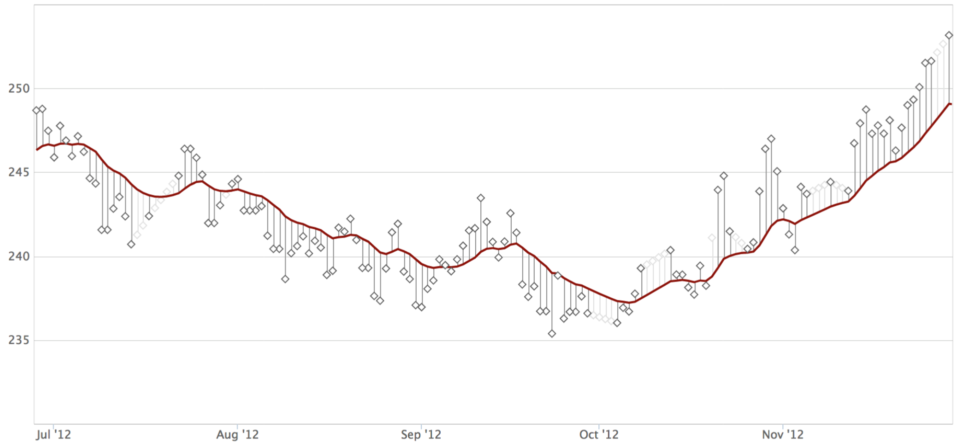

Figure 1.4: Daily weight measurements from a subject before and after being diagnosed with heart failure. Unexpected and rapid weight gain can indicate water retention, and thus heart failure [9].

Having changed nothing about their daily routine, the subject had two months of rapid weight gain starting in October. This prompted the subject to see a cardiologist, where he was then diagnosed with heart failure. This diagnosis may not have been made for many months if the subject was not tracking his weight. Imagine if the subject did not track their weight and only went to the doctor in July and November. The doctor would have only seen a weight gain of 10 pounds, which could be considered normal and could have been easily overlooked.

Many subjects wait until they have chest pain or issues during exercise before being examined by a cardiologist. By the time it would be diagnosed, the subject's heart failure could have progressed to the point that it could no longer be managed with medication, poten-

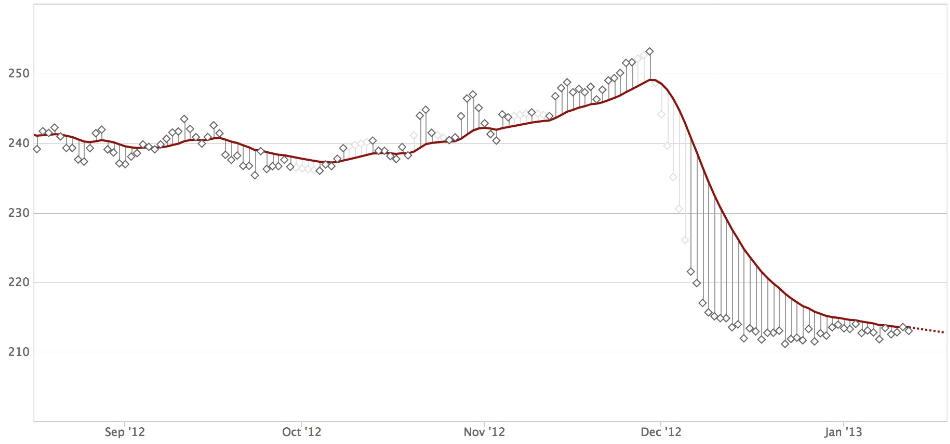

Figure 1.5: After being put on medication for heart failure and water retention, the subject looses the excess water weight very quickly [9].

tially requiring a transplant, an implantable cardiac device, or a more invasive type of heart surgery. Once this subject was given medication for heart failure, he lost approximately 40 pounds of water in the course of a month, as shown in Figure 1.5.

> *"The good news is that with just some medications, all this extra retained water drained off quickly, my symptoms disappeared, and I am back to feeling "normal" and have a normal level of physical activity including daily exercise." - Erv Walter [9]*

This is a remarkable example of how trends in a physiological signal can indicate a serious medical condition that could be missed if not monitored daily. Not all subjects are as diligent as the one depicted in this example, highlighting the need for inconspicuous daily medical monitoring.

1.3 An Ideal System for In-Home Monitoring

Each of the aforementioned devices have one thing in common: they either require a doctors visit or require the subject to change their daily habits when monitoring their health. Even if expensive connected versions of these devices are purchased, the subject must still take the time every day to perform the measurement at the correct time of day. This makes it difficult for physicians to monitor a subject remotely, where trends and patterns in a subject's measurements could indicate an improvement or a decline in health.

By integrating multiple medical instruments into a toilet seat, many of the challenges associated with in-home monitoring are addressed. The resulting cardiovascular monitoring system can be integrated into the natural routine of a subject, enabling measurements to be taken at the same time of the day before any stimulants (e.g., sugar, caffeine, nicotine) or food. This results in a stable daily measurement over time that is critical for accurate trend analysis. Issues with preparation and subject error are greatly reduced, since skin contact is automatic and has sufficient pressure to create a consistent electrode interface at a consistent location for each individual.

The fully integrated toilet (FIT) seat incorporates a single-lead electrocardiogram (ECG) for measuring the electrical activity of the heart, a photoplethysmogram (PPG) for measuring blood oxygenation and for estimating blood pressure, a ballistocardiogram (BCG) for measuring cardiac function and for estimating blood pressure, and a body weight sensor that can replace the bathroom scale (Figure 1.6). It is completely self contained, battery powered, wireless, and cleanable with all of the sensors and instrumentation integrated inside of the seat to facilitate user acceptance.

In-home physiological monitoring of all kinds (e.g., heart rate, blood pressure, weight)

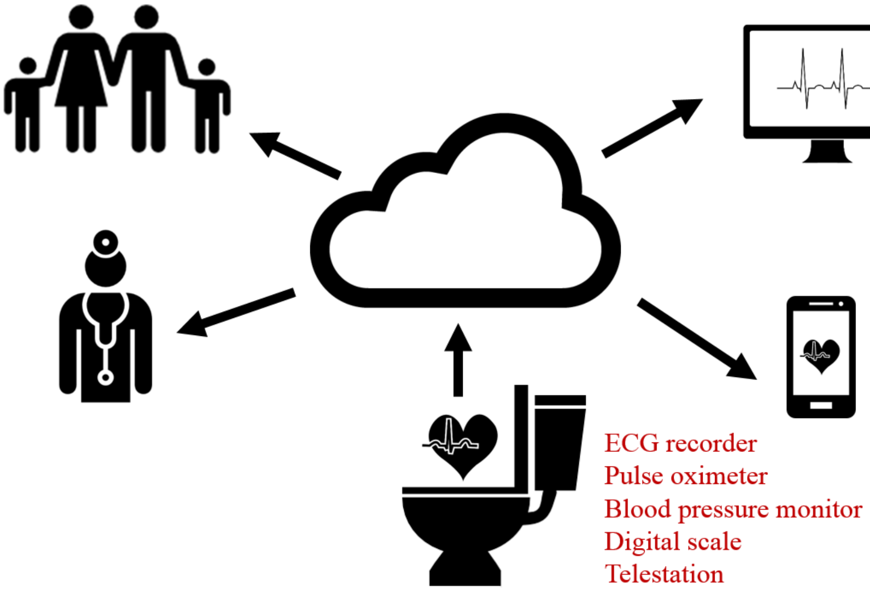

Figure 1.6: The final in-home version of the FIT seat is completely self-contained and will work on any standard toilet seat.

presents unique challenges that are not present in a hospital environment or doctor's office. A trained expert is not on hand to make any real-time changes that would ensure correct electrode placement, signal integrity, and measurement accuracy. Additionally, patient compliance is often very low resulting in measurements that are not taken consistently nor at a consistent physiologic state, which is a requirement for accurate trend analysis. Compliance is hampered if the in-home device is not easy to use or if a significant change of habit is required.

The key to successful cardiac monitoring and the early detection of changes associated with emerging or deteriorating health conditions is ensuring patient compliance, daily measurements, and a consistent physiological state at the time of measurement. Additionally, many medical devices such as the ECG require skin contact to achieve robust measurements and to ensure that the fine features of the waveform are accurately captured.

An integrated toilet seat is proposed as an ideal device for inconspicuous daily cardiovascular monitoring. This seat contains multiple sensors and microprocessors with wireless communication capabilities, providing a fully self-contained bioinstrumentation system that automatically captures medically relevant data on a daily basis.

Such a system is beneficial since many individuals will go to the bathroom in the morning before eating breakfast, having coffee, smoking a cigarette, and before any physical activity. This is the ideal time to take physiological measurements due to the known physiological state and consistent nature of the use of this device. Furthermore, patient compliance is automatic since subjects do not need to change their daily habits when using this device. A commercially available version of the FIT seat is expected to operate unattended and have multiple years of battery life, increasing the chance of user adoption. There are no special installation instructions since the FIT seat can be installed in the same manner as a regular toilet seat.

The extraction of accurate medical parameters from the FIT seat would not be possible without the custom algorithms presented herein. The present algorithms are the major contribution of this work, since there is a lack of robust algorithms in the current body of knowledge for working with non-ideal, noisy physiologic signals captured in the home. These algorithms allow the system to function with no interaction from the subject and allow it to seamlessly integrate into their daily life. This will facilitate the daily cardiac monitoring of subjects at a consistent physiological state, as required for accurate long-term trend analysis.

1.4 Research Overview

The outcome of this research is intended to be advanced custom algorithms that enable true, daily in-home monitoring of cardiovascular health, utilizing a completely self-contained unconventional cardiovascular monitoring system. The main contribution of this work is the development of automated algorithms for use with unconventional, noisy physiologic signals. Novel approaches will be used to rejection noisy sections of waveforms before analysis, specifically designed to recognize in-band noise. Delineation algorithms will be designed from the ground up with a focus on temporal resolution and ability to perform well on real-world signals, specifically with a dry electrode based ECG.

The monitoring system and custom algorithms have been designed and verified using data captured from two rounds of institute review board approved human subject testing both at the Rochester Institute of Technology and the University of Rochester Medical Center. Initial verification of blood pressure trend data from a seat deployed in the home is also presented.

Background theory on the cardiovascular system and medical instrumentation is discussed in Chapter 2 in order to provide the necessary information to understand the fully integrated toilet seat system, which is presented in Chapter 3. The algorithms and signal processing techniques that have been developed for use with noisy in-home data is discussed in Chapter 4. The structure of both human subject studies are discussed in Chapter 5, while the results for each medical instrument are presented in Chapter 6, and Chapter 7. True sub-Nyquist compressed sensing is discussed in Chapter 8, before outlining suggested future work that would leverage the systems and processes developed herein.

This work paves the way for future studies that would investigate the clinical utility of the FIT seat for heart failure subjects and the ability of a deployed, self-contained, toilet seat based system and algorithms to monitor long-term trends in the home. Such a device has the potential to capture long-term trend data that has been previously unattainable, as it facilitates daily measurements taken at rest prior to food and stimulants (e.g., caffeine, nicotine) at consistent times each day, with no required change in habit. This, in combination with intra-day circadian trends will enable new approaches and capabilities in the diagnosis and treatment of cardiovascular disease for those with heart failure, hypertension, and those undergoing chemotherapy treatments.

Chapter 2

Cardiac Theory and Physiological Signals

2.1 Introduction

This chapter provides all necessary background on the cardiovascular system and the medical instrumentation used during the diagnosis and management of cardiovascular disease, within the scope of the present work. Specifically, background and device theory for the electrocardiogram (ECG), the photoplethysmogram (PPG), and the ballistocardiogram (BCG) are provided, as each of these instruments have been embedded within the fully integrated toilet seat.

2.2 The Cardiovascular System

The cardiovascular system, also known as the circulatory system, is responsible for pumping blood throughout the body. The heart is at the center of the cardiovascular system and pumps blood through the vascular system, which consisting of arteries that bring oxygenated blood to tissue and veins that bring blood back to the heart. The heart can be thought of as two electrically controlled mechanical pumps, which consists of four chambers: two atria and two ventricles. The smaller right ventricle (RV) pumps blood to the lungs and the larger left ventricle (LV) pumps blood to the rest of the body. This can be seen in Figure 2.1.

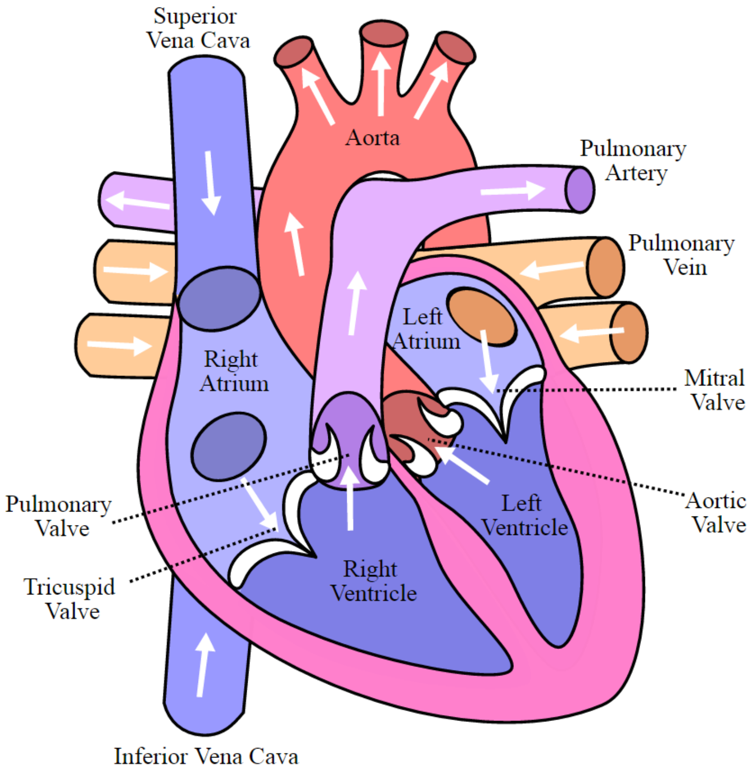

Figure 2.1: The four chambers of the heart are shown. The right atria pumps deoxygenated blood into the lungs and the left ventricle pumps oxygenated blood into the body through the aorta [10].

At the start of systole, the left ventricle begins to contract causing the aortic valve (AV) to open, causing blood to be ejected from the left ventricle into the aorta through the left ventricular outflow tract (LVOT). The resulting pulse wave propagates upward to the aortic arch, changing directions to continue down the torso through the descending aorta, which is shown in Figure 2.2. Following systole, diastole begins, which is when the ventricles relax and the heart refills with blood.

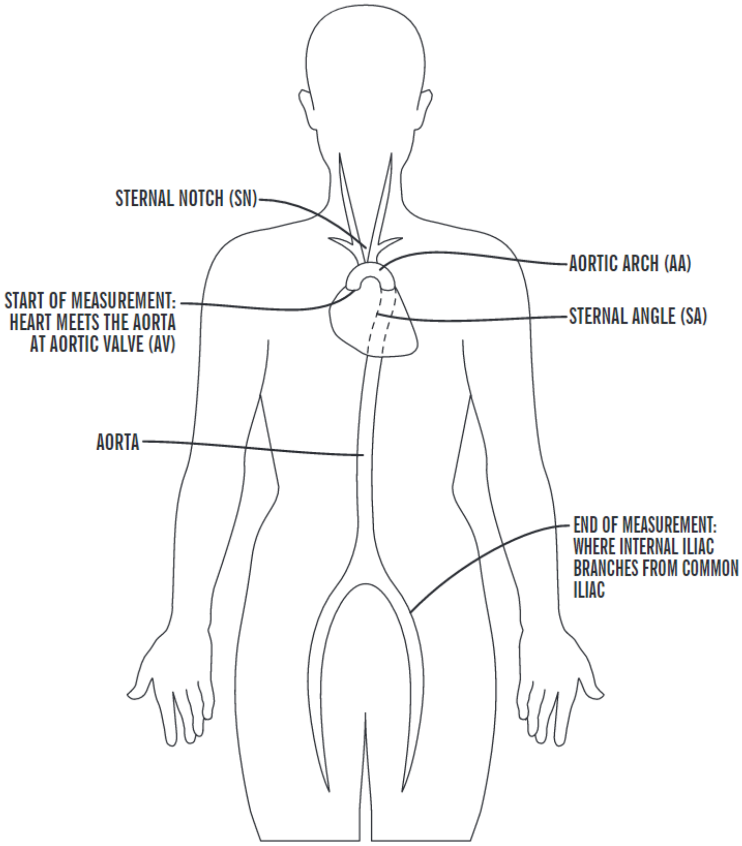

Figure 2.2: The aorta starts at the left ventricle and moves upwards before arcing downward towards the lower body. The aorta then branches directly below the abdomen into the two common iliac arteries.

A single cardiac cycle is initiated starts with an action potential generated by the sinoatrial (SA) node, as shown in Figure 2.3. The SA node consists of self-excitatory myocardium, allowing the creation of action potentials that result in a series of heart beats [11]. The electrical action potential stimulates the atria causing atrial contraction, which forces the blood in the atria into the ventricles. The action potential then continues through the atrioventricular (AV) node, and then after a small delay, continues down the left and right branch before stimulating the ventricles through the Purkinji fibers [11]. As the ventricles contract, the pressure in the ventricles increases until the aortic valve opens. Once the aortic valve opens, blood is injected into the aorta.

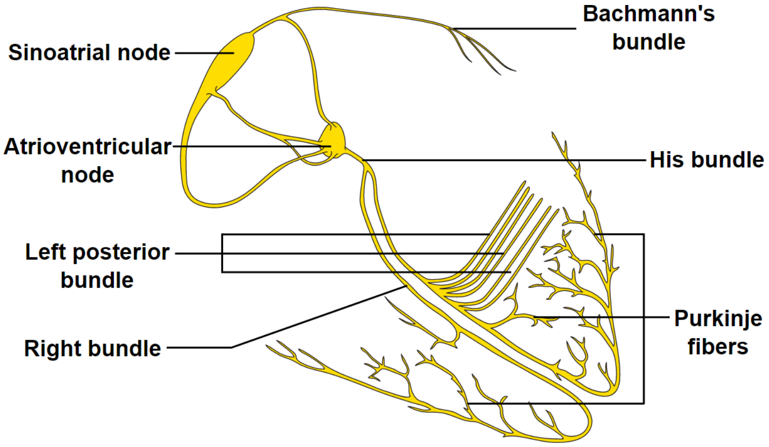

Figure 2.3: The electrical conduction system of the heart is shown, from the sinoatrial node to the Purkinje fibers [12].

The electrical activity of the heart can be measured using the electrocardiogram (ECG) and the mechanical forces of the heart can be measured using the ballistocardiogram (BCG). The photoplethysmogram (PPG) is an optical measure of local blood volume, which when used in combination with the ECG and BCG can illicit additional details relating to peripheral blood flow.

2.3 Electrocardiogram

The electrocardiogram (ECG) is a non-invasive medical device which differentially measures the changes in surface body potential caused by the depolarization and repolarization of cardiac tissue [11].

An example showing two typical ECG beats is shown in Figure 2.4. The ECG consists

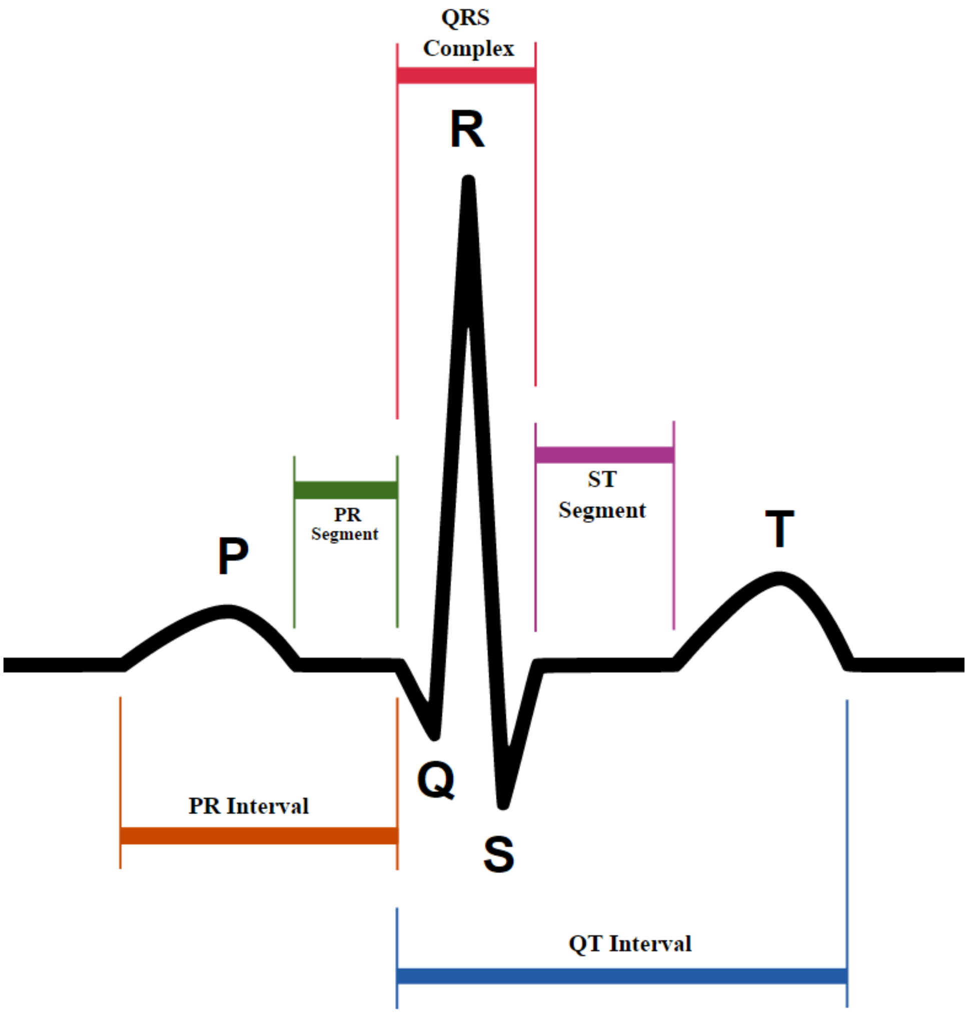

Figure 2.4: Two normal ECG beats are shown. A single ECG beat consists of the P-wave, the QRS complex, and the T-wave [13].

the P-wave, the QRS complex, and the T-wave [11]. The P-wave is generated from the contraction and activation of the atria, whose amplitude is significantly less than that of the QRS complex, which is the most prominent waveform in the ECG as it is created from the activation of the ventricles [11]. The beat-to-beat interval between neighboring R-peaks are typically used to determine the heart rate. It is also used as a reference point for delineation algorithms due to the fact that it is the most prominent and easiest feature to locate. Finally, the last wave in a normal beat is the T-wave, which is caused by the recovery, or repolarization, of the ventricles. T-wave morphology can vary greatly from individual to individual due to drug effects and metabolic factors [14].

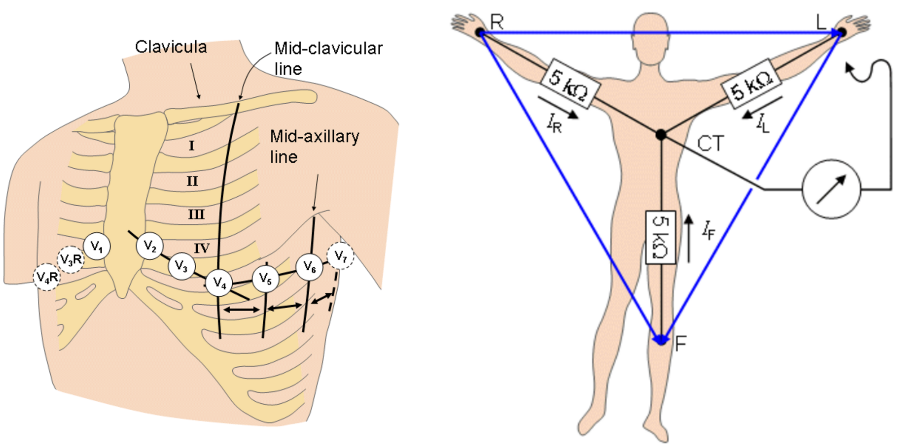

(a)

(b)

Figure 2.5: Each lead location for the 12-lead system is shown in (a) [15]. The Wilson central terminal is the reference for the unipolar leads. This is shown with Einthoven's triangle in (b) [15].

The ECG is measured differentially to reduce common mode noise, so lead placement becomes very important. There are many different methods for placing ECG leads, but the most popular and standard lead placement system is the 12-lead ECG system, shown in Figure 2.5a [11, 14]. The 12-lead system contains three differential limb leads corresponding to Einthoven's triangle (shown in Figure 2.5a and Figure 2.5b). Next there are three augmented limb leads, which are differential measurements between each limb lead with respect to the average of the other two limb leads. Finally, there are six unipolar leads. The unipolar leads are still measured differentially, but are all measured relative to the Wilson central terminal (CT) which will contain the common mode noise on the body. This point is considered the zero-point of the ECG and is extracted from the three limb leads via 5 k resistors as shown in Figure 2.5b).

The leads in the 12-lead ECG system can be used to reconstruct the orthogonal Frank leads, which represent the heart vector and consist of three orthogonal leads, one for each spatial dimension. This allows the entire cardiac cycle to be modeled as if the heart were a time-varying, rotating dipole with a variable magnitude [11]. This dipole is formed as cardiac tissue repolarizes after depolarization creating a moving charge gradient; this is illustrated in Figure 2.6. Contour and rotation of the heart dipole is not easily represented in the 12-Lead system; this is the main reason for using the Frank leads when working directly with this signal [16].

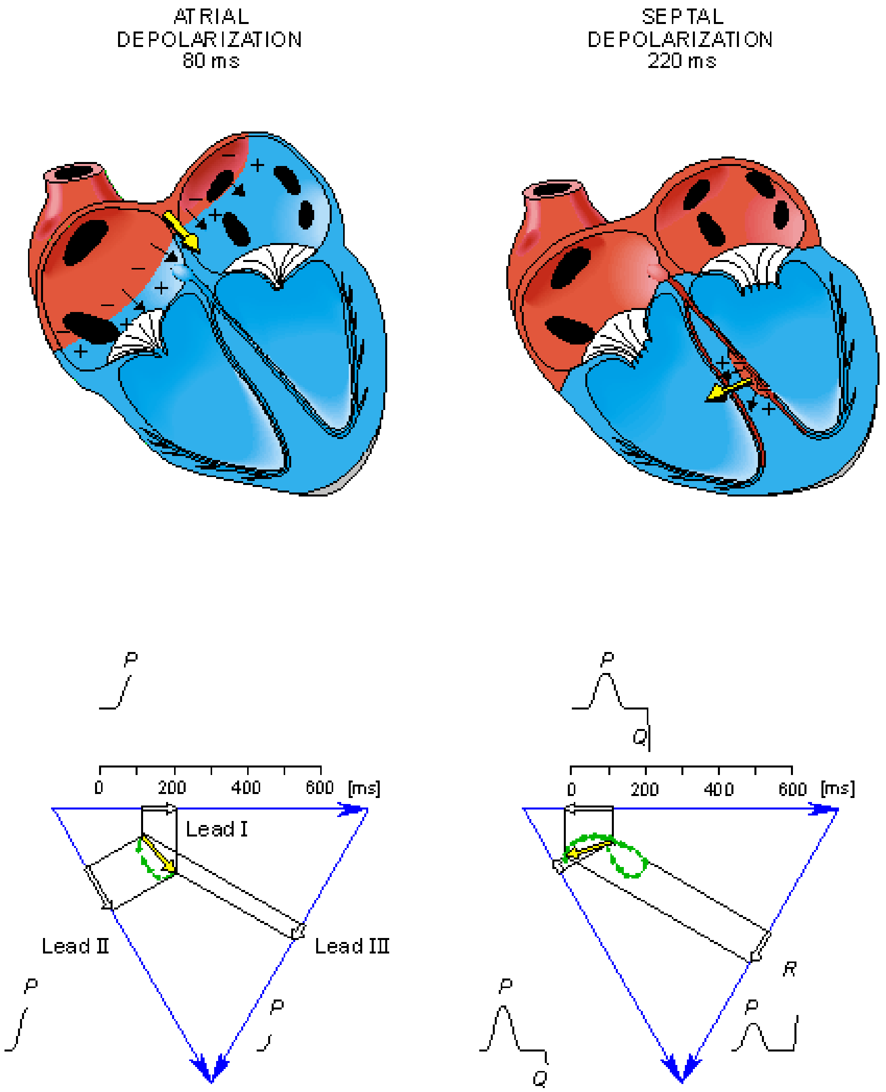

Figure 2.6: The heart can be represented as a rotating dipole created by the depolarization and repolarization of cardiac tissue [15].

As the lungs expand and contract during respiration, the heart will move and the impedance of the thorax changes. The impedance of the thorax and movement of the heart within the body affect the apparent orientation of the heart dipole, and thus the signal on each ECG lead. A 1 cm variation in location of the heart can result in a 24% change in surface potential as measured by the ECG [17]. Furthermore, it has been shown that respiration manifests itself as a rotation of the heart dipole along the orthogonal axes [18, 19]. The degree of rotation caused by respiration is approximately 10 degrees [19]. This is the mechanism that explains why each of the 12-leads in the standard ECG have different waveform morphology. The morphology of an ECG captured at an arbitrary point is likewise determined from the dot product of the electrode lead vector and the heart dipole [20, 21, 22].

The single lead ECG plays an important role in the diagnosis and management of cardiovascular disease. The ECG is clinically important because it is used to diagnose myocardial ischemia and infarction, atrial fibrillation, left ventricular hypertrophy/dilatation, left bundle branch block and intraventricular conduction delays, and left atrial abnormality [8]. These disease states can be diagnosed by monitoring rhythm and morphology changes in a single lead ECG. For example, changes in orientation could indicate myocardial infarction, such as when the T-wave is not in the same direction as R-wave or if the ST segment is elevated [23, 24]. Change in morphology and timing, such as a PR interval, could indicate conduction system dysfunction [25]. Similarly right ventricular hypertrophy (RVH) can be detected 87% of the time using ECG; an important prognostic as RHV tied to a 4.3-fold increase risk of death [26]. The heart rate (HR), heart rate variability (HRV), QRS duration, and corrected QT (QT_c) interval are of specific interest for the work presented herein.

The HR is calculated is calculated from the ECG by taking the average interval between consecutive R-peaks (RR-interval) across a set period of time. Heart rate variability is a measure of the variation between RR-intervals across time, often calculated as the standard deviation of RR-intervals across 5 minutes or 24 hours [27]. Changes in both HR and HRV can be used to predict cardiovascular events. For patients with (and without) coronary artery disease, resting HR is a predictor for mortality, independent of other risk factors [28, 29]. An elevated resting heart rate is associated with increased risk for incident heart failure in asymptomatic patients, and is related to development of regional and global left ventricular dysfunction independent of subclinical atherosclerosis and coronary heart disease [30]. Low HRV is associated with a 32-45% increased risk of a first cardiovascular event for patients with no previous history of cardiovascular disease, and is also associated with chronic heart failure, diabetes, and alcoholic cardiomyopathy [31]. In patients with advanced chronic heart failure, decreased HRV indices are an independent risk factor for mortality post myocardial infarction [32]. Additionally, a subject's heart rate variability (HRV) offers prognostic information and is significantly associated with risk for angina pectoris, myocardial infarction, coronary heart disease death, or congestive heart failure [33].

The QRS duration is defined as the time between the Q-wave onset and the S-wave end. An increase in QRS duration can be used to diagnose disease state and can be used as a predictor for sudden death [34]. As an example, a QRS width greater than 120 ms suggests that cardiac dyssynchrony may be present [35]. Additionally, QRS duration may have secondary value in predicting the prognosis in patients with heart failure [34]. Implantable cardiac defibrillator patients with heart failure (HF) that had a wide underlying QRS complex showed more than double the cardiac mortality compared to those with a narrow QRS complex [36]. The degree of QRS prolongation is correlated to an increase in severity of left ventricular systolic dysfunction, left ventricular dilation, and mitral regurgitation [37]. Left ventricular function worsens as the QRS duration increases [36, 37, 38, 39], making it an important parameter to monitor over time.

The QT interval is defined as the interval between the Q-wave onset and the T-wave end. Correcting the QT interval for different heart rates is necessary when looking for trends or comparison across recordings. The corrected QT interval (QT_c) is calculated using the

Bazett formula [40] in (2.1).

$$QT_c = \frac{QT}{\sqrt{RR}} \tag{2.1}$$

A prolonged QT_c interval is a strong, independent predictor of adverse outcomes in patients with heart failure, as the interval is related to ventricular polarization and repolarization [41]. Many drugs prescribed to cardiovascular patients change the PR interval and the QRS duration, however, they can also prolong the QT interval, which can be very dangerous. A drug induced prolongation of the QT interval is associated with Torsades de Pointes (a polymorphic ventricular tachycardia), which is the leading cause of sudden cardiac death (unexpected cardiovascular collapse without warning) [42, 43]. It is important for physicians to monitor QT prolongation when prescribing drugs to those with cardiovascular disease or when evaluating new drugs (drug screening). By looking at long term trends, each of these parameters can be used to monitor the progression of disease state over time.

2.4 Pulse Wave Velocity and Blood Pressure

Ventricular ejection starts only after the pressure in the left ventricle exceeds that of aortic pressure, at which time the aortic valve opens. At the end of ventricular systole, pressure falls in the left ventricle and the aortic valve closes. The time between the start of the QRS and aortic valve opening is called the pre-ejection period (PEP), the time that the aortic valve is open is the systolic ejection period, and the time between when the aortic valve closes and ventricular pressure reduces to its diastolic nadir, permitting the mitral valve to open, is the isovolumetric relaxation time.

The aortic PWV can be calculated by determining the length of the arterial segment divided by the pulse transit time (PTT) over that length. The velocity is the distance divided by the time. The PTT is determined by the start of ventricular ejection (when the aortic valve opens), as well as the point in time when the pulse wave reaches a specific end-point in the periphery.

The pulse arrival time (PAT) is a summation of the PEP and the PTT. The PEP starts at the beginning of ventricular contraction and ends with the start of ventricular ejection (when the aortic valve opens). The pulse transit time begins when the aortic valve opens and ends when the pressure wave reaches the distal measurement point. For blood pressure and aortic compliance, the ideal distal location is the end of the aorta, close to the start of the femoral artery.

The length of the arterial segment can be determined by various methods, including direct subject measurement on a user by user basis (discussed in Chapter 7). However, it is possible that the length can be estimated without direct measurement by using population statistics [44]. The aortic pulse wave velocity (PWV) is this estimated aortic length divided by the PTT.

Historically, there are four measurement techniques that are used for estimation of a pulse wave velocity. First, the clinical gold standard uses tonometry where a transducer is held against the carotid artery (neck) and a thigh pressure cuff is used to measure when the pulse wave reaches the femoral artery [45]. The distance between the two measurement points, coupled with the pulse transit time (PTT) is used to determine an aortic pulse wave velocity (PWV) and estimate aortic compliance.

In the second technique, two points on the same artery are used to measure an arterial PTT, with the distance between measurement points determining PWV [46, 47]. This is often done using two photoplethysmography (PPG) sensors with known separation between the two positions on the radial artery of the arm, or in the finger (using the foot to foot measurement of the two PPG waveforms). This technique estimates the PWV in the measured peripheral artery, not in the aorta, and is therefore not useful for determining aortic compliance, but is often used to estimate blood pressure [47].

The third technique uses the R-wave peak of the ECG is used as the starting point, with a peripheral PPG measurement (often finger, toe, or ear) used as the distal point [48, 49]. This measurement is called the pulse arrival time (PAT) and is often used as a surrogate for PTT (and PWV) in estimating blood pressure [50]. However, as this measurement technique includes the PEP it has no basis in physiology and fundamental pulse wave velocity/blood pressure theory [51, 52].

In the fourth technique, the BCG is used as the starting point (estimating aortic ejection) and PPG at the periphery (toe or ear) is used as the distal point for estimation of a PWV [53, 54, 55]. This approach measures an averaged PWV of the aorta and femoral artery. It has been used for aortic compliance estimation. However, it is not an accurate measurement of the true aorta PWV due to the contribution of the femoral artery distance from the end of the aorta to the toe and the carotid arterial distance from the aorta to the ear.

2.5 Photoplethysmogram

The photoplethysmogram (PPG) is a medical device that optically measures changes in local blood volume, based on the amount of light reflected or transmitted through tissue. The PPG requires a light source to illuminate the tissue in order to measure the change in light intensity. The raw signal measured by either a photodiode or phototransistor contains a large DC component caused by ambient light and the scattering of light within the tissue. The pulsatile AC signal caused by the pulse wave is much smaller. The AC component of the PPG is typically 0.1-1.5% of the DC component [56].

A standard PPG waveform is shown in Figure 2.7. It is a low frequency waveform with a bandwidth of 0.5 Hz to 17 Hz [56]. The PPG contains three major features: the PPG foot, the peak, and the dicrotic notch. The PPG foot represents the onset of the pulse wave; this point of the waveform is used to determine the end point of the pulse transit time (PTT) and pulse wave velocity (PWV). The PPG peak is the maximum of pulse wave and the dicrotic notch is caused by a second, reflected peak in the PPG [57].

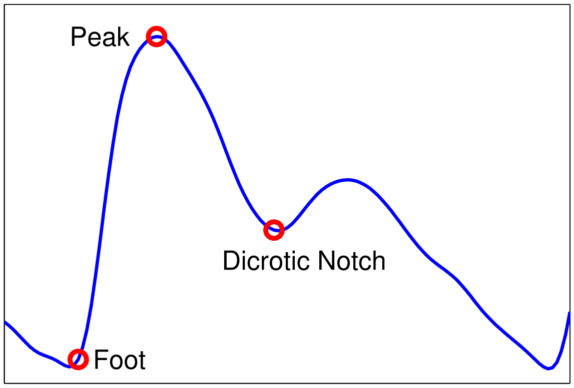

Figure 2.7: A single PPG beat consists of the foot (also known as the beat onset), the peak, and the dicrotic notch. The foot is created when the pulse wave reaches the localized tissue.

The PPG is most commonly found in a pulse oximeter, which is a medical device that uses two PPG signals measured at different wavelengths to estimate blood oxygenation levels

(SpO2). This is possible since oxygenated blood and deoxygenated blood have different absorption spectra. The absorption spectra of oxygenated and deoxygenated hemoglobin is shown in Figure 2.8.

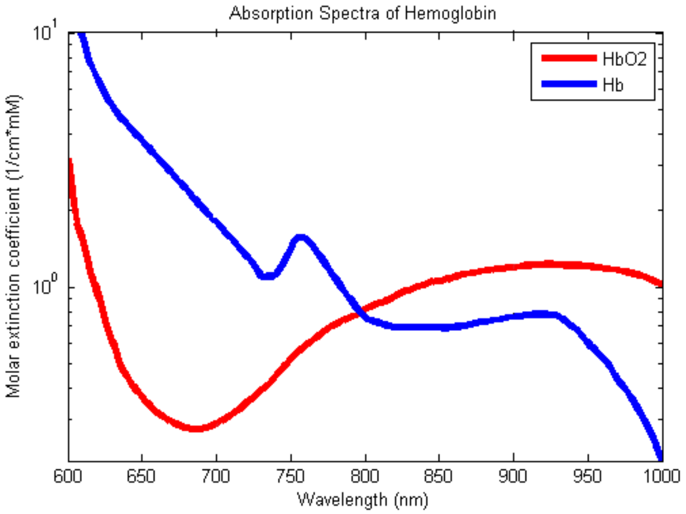

Figure 2.8: The absorption spectrum for oxygenated and deoxygenated hemoglobin is different, allowing a pulse oximeter to estimate the blood oxygen saturation of the localized tissue [58]. Typically, red (660 nm) and infrared (940 nm) wavelengths are used.

The FIT bPPG is used when estimating both pulse transit time and blood oxygenation (SpO_2). The FIT seat is capable of measuring a subject's peripheral oxygen saturation (SpO_2) using a dual wavelength reflectance mode photoplethysmogram (pulse oximeter), positioned to make contact with the upper thigh. A pulse oximeter measures blood oxygenation by illuminating tissue with two different wavelengths of light and measuring the returned light intensity with a photodiode. The illumination is provided by a red LED with a wavelength of 645nm, and an infrared LED with a wavelength of 940nm. The critical value extracted from the raw data which is used to calculate SpO_2 is the "R-value". This is the compound ratio of the AC to DC amplitudes for each wavelength, as shown in (2.2).

$$R = \frac{AC_{645nm} DC_{645nm}}{AC_{940nm} DC_{940nm}} \tag{2.2}$$

Normally, the light source is either reflected off of a bone, as is the case in the finger and forehead, or transmitted completely through the tissue, as is the case in the earlobe or the finger. This research investigates the use of the PPG on the buttocks and hamstring. At this location, the PPG will not be operating in reflective mode nor will it be able to transmit light through the tissue. This presents a unique problem for both the PPG instrumentation and the sensor construction. It expected for a buttocks PPG (bPPG) to work due to the scattering of light in the local tissue. This will require the distance between the light source and photosensor to be optimized and as well as the sensitivity of the analog-front-end to be maximized.

The correlation between R-value and SpO_2 is highly linear for changes in SpO_2 of about 10%, and remains approximately linear over the entire range of possible values. The correlation is highly dependent on the two wavelengths of light chosen, and to a small degree the position on the body where the measurement is taken. Furthermore, the device hardware and optics impact the relationship between the R-value and SpO_2. As such, all commercial pulse oximeters need to undergo calibration. The FIT seat is no exception.

Commercial pulse oximeters must undergo testing according to ISO 80601-2-61:2011, which includes R-curve determination using a set of subjects undergoing a controlled desaturation study while monitored by the pulse oximeters under test and an in vivo SaO2 monitor. This is out of the scope of this study, so a hospital finger pulse oximeter was substituted as our reference while a subject underwent controlled desaturation. Two subjects underwent the desaturation test, taking their SpO_2 from a resting value of approximately 100% down under 80% over the course of several minutes, and then returning back to 100%. The R-curve is plotted against SpO_2 for both subjects in order to calibrate the device.

2.6 Ballistocardiogram

The ballistocardiogram (BCG) measures the ballistic forces of the heart. Unlike the ECG which measures the electrical activity of the heart, the BCG can provide insights into the myocardium function and cardiac output [59]. The BCG was pioneered in the 50's and 60's by Starr for use in diagnosing issues with cardiac output, cardiac infarction, and chronic angina pectoris [60, 61, 59, 62, 63, 64]. In addition to these disease states and metrics, the BCG can be used to determine coronary disease, ventricular asynchronism, hypokinesia, hypertension, and age related weakening of the heart [65].

After about 30 years of continuous and consistent BCG research, the instrument's use saw a significant decline [66]. Despite a recent resurgence of interest in the BCG, there are no commercially available clinical BCG systems. With improved modern sensing techniques, the BCG can now be reliably measured in bathroom scales and in wearable technology such as an ear based accelerometer [67, 68, 69, 70].

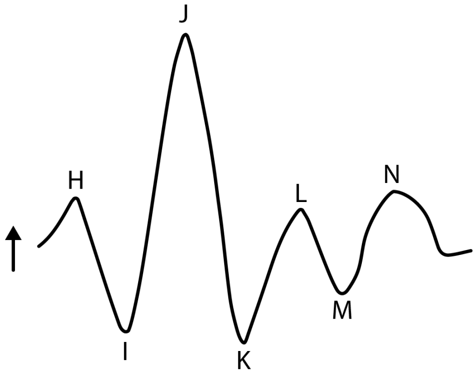

Figure 2.9: A typical BCG waveform as measured by Starr. Adapted from [60].

The original technique for measuring the BCG involved a suspended bed on which the subject laid [60]. The displacement of the suspended bed was measured and related to heart function. Other systems involved measuring a subject lying on a bed suspended in mercury [71]. Systems utilizing load-cells and piezoelectric sensors directly measure the change in force due to the ballistic forces of the heart [72, 67].

An example of the BCG waveform measured by Starr is shown in Figure 2.9 [60]. This BCG waveform contains the following features: H, I, J, K, L, M, and N. It is theorized, but not proven, that the H peak is related to the motion of the heart early in systole, and that the IJK complex is related to the ventricular ejection and resulting aortic flow [66]. The cause of the other waves is not known [66].

2.7 Conclusion

Each of these devices are utilized in the fully integrated toilet seat. The ECG is used to extract key timing intervals and to provide a reference point for all other analysis. A seated BCG is captured in order to estimate cardiac function and the timing of aortic valve opening, which is the start of the pulse wave at the aortic root. The PPG is used to measure the end of the pulse wave velocity at the end of the aorta, and to provide SpO_2.

Chapter 3

A Toilet Seat for In-Home Cardiovascular Monitoring

3.1 Introduction

The design and verification of the fully integrated toilet (FIT) seat is described in this chapter. Specialized hardware required for measurements in non-standard locations are presented. Each version of the FIT seat, and subsequent improvements are detailed with a focus on the systems used for human subject testing. Finally, expected use cases are presented with the results from an in-home ethnographic study.

3.2 System Introduction and Overview

Advances in ultra-low power electronics, signal processing techniques, sensor technologies, and wireless interconnectivity offer new opportunities for truly inconspicuous daily medical analyses. Of particular interest is measurement of the electrocardiogram (ECG), ballistocardiogram (BCG), and photoplethysmogram (PCG), enabling a broad range of clinically relevant and predictive analyses when these signals are simultaneously captured.The entire FIT seat system is shown in Figure 3.1.

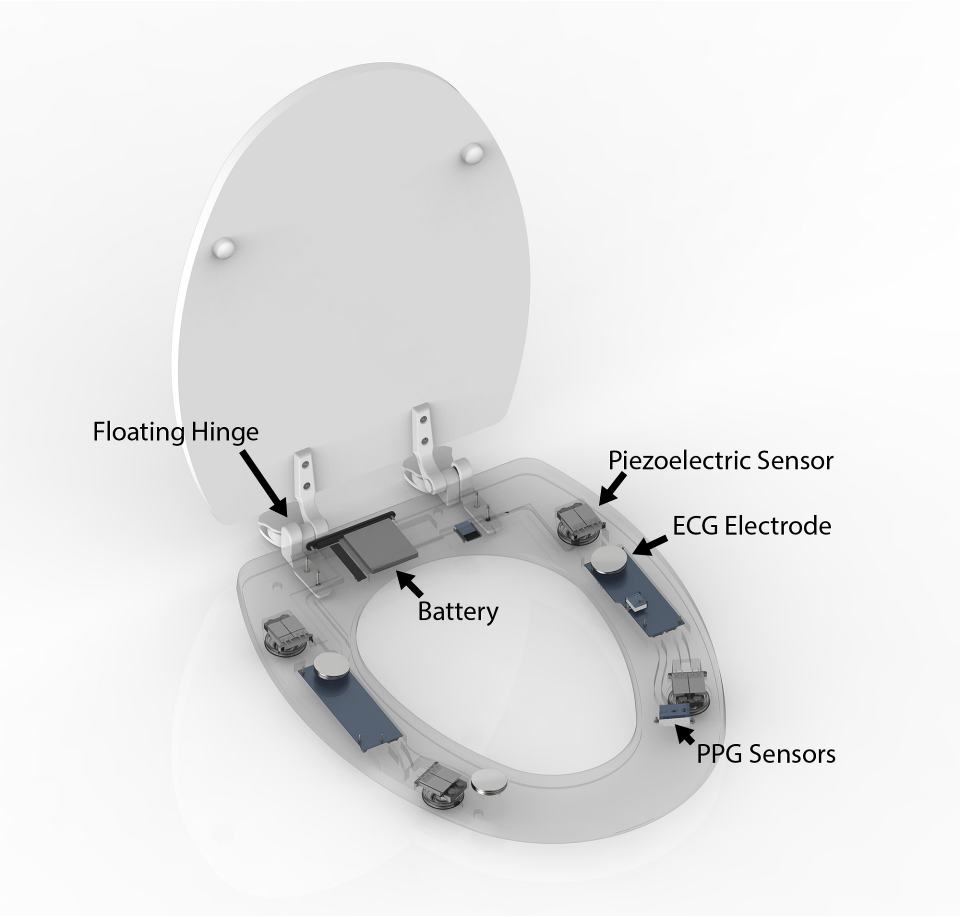

Figure 3.1: A rendered view of the complete integrated FIT system, showing all internal instrumentation.

There are examples in literature demonstrating that it is possible to capture an ECG from a toilet seat [73, 74, 75, 76, 77, 78, 79]. Only the work presented in [76] has quantitatively compared the seated ECG on a toilet seat to a gold-standard ECG measure, where both non-contact and wet electrodes placed on the thigh were compared to a standard limb lead ECG. Their results showed that manual R-peak delineation resulted in less than a 2 ms error in location and that the estimated HR was within 0.003 bpm for a single test subject. Similarly, it has been demonstrated that the PPG can be acquired from a toilet seat in [74, 80, 79]. Only the work presented in [80] provided a quantitative measure of the PPG compared to an ECG in order to determine the optimal location for the optical sensor. Results showed that the front of a toilet seat is the optimal location to measure the PPG.

Bioimpedance has been used in [81, 75] to estimate body composition. In [81] the body fat ratio estimated from the impedance measures were verified in a controlled study with 86 subjects, resulting in a high linear correlation (R=0.87). Blood pressure has been estimated from a toilet seat using the volume-oscillometric method in [82] and pulse arrival (PAT) based method in [79, 83]. The work presented in [83] showed a quantitative comparison of toilet seat based blood pressure across three subjects. Their results show that the blood pressure estimation error had a average error of 12.3 mmHg.

The proposed system expands on what has been accomplished in literature in a number of ways. Every sensor in the proposed system is completely integrate into the seat and does not require any external equipment or devices for proper operation. In [84, 85] weight was measured by placing the entire toilet on a platform and the ECG was measured from electrodes on the seat. In the work presented in [81], weight was acquired using load-cell between the seat and the toilet, however the system did not have a hinge and required the subject to lift up their feet. This work also proposed a shaft based cantilever system for monitoring weight, and verified the system using only dead weight.

The following list describes all of the measurements that will be extracted from the proposed FIT seat:

Heart rate

The average heart rate (HR) of an individual will be calculated from the bECG and bPPG.

HRV

The heart rate variability will be calculated from the ECG. Low HRV can indication an impending cardiac event and can be used to estimate stress levels.

QT interval

The QT interval represents the recovery time of the ventricles after contraction. This metric is often used to determine the effect of medication on the heart.

QRS duration

The duration of the QRS complex can indicate heart failure and other cardiovascular issues.

SpO_2

The blood oxygen saturation (SpO_2) percentage can be measured using a two wavelength bPPG. Low SpO_2 values can be used to indicate heart failure.

Aortic pulse transit time

The pulse transit time (PTT) is the time that it takes the pulse wave to propagate through the length of the aorta. This is defined as the interval between aortic valve opening and the start of the pulse wave at a peripheral location. This can be calculated from the BCG and the bPPG, where the bPPG foot is the end of the pulse transit time.

Aortic pulse wave velocity

The pulse wave velocity (PWV) is calculated using the aortic PTT and the length of the aorta. The length of the aorta can be determined on a subject-by-subject basis or using demographic statistics.

Cardiac output

Cardiac output can be estimated from the BCG, as the IJ-amplitude has a linear correlation to cardiac output. This is the leading indicator of heart failure.

Blood pressure

The blood pressure (BP) can theoretically be estimated using the PWV. This is a useful tool for tracking the progress of patients with cardiovascular disease.

The captured data can be wirelessly transmitted to either a base station in the home or a subject's smart phone or tablet or transfered over a USB connection for real-time visualizations. The resulting data can then either be kept solely on the user's device or uploaded to the cloud. This would allow physicians and family member to monitor an individuals cardiac heath if desired. This device has the potential aid in the prevention of cardiovascular disease through preventative monitoring and to revolutionize how cardiovascular disease is currently managed.

The functional differences between the normative system and the integrated system are shown below in Figure 3.2. These differences are discussed throughout this chapter.

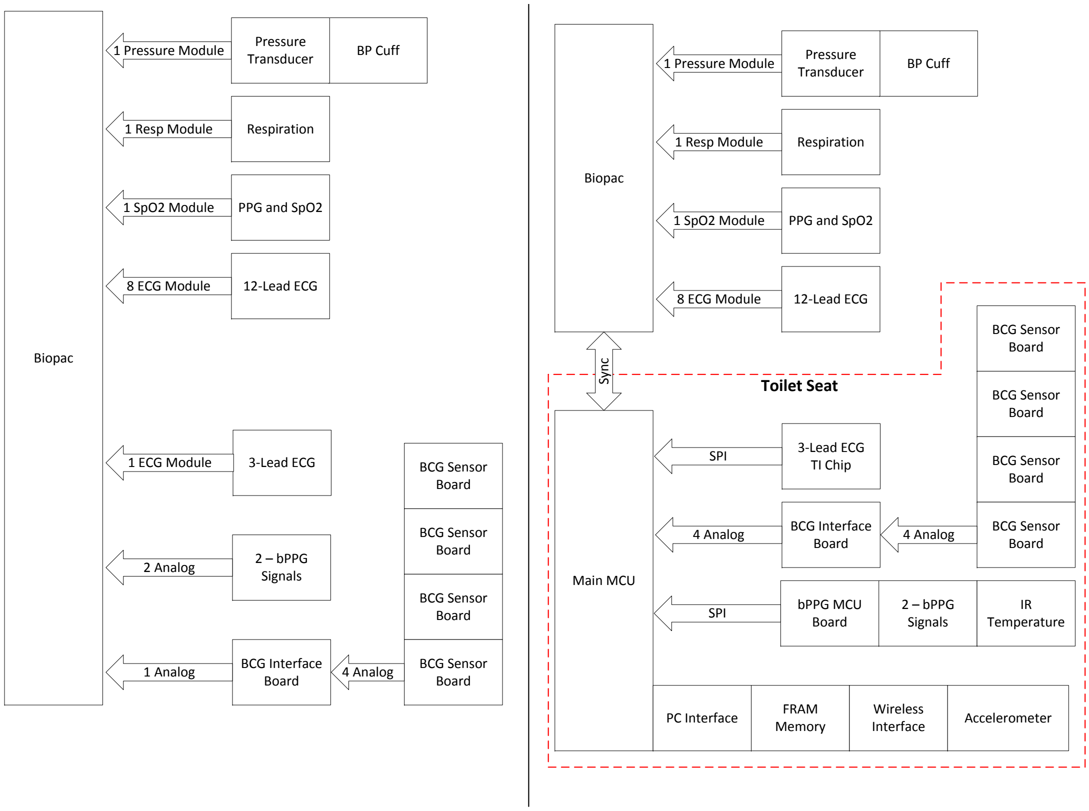

Figure 3.2: The system block diagram for the FIT seat details every sensor in the normative seat (left) as well as the differences between the normative system and the integrated system.

3.3 Hardware

3.3.1 ECG Instrumentation

The ECG is a very small signal: the amplitude of the limb leads are typically less than 2 mV and it has a frequency range of 0.05 to 100 Hz [14]. Ambient electromagnetic noise in the environment is significantly larger than the ECG signal. For this reason, the ECG signal is measured differentially so that the common noise across the body can be rejected during amplification. This works under the assumption that the environmental noise should be approximately the same across the whole body. As such, each ECG waveform is a measure of the difference between two electrodes.

A standard single channel ECG consists of three electrodes, two differential electrodes, and one reference electrode. The two differential electrodes are amplified by a differential amplifier before further amplification and analog filtering. An instrumentation amplifier (INA) is commonly used in an ECG analog-front-end (AFE) due to its high common mode rejection. An example of basic ECG instrumentation is shown in Figure 3.3. Details on the electrode/skin interface and sources are discussed in the following section.

The reference electrode can either be tied to a reference voltage such as ground, or driven by the amplified and inverted common mode signal. The common mode signal can be found at the center point of an INA's gain resistor, as shown in Figure 3.3. The signal is then greatly amplified using an inverting amplifier, and fed back into the electrode through a current limiting resistor. Additional sources of noise include motion artifacts, baseline wander, and the electromyogram (EMG).

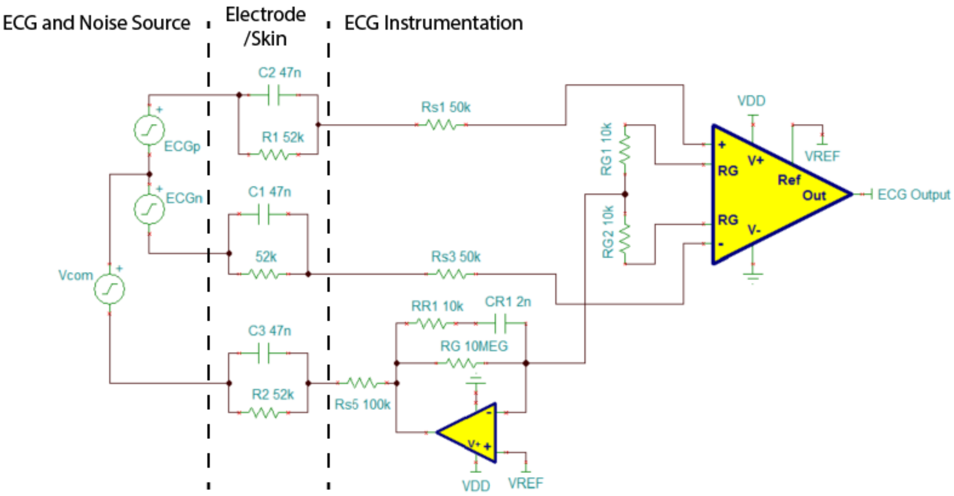

Figure 3.3: A basic ECG amplifier is shown, which amplifies a single differential channel using an instrumentation amplifier. In this configuration, a driven right leg circuit is used for the third electrode.

After the initial amplification stage, the ECG can be high-pass filtered using a passive filter with a cutoff frequency of 1 Hz in order to limit baseline wander from the electrode interface. Then the signal can be further amplified, low-pass filtered, and sometimes notch filtered (to remove line noise) before the analog signal is converted to a digital signal.

Despite using an instrumentation amplified for high common mode rejection, power line noise can still dominate the acquired signal. In the United States the line noise is at 60 Hz, in many other countries the line noise is at 50 Hz. The digital ECG signal then undergoes digital signal processing to remove any remaining noise, before being analyzed, as discussed in Chapter 4.

The ECG system utilized in the FIT seat will be a single channel ECG with a grounded right leg. The hardware will be capable of having a driven right leg, however this will not be used for subject testing. An active ECG AFE has been used that incorporates a high-pass filter (1.6) Hz and buffer, which is differentially amplified by an instrumentation amplifier (G=1100) before being bandpass filtered. A two stage bandpass filter has been used, consisting of a high-pass filter and then a low-pass filter (0.5-40 Hz). This signal is then acquired either by an external data acquisition system (DAQ) or an internal DAQ depending on the testing being performed.

3.3.2 ECG Electrode and Body Modeling

One of the largest factors that impact noise and motion artifacts is the electrode interface. When designing an ECG, understanding how the impedance of the body and the electrode impact performance allow for a more robust device. The electrode interface and human body can be electrically simulated and modeled using the electrical properties of the materials and tissue involved.

The electrode impedance can be modeled for electrical simulation using capacitors and resistors. Similarly, the signal source and the body/skin can be modeled using capacitors and resistors. A simplified electrical model of the body and electrode interface for an ECG is shown in Figure 3.3. The heart dipole is simulated using two voltage sources of opposite polarity, and the common mode noise is simulated as Vcom.

Understanding the electrode interface and skin impedance is a key part of designing a successful ECG AFE. When a wet electrode is used (one with conductive gel between the skin and the metal contact), the overall impedance is low and is dominated by the skin impedance. When the skin impedance dominates, the dominant element becomes the resistance and a standard high-impedance instrumentation amplifier can be used.

Often, a dry electrode must be used for certain applications, such as wearable devices. Wet electrodes can dry up, limiting the potential measurement duration. Additionally, wet electrodes must be physically placed on a subject's prepared skin before use. Dry electrodes do not rely on conductive gel between the skin and metal contact, but have a significantly larger impedance. The interface is now dominated by the electrode skin/interface. Despite the high impedance, the interface is still dominated by the resistive component of the interface. The SNR can be further impacted by long lead length, since the high impedance electrode/skin interface is much more prone to electromagnetic noise pickup and impacts the common mode rejection of the instrumentation amplifier.

Another option for measuring the ECG is a capacitive electrode. This electrode is insulated and does not make a resistive connection with the skin. In this case, the electrode is capacitively coupled to the body. This results in an interface that is dominated by the capacitive element. The resulting instrumentation must be capable of amplifying a capacitive sensor in addition to ensuring the capacitance does not filter out frequencies that are present in the ECG. Capacitive electrodes are not used in the work presented herein.

When using a dry electrode, active electrode circuitry is needed to buffer the impedance between the electrode and instrumentation amplifier. It is important to minimize the lead length between the skin interface and the active electrode amplifier. This increases signal to noise ratio (SNR) and reduces the amount of electromagnetic noise pickup. An example active electrode is shown in Figure 3.4. A non-inverting amplifier at unity gain is used to buffer the impedance. Since there is no amplification, the common mode rejection of the INA does not suffer due to component mismatch.

The circuity used in the FIT seat contains ESD protection diodes, and a high-pass filter with a cutoff frequency of 1.6 Hz. The op-amp used is an OPA376 from Texas Instruments, which has a voltage noise of 75 nV/rtHz at 1 kHz. The V+ is a 3V regulated rail and AGND is a 1.5V regulated rail. Bypass capacitors are placed in close proximity to the op-amp on

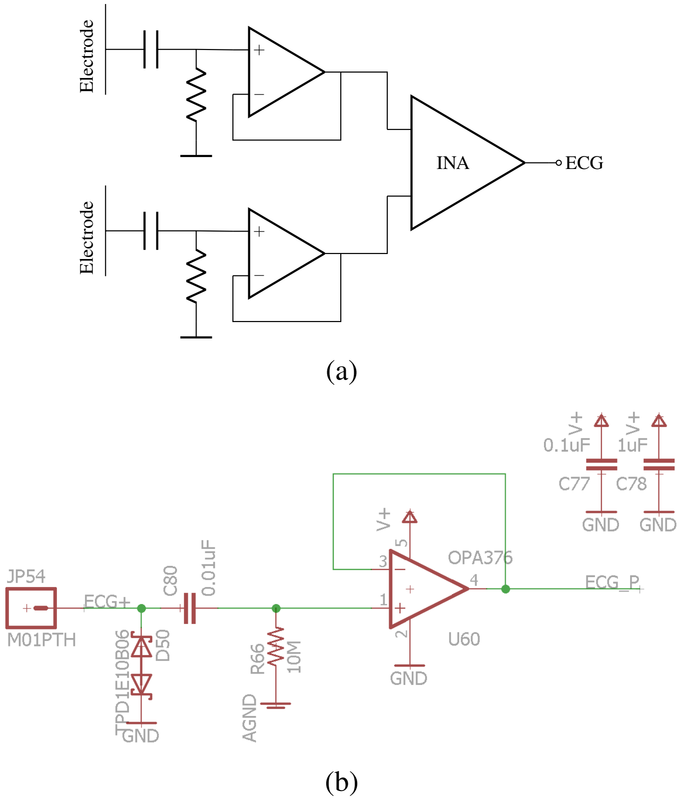

(a)

(b)

Figure 3.4: Two active electrode analog front end circuits are used with an instrumentation amplifier to increase the SNR of dry electrodes (a). The active front-end used in the FIT seat with associated component values is also shown in (b).

the circuit board. Two matching pairs of active electrode feed into an integrated ECG AFE from Analog Devices (AD8232).

When using an active electrode, it is important for the metal contact to be as close to the op-amp as possible. In this FIT seat, this distance is kept to less than 1 cm by directly soldering the electrode wire to the active ECG instrumentation circuitry. The electrode wire is connected to the stainless steel electrode using conductive epoxy in the integrated seat and is welded in the normative seat.

3.3.3 PPG Instrumentation

In the most basic form, a PPG analog-front-end (AFE) can consist of a phototransistor, a buffer, a high-pass filter, and low-pass gain stage, as illustrated in Figure 3.5.

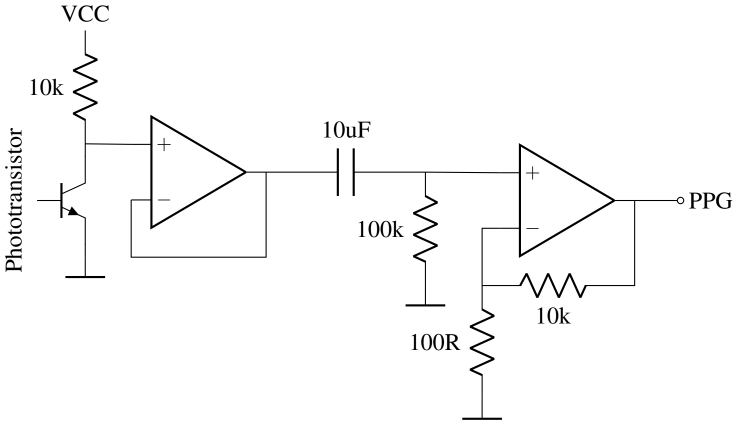

Figure 3.5: A simple PPG AFE built using a phototransistor, a low-pass filter, and an amplifier.

There are generally two types of sensors that can be used to measure light intensity in the PPG: photodiodes and phototransistors. For low-power systems, the LED must be pulsed with a very low duty cycle in order to minimize power consumption. This requires a fast photosensor that will stabilize quickly so the LED can be turned off sooner. Commercially available phototransistors do not have a sufficient response time, so for this reason, the photodiode is used in the FIT seat. The schematic for the normative PPG AFE is shown in Figure 3.6. For the normative seat, VCC is a 3.3V regulated rail.

The overall power consumption of the PPG is limited by the LED light source, resulting in the PPG consuming more power compared to other cardiac instrumentation. In order to reduce the power consumption in portable instrumentation, the light source is pulsed at a low duty-cycle (¡20%). The signal is then sampled while the LED is on after the analog-front-end stabilizes. This is a mandatory design choice for any portable pulse oximeter or PPG. It is for this reason that the simple PPG circuit shown in Figure 3.5 (used in the

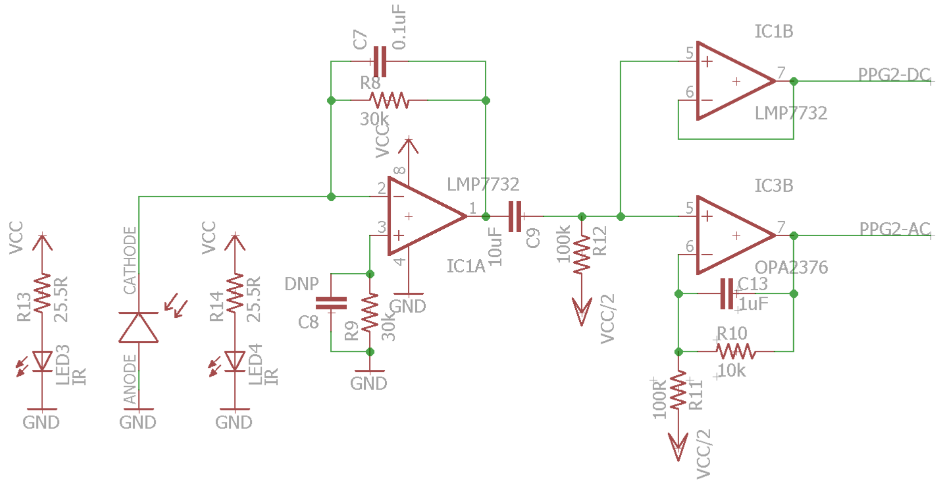

Figure 3.6: The PPG analog-front-end for the normative FIT seat utilizes a photodiode with a transimpedance amplifier, rather than a phototransistor.

normative system) is not used in portable or battery powered applications.

When pulsing the LED, the resulting waveform can no longer be thought of as a continuous waveform. As such, it cannot be low-pass or high-pass filtered in the analog domain to remove ambient light noise at the power line frequency (e.g. 60 Hz) and its harmonics (e.g. 120 Hz). Since this noise cannot be removed with analog filtering, the signal must be oversampled to avoid aliasing so that it can removed digitally after sampling. Despite the increased sample rate, the overall power consumption is still significantly lower when compared to a non-pulsed design solution, as dictated by the LED duty cycle. Typical sample rates for the PPG are 240 Hz and 480 Hz [90, 91].

The DC level is removed using active DC cancellation, since an analog high-pass filter cannot be used. A differential amplifier is used to amplify the difference between the sensor output and a DC level, which is generated using a digital to analog converter (DAC) and a microcontroller (MCU). The DC level is calculated using a microcontroller that samples the output from the photodiode transimpednace amplifier (TIA) before the analog signal is amplified. A schematic detailing this process is shown in Figure 3.7.

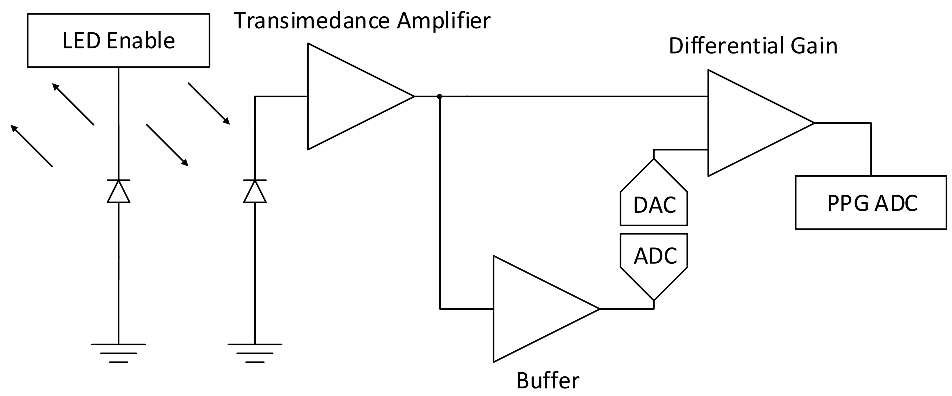

Figure 3.7: The PPG analog front end utilizes a red and IR LED (only one shown) with a photodiode amplified with a transismpedance amplifier (TIA) to measure the signal. Since the LED is pulsed in order to reduce power consumption, the DC offset from the TIA cannot be removed with a high-pass filter. The DC offset is actively removed by digitally generating a DC reference for a differential amplifier, calculated using a moving average of the measured DC values from the output of transimpedance amplifier.

The schematic for the two wavelength custom PPG AFE that is utilized in the FIT seat is shown in Figure 3.8. Both the red (660 nm) and IR (940 nm) LEDs have variable current control so that power consumption and SNR can be optimized by the MCU. Both LEDs utilize the same analog circuitry since only one of them will be on at a time. The output from a single wide-band photodiode is fed into a transimpedance amplifier (TIA) based on the OPA2313 with a slew rate of 0.5V/µs; this allows the LEDs to be pulsed for 294 µs resulting in a duty cycle of 5% for a sample rate of 170 Hz. After the active DC cancellation using an instrumentation amplifier, the signal undergoes amplification with a total gain of 301 V/V. The output signal is then acquired by an external data acquisition system (DAQ) for the normative FIT seat or an internal DAQ for the integrated FIT seat.

The main challenge with measuring the PPG on the buttock is that the sensor does not operate in reflective mode nor in transmission mode. The resulting signal quality is greatly reduced since it is believed the signal measured relies on the scattering of light in the local tissue. This has the potential to be inconsistent between subject due to different body composition and varying sensor locations. When measuring the PPG on the buttock, the

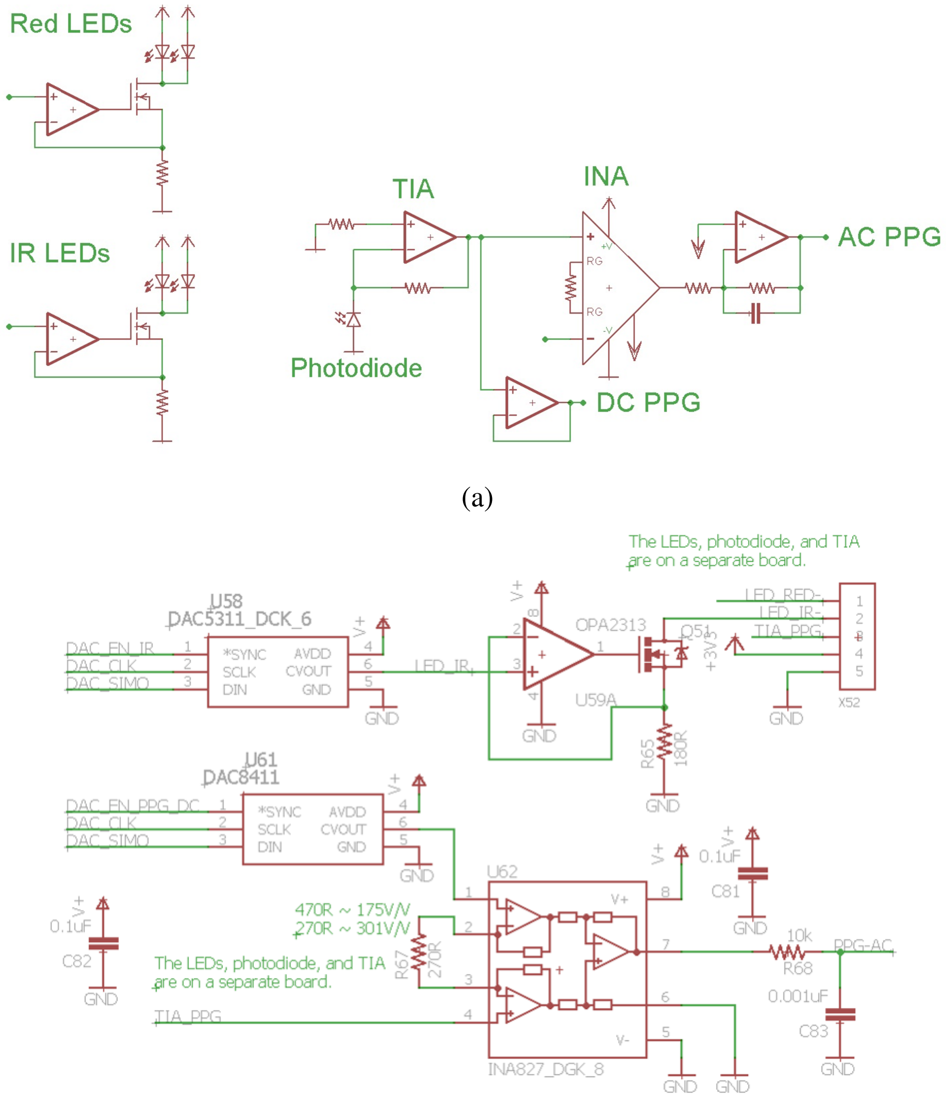

(a)

(b)

Figure 3.8: The PPG AFE in the FIT seat has variable power controlled LEDs and active DC cancellation. The integrated MCU samples the DC level directly after the transimpedance amplifier, and then calculates the average DC value. This is then used as the negative input on the instrumentation amplifier to remove the DC level. The high level concept of this is shown in (a), while the implemented version is shown in (b).

LED power needs to be much higher since the signal must scatter through the local tissue. This is especially challenging when the system has a power consumption constraint, since the LED power cannot be ramped up to the maximum possible intensity. A potential solution to reducing the PPG power while maintaining high signal quality is to use compressed sensing and high-speed circuitry.

3.3.4 BCG Instrumentation

The system utilized in the fully integrated toilet seat measures the BCG using force sensors integrated into four standoffs. The sensors investigated in this work include the A401-25 FlexiForce piezoresistive sensor, LDT0-028K piezoelectric sensors from Measurement Specialties, and unmarked strain gauge based load-cells (available from SparkFun Electronics).

The schematic used for the FlexiForce sensor is shown in Figure 3.9. The FlexiForce sensor changes resistance based on the force applied. The first stage is an inverting amplifier where the output is related to the bias voltage across the sensor (-V) and the resistance of the sensor. The FlexiForce sensor can measure both dynamic and static forces since it is a piezoresistive sensor. The DC output can be buffered and captured to estimate the DC static weight of a subject sitting on the seat. The following stage is a high-pass filter that will remove any low frequency signal including DC weight. The final stage is a non-inverting amplifier with a built-in low-pass filter for removing high frequency motion and noise.

The piezoelectric sensor cannot measure static forces, but it is significantly more sensitive to small dynamic changes than the piezoresistive sensor. A piezoelectric sensor can be thought of as an ideal voltage source with a capacitor in series or as a voltage source with

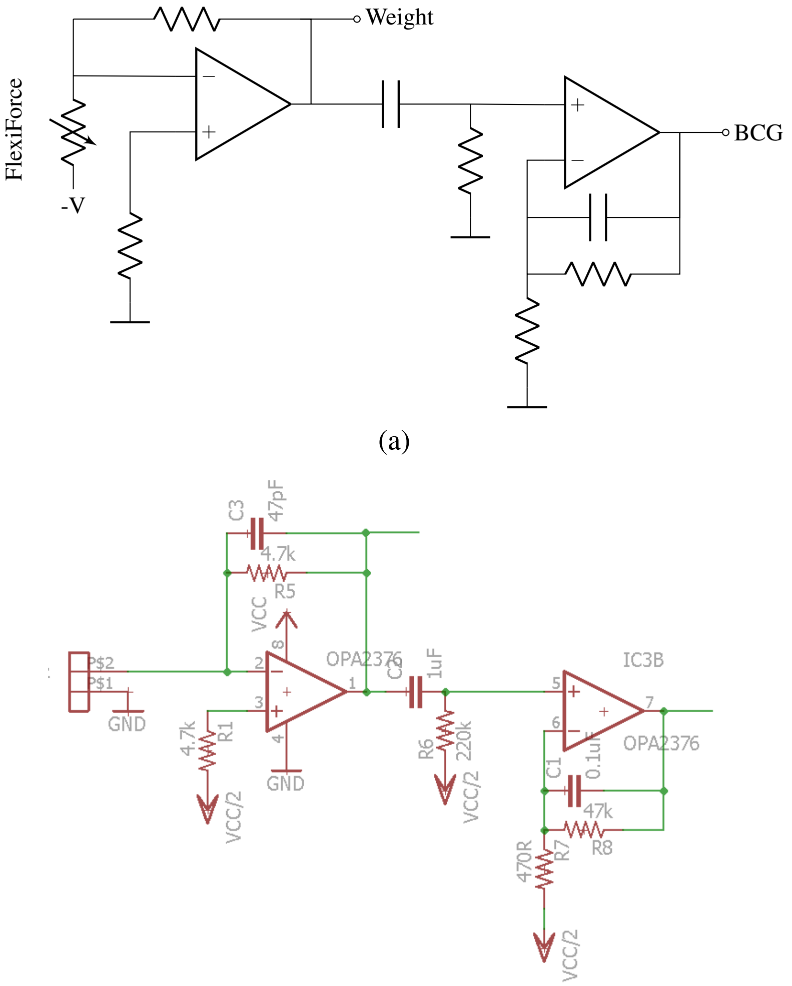

(a)

(b)

Figure 3.9: The AFE for the FlexiForce piezoresistive sensors includes a high-pass filter and a gain stage. If desired, the DC response can be measured by branching off the sensor output before the high-pass filter. The high level overview of the schematic is shown in (a) and the schematic used for the normative system is shown in (b).

a capacitor in parallel. There are two different circuit configurations that can be used in the piezoelectric AFE, one that amplifies the voltage across a load resistor, and the other that directly amplifies the charge across the sensor. The circuit configuration that amplified the voltage across the load resistor is used in the FIT seat, as shown in Figure 3.10.

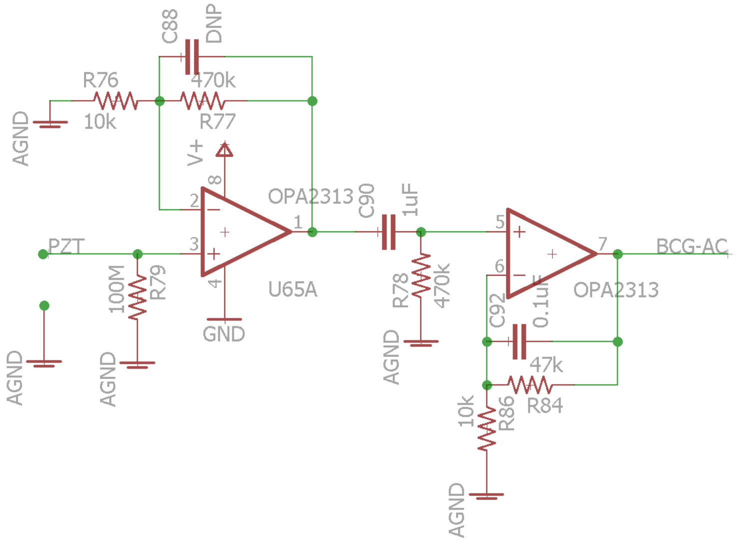

Figure 3.10: The PZT instrumentation in the FIT seat consists of a non-inverting gain stage, followed by a band-pass filter with a bandwidth of 0.34 Hz to 34 Hz. The load resistor for the PZT must be large to maximum the signal amplitude for low frequencies, as the PZT sensor has a capacitance of 480 pF. With a load resistor of 100 megaohm, the cutoff frequency is 3.3 Hz.

Due to the shortcomings of the PRT and PZT sensors, as discussed in Chapter 7, a third design is proposed utilizing a load-cell. A load-cell is commonly found in bathroom scales and provides very accurate and repeatable static weight measurements with a very high repeatability. The load-cell output is amplified using an instrumentation amplifier in a half bridge configuration, where each load-cell contains two complementary sensing elements. The BCG signal is very small compared to the static weight on the sensor, so the INA827 was chosen as the instrumentation amplifier. It has a very low noise of 17 $nV/\sqrt{Hz}$, a common mode rejection ratio (CMRR) of 88 dB, and power supply rejection ratio (PSRR) of 100 dB. After the INA bridge amplifier with a gain of 5V/V, the DC component of the signal is removed using a high-pass filter with a cutoff of 0.33 Hz for further amplification and filtering of the BCG. The BCG is then amplified by 47 V/V and low-pass filtered at 16 Hz. The schematic used in the FIT seat is shown in Figure 3.11.

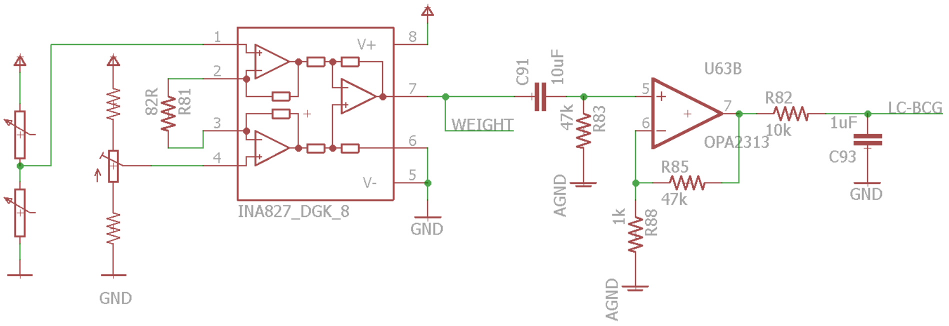

Figure 3.11: The load-cell instrumentation in the FIT seat consists of an instrumentation amplifier in a half-bridge configuration, followed by a band-pass filter. A potentiometer is placed between the fixed resistors in order to compensate for the variation between elements within the load-cell.

The magnitude of the BCG is typically between 3-5 N, which corresponds to approximately 1/1000th of a subject's total weight. Since the BCG sensors must be sensitive enough to measure this small signal, any motion including respiration, hand movement, and changing posture are sources of noise that are often one or more orders of magnitude greater than the BCG signal, causing the instrumentation to saturate.

3.4 Weight and BCG Mechanical Systems

The toilet seat rests on four standoffs and a floating hinge. A single BCG and a single weight sensor are integrated into each standoff. This allows the BCG and weight to be measured independently for each standoff, resulting in more robust post-processing of the signals. This post processing is needed since the user's posture will not be consistent between measurements or even between moment to moment. The BCG and weight sensor configuration used for each prototype are discussed in more detail in the Section 3.6.

In order to ensure that no load is being carried by the hinge, a floating hinge design is utilized. If part of the load was being carried by the hinge, the exact percentage of the total load on the hinge would be unknown, reducing the accuracy of the body weight estimates and accuracy of the BCG amplitude. Furthermore, the BCG force is propagated downward through the torso, so the rear two standoffs on the seat will contain the largest BCG signal. If the hinge was bearing part of the load, this would significantly reduce the BCG signal on the rear two standoffs.

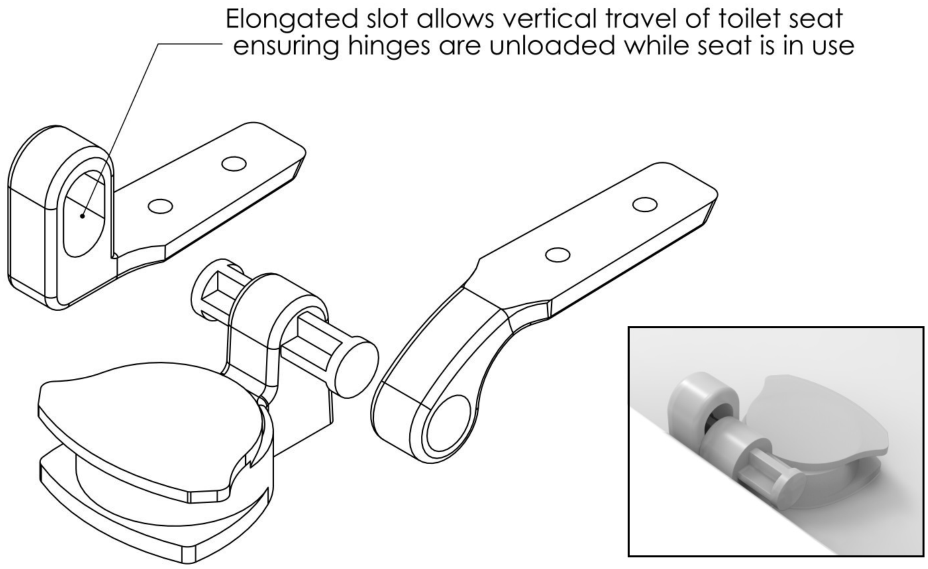

Figure 3.12: The floating hinge has an elongated slot that allows the entire seat to move vertically, but not horizontally. Courtesy of Think Design.

An exploded view of the floating hinge design is showed in Figure 3.12. The floating hinge is designed so that the seat can move up and down vertically, but has no movement in the horizontal direction. This is so that the subject does not feel any movement in the seat when sitting down. Any unusual movement in the seat could reduce patient compliance and acceptance of the FIT seat. This ensures that no load will be present on the hinges when the subject sits on the seat.

Another important part of the seat mechanics is the standoff design. The standoffs must be designed so that all of the load it is bearing is translated to the sensor fixture. Due to the application, the standoffs must allow translation of the force to the sensors while being completely sealed and cleanable. The seat needs to be both waterproof and resistant to cleaning chemicals. The initial design for the standoffs when a FlexiForce sensor is used for both the weight and BCG, is shown in Figure 3.13.

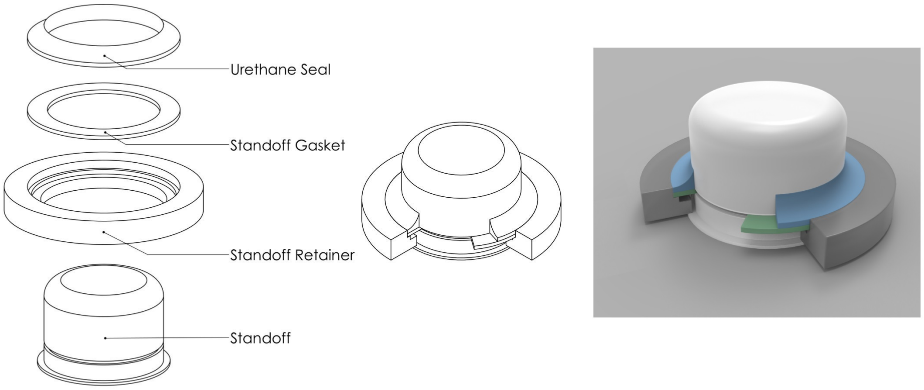

Figure 3.13: The first standoff was designed for use with the FlexiForce sensor. This is a simple mechanical design that transfers all of the force onto the sensor. Courtesy of Think Design

Piezoresistive sensors are built into each standoff for measuring both the BCG and estimated body weight. In order to test and compare the piezoelectric sensors to the FlexiForce sensors, the peizoelectric sensors were added to the normative toilet. They are placed between the standoff and toilet, and are being utilized in compression mode in a custom housing. This results in a total of eight BCG channels that are being captured for each subject.

In the integrated system, rather than using a single piezoresistive sensor to measure the weight and BCG signal, a piezoelectric sensor is used in combination with a load-cell. This requires specialized mechanical coupling that allows the entire force present on the standoff to be translated to both sensors. The internal system that allows this is shown in Figure 3.14, where an insert is used to both support the load-cell and translate the force onto two piezoelectric sensors. Both sensors are connected in parallel and amplified using the same circuitry used with a single sensor (Figure 3.10). This is shown in more detail in

Figure 3.15, which is a rendering illustrating how the force is applied from the standoff, through the load-cell, onto the piezoelectric sensors.

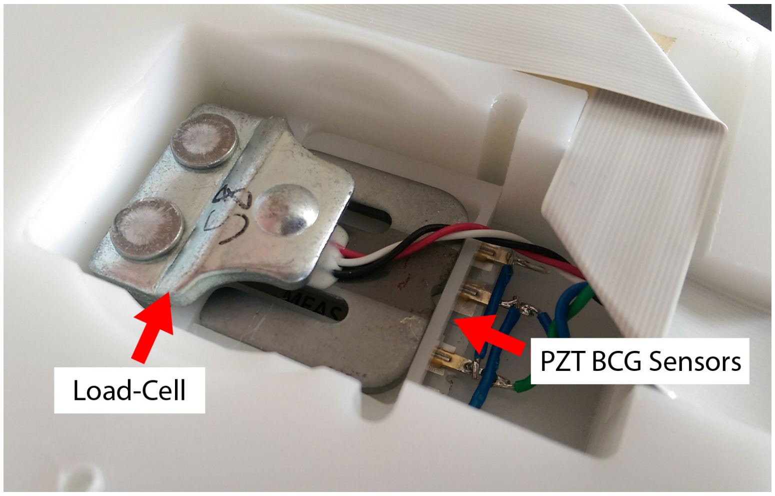

Figure 3.14: The metal load-cell makes direct contact with the standoff. The insert which supports the load-cell then translates the downward force onto the piezoelectric sensors. This image was taken from a bottom view.

Additionally, the standoffs have been redesigned in high-density polyethylene (HDPE) using a press fit design that does not require caulking or adhesive to ensure a water tight seal. The system is also very flexible and consists of a single part, compared the the normative system assembly that contained many different pieces. An exploded view of the new standoff system is shown in Figure 3.16. This advancement is key to improving the signal quality of the BCG, as more of the force is transferred directly to the sensor.

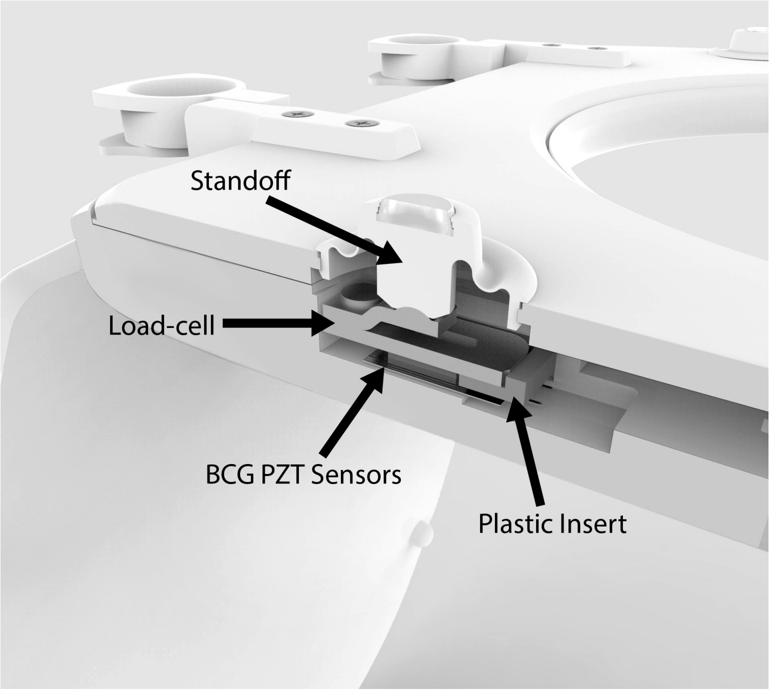

Figure 3.15: A side cutout rendering, illustrating how force is transformed from the standoff through the load-cell to each piezoelectric sensor (one shown as the other has been cut away for rendering). The plastic insert insures that the force is only applied to the sensor, rather than through the internal structure of the seat. Image courtesy of Think Design.

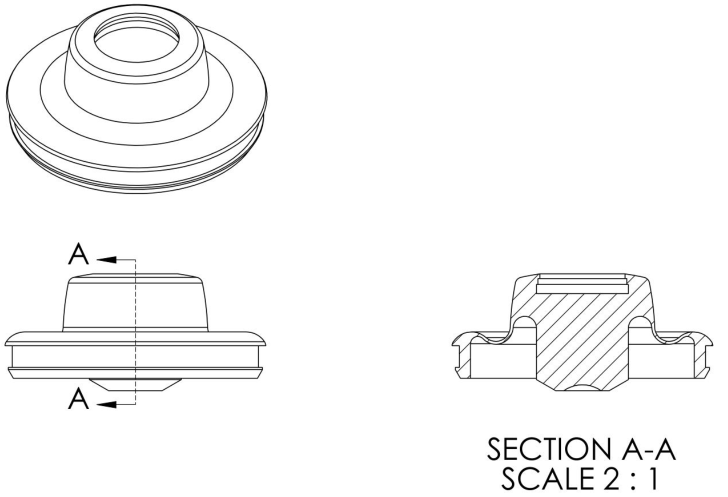

Figure 3.16: The updated standoff design for the in-hospital version of the FIT seat utilizes a single flexible piece that is press fit into place. The seat is water tight and does not dampen the BCG signal, as was the case with the normative standoff system. Courtesy of Think Design.

3.5 Hardware and Sensor Validation

3.5.1 Blood Oxygenation Testing

The reference SpO_2 is plotted against the FIT seat R-value for two subjects with different body types in Figure 3.17. The slope of each R-curve varies by approximately 10% between subjects. The slope is also in agreement with one found in literature with a slope of -33.3 using similar wavelengths [92]. While the variation in slopes is relatively small, the R-value intercept that corresponds to 100% SpO_2 had a large variation, requiring that a single point calibration per subject be made.

Using a single point calibration, the worst case error for subject 2 (using an averaged R-curve slope) is 1% for every 10% deviation from the calibration point. As an example, a value of 91% could be reported for a true value of 90%, and 82% for a true value of 80% if the calibration point was taken at 100% SpO_2. If the single point calibration is not performed and instead the average R-value curve between both subjects is used, then subject 2 would report 94% for a true value of 90%, and 86% for a true value of 80%. This error is too high for practical use, leading to the conclusion that a single point calibration per subject is necessary.

Commercial pulse oximeters do not require a calibration per subject, but also have the advantage of measuring on the finger or ear where there is less tissue variability between subjects. There are two possible explanations for FIT seat variation between subjects: the FIT seat's PPG design or the choice of measurement location. To determine the underlying cause of this variation, FIT seat R-values from the finger and buttock are captured from three subjects. The R-values obtained from the seated thigh test had large variability

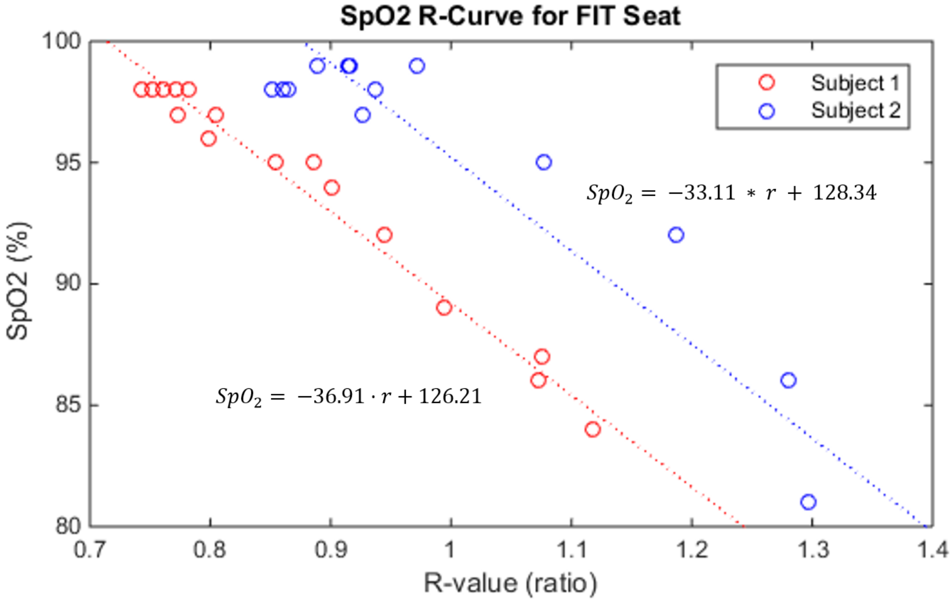

Figure 3.17: The R-curves for two subjects on the FIT seat is shown. Both slopes are in close agreement with literature, however the offset is different enough to require a per-subject single point calibration.

between subjects as expected, but the finger test results fell within a very narrow range of values for all subjects. These results are shown in Table 3.1. This indicates that the need for a per-subject calibration is due to measurement location and not the FIT seat pulse oximeter design. It may be possible to derive this calibration from the subject's body mass or weight, which will be investigated in future work.

	Subject 1	**Subject 2**	**Subject 3**
Buttock	0.58	0.73	0.86
Finger	0.90	0.92	0.93

Table 3.1: Finger R-values compared to the buttock R-values between three healthy subjects, all at an SpO_2 of 99%, showing very a small variation in finger R-values relative to buttock R-values between subjects.

Due to the need for a single point calibration per subject, SpO_2 cannot be verified using the data gathered from normative testing. Additionally, all normative subjects were healthy and as such, have very stable SpO_2 percentages across the entire duration of the normative test. This results in a single SpO_2 point per subject, making it only useful for calibration, not verification. No additional SpO_2 results will be presented. Despite this, the presented results indicate that the FIT seat is capable of measuring a subject's SpO_2 using a reflectance mode pulse oximeter, positioned to make contact with the upper thigh.

3.5.2 Weight and BCG Amplitude Calibration

Methods

In the normative FIT seat, four piezoresistive sensors are used to measure both the BCG and static weight. FlexiForce sensors, which are a film based force sensor, were chosen due to mechanical simplicity. A custom test fixture was created to perform accurate static and dynamic force calibration of the FlexiForce sensors. The test fixture used is shown in Figure 3.18 and Figure 3.19, where a static load can be applied simultaneously with a small AC force using standard weights (static) and a custom built solenoid (dynamic). The entire test fixture was placed inside of an electrical and mechanical isolation table for the entire calibration process. The current to force relationship for the custom solenoid was determined using a high-precision force sensor from Futek (LRF400).

The dynamic weight sensitivity at different static loads was determined by performing 4 trials, where each trial consisted of a test at each of 4 static weights: 3.5 lb, 14 lb, 26.5 lb, and 39 lb. The sensitivity in mV/N was recorded for each test and 5 tests were performed at each static weight, alternating 3.5 lb, 26.5 lb, and 51.5 lb tests, for a total of 15 tests. The dynamic sensitivity of each test is then plotted in a scatter plot to determine linearity and conversion factor for weight. Similarly, the FlexiForce sensors were excited with small amplitude AC forces in the frequency range from 1-10 Hz and amplitudes of 0.5-1 N to approximate the ballistic forces of the heart. The sensors were tested to determine the

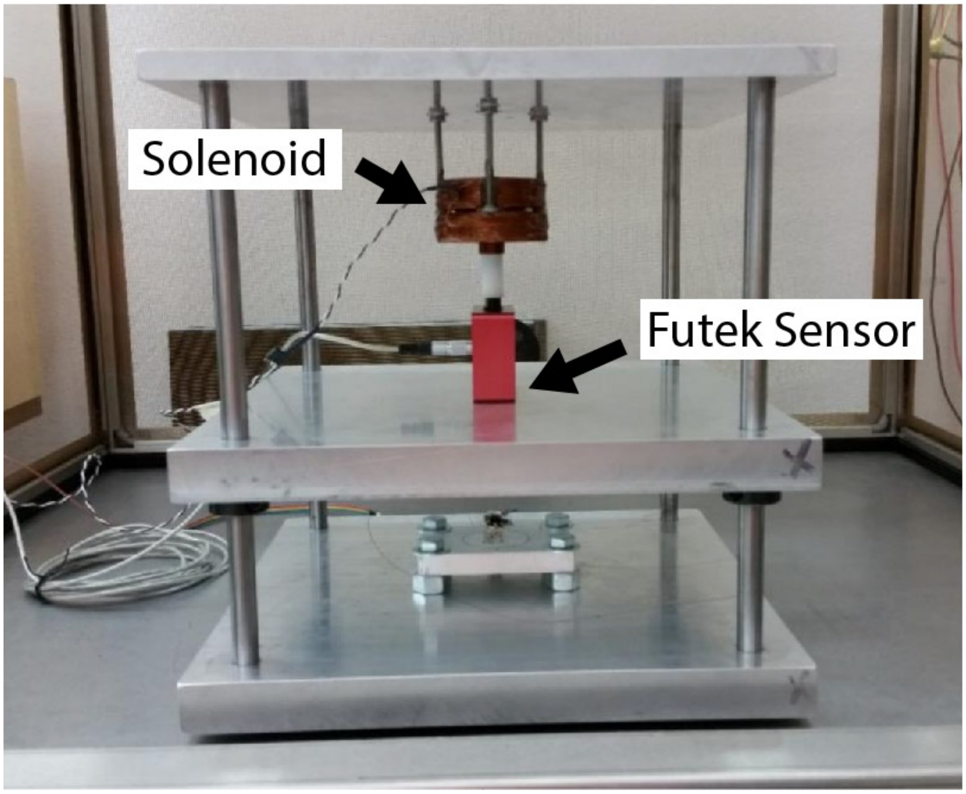

Figure 3.18: Image of test fixture used for calibration, while the solenoid current was calibrated to force using high-precision Futek LRF400 1lb force sensor.

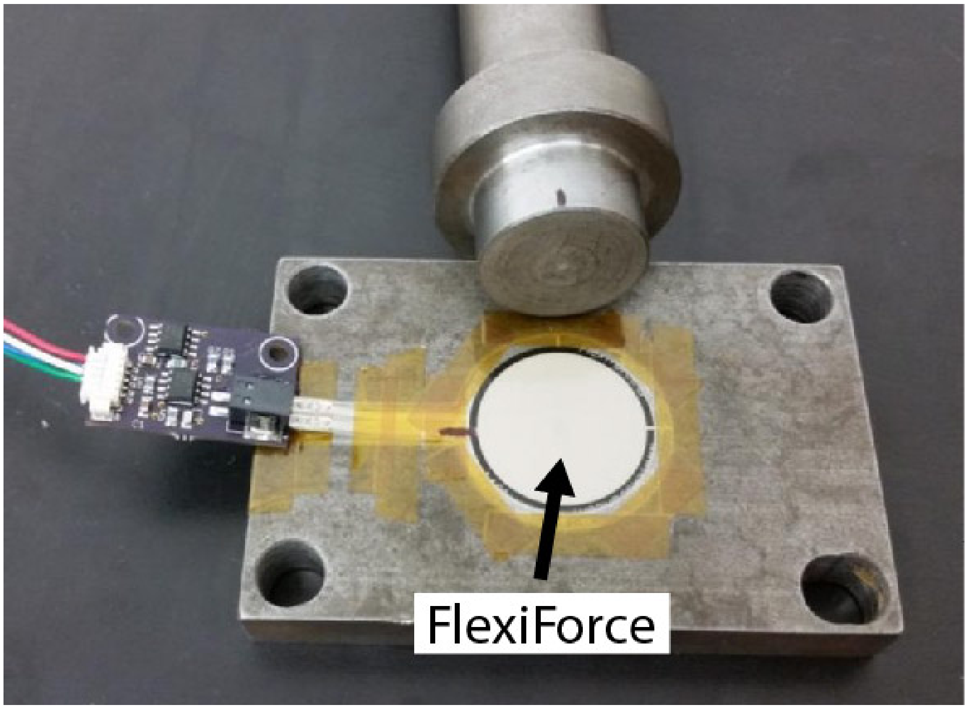

Figure 3.19: Test fixture for exerting force on the FlexiForce sensor and to keep it at a consistent location throughout testing.

dominant sources of error, and to provide a calibration to convert from the sensor voltage output to units of force.

Results and Discussion

The static weight sensitivity was determined by performing 4 trials, where each trial consisted of a test at each of 4 static weights: 3.5 lb, 14 lb, 26.5 lb, and 39 lb. The average magnitude of the static weight sensitivity for the FlexiForce sensor is shown in Figure 3.20. The results indicate that the sensor's sensitivity to dynamic forces are not dependent on the static weight.

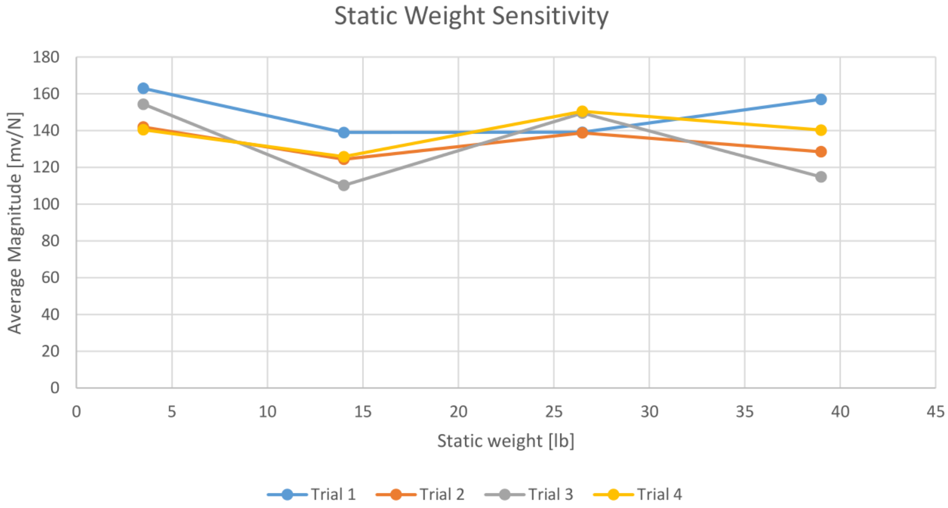

Figure 3.20: Static weight sensitivity for the FlexiForce sensor across multiple trials demonstrates that the static weight present on the sensor does not impact the amplitude of the measured dynamic force.

The transfer function found theoretically from analysis of the FlexiForce sensor circuit accurately matches that measured by the test setup, as shown in Figure 3.21. The theoretical transfer function is calculated for each stage: the front end (assuming no capacitance for the PRT), the high-pass filter, and the amplification stage. Using the maximum gain in the passband, the output voltage can be converted accurately to newtons by multiplying the output by the constant 690 N/V. By converting the BCG to newtons, accurate comparisons can be made between subjects and between different versions of the FIT seat. Furthermore, amplitude comparisons between subjects can now be made with confidence.

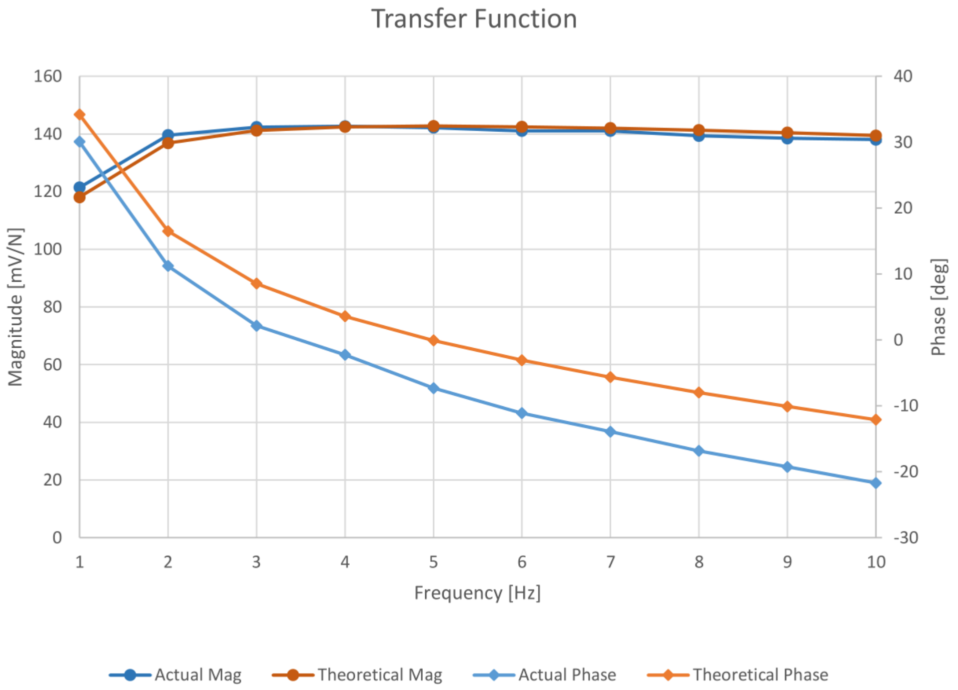

Figure 3.21: The measured (actual) verses theoretical transfer functions for the Flexiforce sensor for small dynamic forces are closely aligned, with a small phase error across the range of tested frequencies.

3.6 FIT Seat Versions

While the final version of the FIT seat is capable of in-home deployment for long periods of time, earlier version of the seat brought the design from proof-of-concept to the final in-home version. The first prototype functioned as a proof of concept, verifying that the ECG, PPG, and BCG can be measured from an individual while seated on a toilet. The first completed system was the normative system, which was used for normative subject testing. Both the in-hospital and in-home systems are completely integrated and are self-contained.

The in-hospital system was used for heart failure testing, while the in-home system is the final design that could be used for in-home deployment. Table 3.2 details the purpose, capabilities, and key improvements for each design. Each of these systems are discussed in detail throughout this chapter.

System Name	**Description**	**Improvements**
Proof of Concept	Demonstrate feasibility of measuring signals on the buttocks. Outputs analog bECG, bPPG, and BCG waveforms simultaneously.	N/A
Normative System	Used for normative subject testing. Outputs the bECG, bPPG, and BCG waveforms in addition to temperature, and weight. DAQ is performed using an NI DAQ.	Significant signal quality improvements as well as the first system integrated into a toilet seat.
In-Hospital System	Used for in-hospital testing with HF subjects. Self-contained system for interfacing directly with a PC via USB.	Battery powered, with integrated DAQ capabilities, and further instrumentation signal quality improvements.
In-Home System	Used to acquire daily cardiac measurements in the home for an extended period of time. Self-contained system with long battery life that wirelessly interfaces with an Android device.	Added BLE, on-board data storage, automatic recordings, battery life improvements, as well as a load-cell BCG and increased ECG gain..

Table 3.2: Iteration Overview

3.6.1 Proof of Concept Seat

The first prototype was considered a proof of concept. This version of the seat was used to demonstrate the feasibility of measuring the ECG and PPG on the buttocks. The prototype consisted of a machined MDF toilet seat purchased at a local hardware store, as seen in Figure 3.22. Slots were milled out for active ECG electrodes and a PPG PCB. The hinge of the seat was removed for testing so that it did not bear any load, and the standoffs were used as is. The force sensors were placed underneath the standoffs on the actual toilet in order to verify that the BCG can be measured when in a seating position. The ECG, PPG, and BCG signals were acquired using the Biopac MP150 data acquisition system.

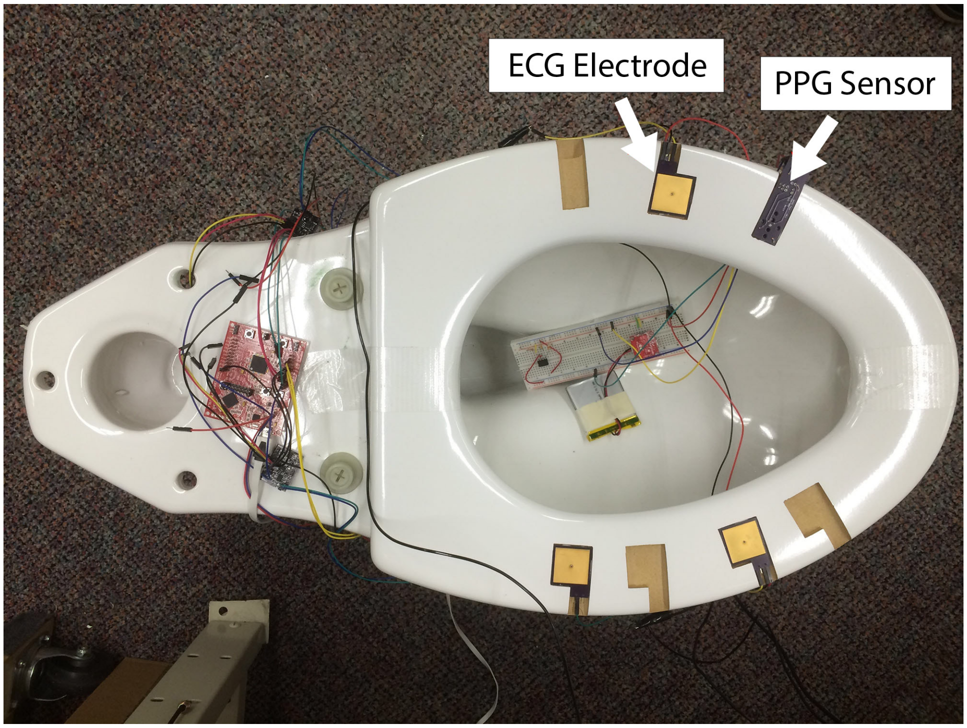

Figure 3.22: The first proof of concept FIT seat was created from a machined MDF seat that was purchased from a local hardware store. The ECG and PPG were placed on the surface of the seat for testing.

Multiple slots were milled so that different locations for the PPG and ECG could be tested. The dry, active ECG electrodes were integrated into the circuit board using the schematic shown in Figure 3.4. The electrode is an exposed copper pad that makes contact with the subject. The PPG tested at this stage contained only a single wavelength, which was 940 nm (IR) and utilizes the schematic shown in Figure 3.5. The FlexiForce sensor instrumentation (Figure 3.9) was built up on a breadboard that sat inside of the toilet, as shown in Figure 3.22.

3.6.2 FIT Seat for Normative Study

The second prototype was designed for the normative subject testing that took place at the Rochester Institute of Technology. Normative subject testing is described in Chapter 5. This version of the seat was machined from a solid piece of high-density polyethylene (HDPE). The normative seat is battery powered using a rechargeable lithium battery, which is regulated to a 3.3V output. The ECG electrodes are built into the seat, as is a window for the PPG sensors and the IR temperature sensor. The floating hinge and standoffs are both used in this prototype. The signal are all acquired via a National Instruments DAQ, resulting in a large number of wires between each instrument and the DAQ system. This system is not suitable for in-home testing. Channels were machined on the bottom of the seat for the wiring. A rendering of this seat can be seen in Figure 3.23 and pictures of the actual seat can be seen in Figure 3.24.

The PPG consists of two completely separate channels, red and infrared. In order to remove the need for an embedded system in this prototype, both the red and IR LEDs were left on continually and optical filters were used to separate out the two channels. Each wavelength is then able to be measured using two parallel sets of instrumentation. The circuit board with four LEDs (two for each wavelength), the photodiode, and associated instrumentation is shown in Figure 3.25

The buttocks based ECG (bECG) is integrated into an elongated toilet seat with dry electrodes on the surface and electronic instrumentation inside of the seat, as shown in Figure 3.26. Three electrodes, differential pair and right leg reference (grounded), each with a diameter of 28 mm. Stainless steel electrodes are chosen for their non-corrosive, and non-irritant properties. The differential electrode pair is placed on the seat such that skin contact is made in close proximity to the gluteal fold when seated. A grounded right leg electrode

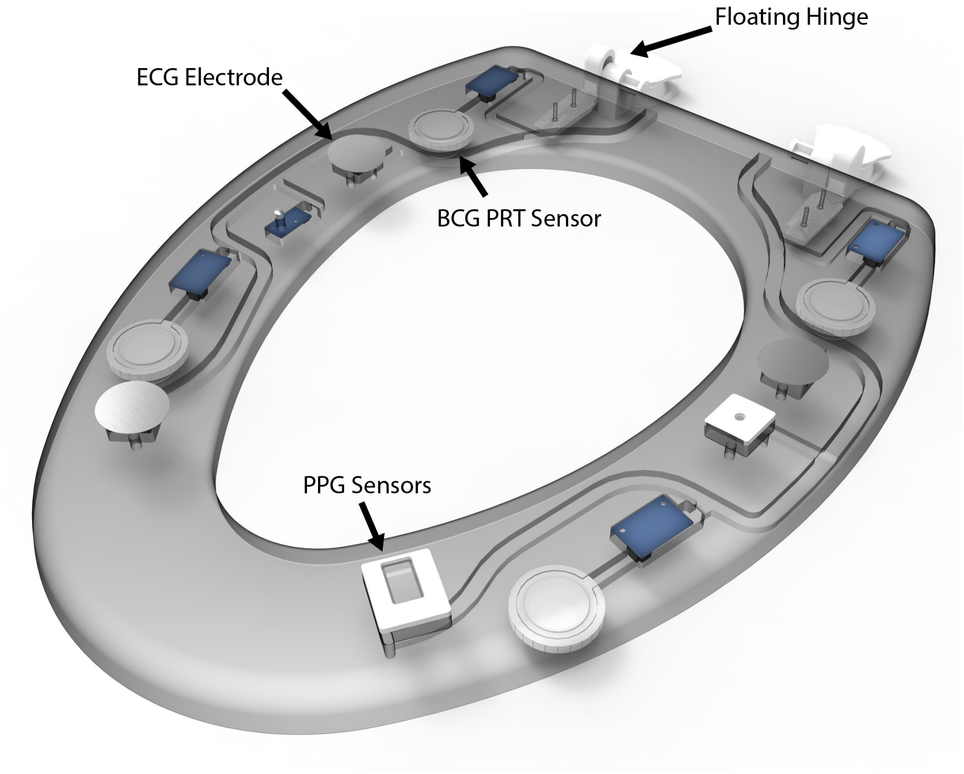

Figure 3.23: The CAD rendering of the normative FIT seat shows where each sensor is located on the seat as well as the standoffs and hinges.

is placed approximately 12 cm below the differential pair on the right side of the toilet seat, as illustrated in Figure 3.26. Each electrode is securely fixed to the toilet seat using epoxy to ensure repeatability across recordings.

Active front-end instrumentation is integrated inside of the seat and connected to each the differential stainless steel electrodes with welded wires, resulting in a maximum distance of 10 mm between the electrode and the front-end instrumentation. The active electrodes are powered by a 3.3V boost converter, which in turn is powered by a 3.7V (nominal voltage) rechargeable lithium polymer battery. The active electrodes also contain ESD protection and a high-pass filter with a -3dB cutoff frequency of 0.16 Hz that removes any DC bias present on the body, ensuring that the signal is within the valid input voltage range. The output from each active electrode is differentially amplified using the ECG instrumentation (ECG100C) within a Biopac MP150 system (Biopack Systems, Inc., Goleta, CA), which

Figure 3.24: Picture of the seat used for normative testing is shown. The top view is on the left, the bottom view is in the center, and the sealed up bottom is on the right.

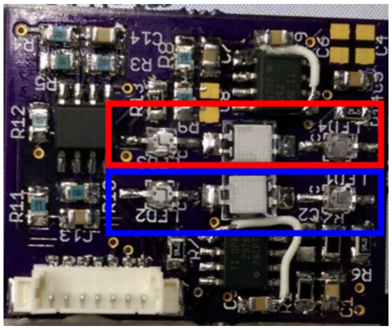

Figure 3.25: The circuit board used for the normative PPG contains four LEDs (two for each wavelength), and two sets of photodiodes with matching instrumentation. The photodiode and LEDs for each wavelength is shown in a red and blue box. The analog signal is then amplified and filtered further on a main PCB (not shown).

is also used to gather a 12-lead gold standard ECG. All signals are then acquired using an NI CompactRIO Data Acquisition System (DAQ), which is controlled by a laptop. The toilet seat with integrated electrodes and active ECG front-end instrumentation is secured to an elongated toilet mounted to the floor. A schematic overview of the system is shown in Figure 3.26. All devices that are not battery powered are plugged into a medical grade isolation transformer (ILC-1400MED4) to ensure electrical safety.

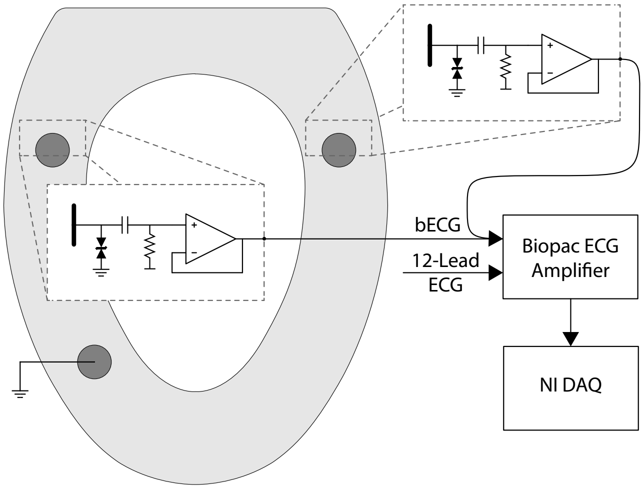

Figure 3.26: Stainless steel electrodes are integrated into the seat and are connected directly to the integrated ECG analog-front-end. The output of each front-end is low impedance, allowing for a low noise connection to the differential ECG amplifier inside of the Biopac MP150 system. The resulting full-scale ECG signal is acquired on a NI DAQ.

3.6.3 In-Hospital Heart Failure FIT Seat

The third prototype was used for the in-hospital testing, and is considered the first integrated version of the seat. It is be powered by a high density primary lithium battery and performs all data acquisition on-board. The seat incorporates a synchronization signal output that will allow the data captured on the seat to be synchronized to the commercial medical instrumentation. While wireless capabilities were built into the hardware, all in-hospital heart failure subject data is acquired via a USB connection.

The block diagram for the integrated system is broken into two separate sections, a digital block that is shown in Figure 3.27 and an analog block that is shown in Figure 3.28. This organization mirrors the physically assembled seat, which has physical separation between the digital PCB and the analog PCB in order to facilitate isolation. An image of the in-hospital seat is shown in Figure 3.29. The final system is completely self contained, and is easily made waterproof with silicon caulk.

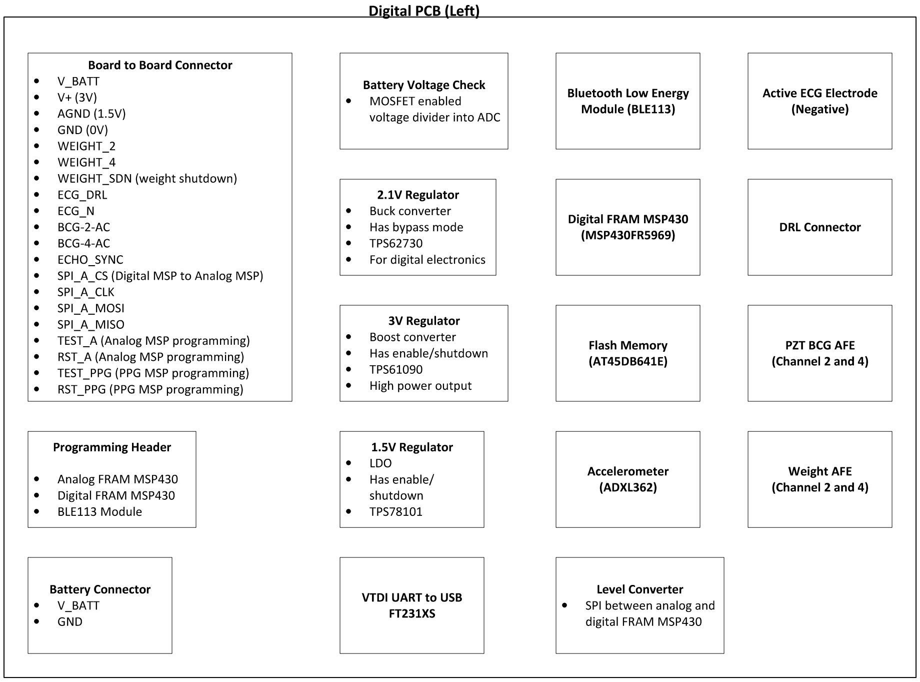

Figure 3.27: The digital side of the integrated system is shown in this block diagram. This system consists of the digital control circuitry, wireless BLE module, flash memory, and an accelerometer.

The analog block consists of the instrumentation and data acquisition circuitry. The ECG instrumentation utilizes an ECG AFE from Analog Devices, the AD8232. The right leg electrode is configurable for either a ground electrode or a driven right leg. The PPG consists of a single photodiode and AFE with configurable LEDs. The current for the red and IR LEDs will be software configurable, allowing for variable intensities. The BCG will be measured using a two piezoelectric sensors under each standoff (LDT0-028K from Measurement Specialties), and the static weight will be measured using a separate load-cell (similar to what is found in a bathroom scale). The ECG, PPG, and weight from unmarked load-cells from SparkFun Electronics are acquired using the analog MCU's built in 12-bit ADC (MSP430FR5969). The BCG is acquired using a separate 24-bit precision ADS1220 from Texas Instruments. This allows the BCG to have a higher dynamic range, making it

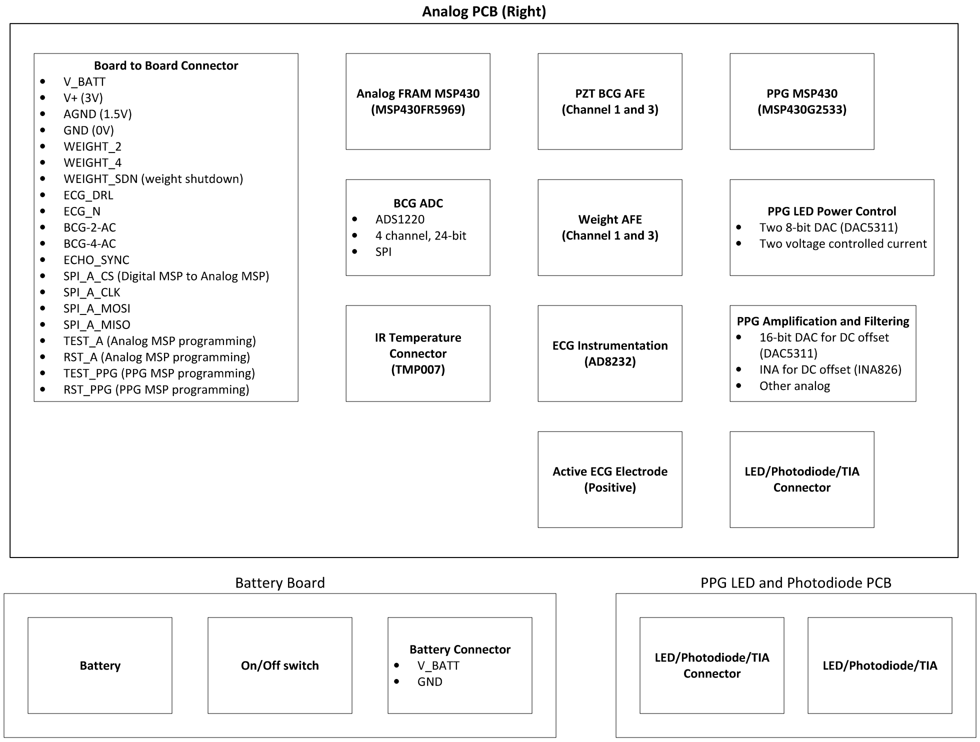

Figure 3.28: The analog side of the integrated system is shown in this block diagram. This side of the system consists of the data acquisition circuitry, the PPG instrumentation and the ECG instrumentation.

more robust to subject induced motion artifacts and ambient motion artifacts.

The major changes in instrumentation in the integrated system compared to the normative system include the PPG circuitry and the standoffs. The standoff mechanical design has been discussed previously in this chapter.

The PPG in this seat utilizes a pulsed LED based system with active DC cancellation, requiring a dedicated embedded control system. An MSP430 MCU is used to control the LED and sample the output from the AFE circuit. When a sample must be captured, the MCU first turns on the desired LED (red or IR), waits for the AFE to stabilize (which is approximately 300 µs based on the instrumentation chosen), then it initiates the ADC for

(a) (b) (c)

(d) (e) (f)

Figure 3.29: The in-hospital integrated version of the FIT seat is self-contained with all electronics and sensors inside of the seat. The seat is cleanable and the surface has no rough edges or crevices. Images of a completed seat and the 3D CAD renderings are shown (courtesy of Think Design).

sampling the signal. Once the signal has been sampled, the LED is turned off. The overall duty cycle of the LED is approximately 5 % when a sample rate of 256 Hz is used. This significantly reduces the power consumption of the PPG AFE, and thus the entire system. The PPG window, which consists of four LEDs (two red and two IR) and a photodiode is shown in Figure 3.30.

Due to the measurement location of the bPPG, the scattered signal has much less intensity than if the sensor were operating in pure reflectance mode. The reduction in signal intensity is approximately 100 fold compared to using the same sensor on the finger. A typical ADC

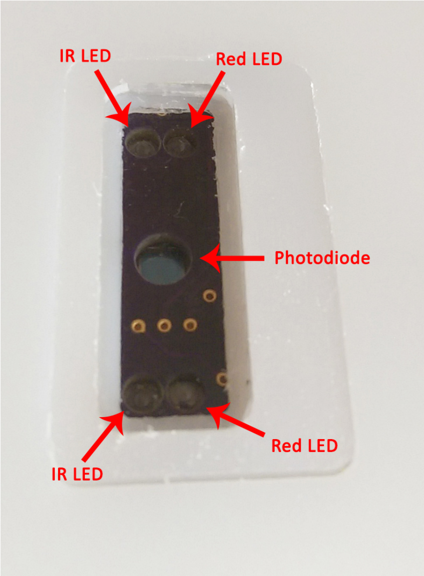

Figure 3.30: The PPG window allows light to enter the body from two out of the four LEDs depending on which wavelength is currently active. The window also allows the reflected/scattered light to be sensed by the photodiode at the center.

is not capable of measuring the DC offset on the output of the transimpedance amplifier, so the output of the 16-bit DAC used for DC compensation is used as the gold-standard. The signal is then amplified with a gain of 301 V/V before being digitized in order to maximize signal to noise ratio (SNR). In order to measure SpO_2, both DC and AC amplitude information is required. The DC output of the DAC is multiplied by 301 and then added to the AC signal acquired from the ADC in order to create an accurate measure of intensity.

3.6.4 FIT Seat for In-Home

The fourth and final prototype will be used for future studies, including the 6 month in-home testing for normative and heart failure subjects. It is very similar to the integrated system (third prototype), but will contain separate firmware which does not have USB connectivity and increases the power efficiency of the system. The main functional difference is that the device is be completely wireless and automatically detect use using an accelerometer and load-cells. Once the systems determines that an individual is using the seat, it automatically starts acquiring the desired signals until the subject stands up and weight is removed from the seat. All of the data captured is sent to an Android or Raspberry Pi base station via an on-board Bluetooth Low Energy (BLE) radio, which will in turn, transmit the data to a secure server.

The digital circuitry is in an always on state and handles all communication and data transfer. It contains an on-board flash module for storing recordings and an accelerometer that allows motion wake-up of the entire system if desired. Additionally, the digital circuitry sends out a synchronization pulse to the Biopac system every second to allow for both systems to be synchronized post-acquisition. The data captured on each FIT seat will ultimately be stored on a secure server, regardless of the acquisition method. The secure server is accessible to a number of devices and software tools, including Python and MATLAB. A schematic overview of this data flow is shown in Figure 3.31.

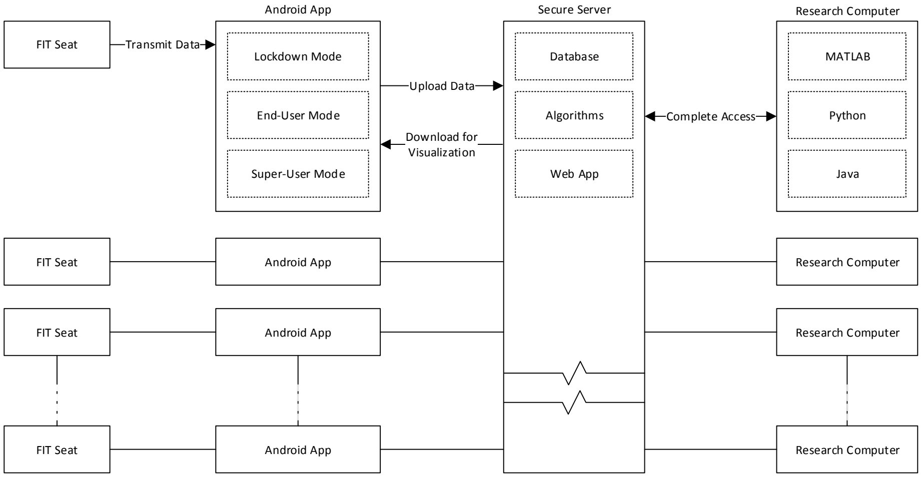

Figure 3.31: Many devices will have the access to access the FIT data from the secure server. The FIT seat will transmit this data to the secure server via an Android device.

Based on the most recent integrated system design and firmware, the overall data rate for the FIT seat is 4614 bytes per second (bps). The channels are shown in Table 3.6.4.

	Channels	Sample Rate	Bit Resolution	Bytes/Second
bECG	1	512 Hz	12-bit	1024 bps
bPPG	2	128 Hz	24-bit	768 bps
PZT BCG	4	128 Hz	24-bit	1536 bps
LC BCG	4	128 Hz	12-bit	1024 bps
Weight	4	32 Hz	12-bit	256 bps
Temperature	3	1 Hz	14-bit	6 bps
Total	18	-	-	4614

Table 3.3: The total data generated by the 18 data channels in the FIT seat is 4614 bytes per second. This does not include any data captured on external commercial medical devices such as the Biopac system.

Assuming approximately 10 minutes of use a day on the FIT seat, the total data generated per day per FIT seat is 5.5 MB. Throughout the duration of a six month in-home trial, subjects will generate approximately 0.5 GB of raw, unprocessed, data. Given an expected usage of 10 minutes per day, the battery life of the in-home system can be estimated. There are essentially two different operating states for the FIT seat, sleep mode and recording mode. The FIT seat will spend most of the time in sleep mode since it is expected that the seat will be in use for less than 10 minutes a day on average. In this mode, the FIT seat will need to be able to communicate with the base station as well as automatically recognize when a user sits down (which will put the seat in recording mode). To achieve the lowest possible sleep mode power consumption, FRAM based MCUs have been used in addition to the best in class ultra-low power accelerometer and Bluetooth Low Energy.

The FRAM based MSP430 (MSP430FR5969) from Texas Instruments consumes 0.5 µA in sleep mode with real-time clock (RTC) [93]. The ADXL362 accelerometer from Analog Devices consumes 0.27 µA in sleep mode with motion wake-up [94]. The BLE113 module from Bluegiga utilizes Texas Instruments ultra-low power radio CC2541. The power consumption of this device with advertisement and in sleep mode is approximately 0.9 µA [95]. This results in a theoretical power consumption limit of approximately 1.7 µA in shut-down mode. This has been verified with direct measurements, where the entire system sleep current is 1.85 µA. To achieve this theoretical limit, the rest of the circuitry in the device is completely shut down or placed in a low-power deep sleep mode when available. This is made possible through a modular circuit design with a highly customized embedded system that can turn on and off different blocks as needed.

The second main contributor to the overall power consumption of the system is the analog electronics and data acquisition circuitry during the recording mode. Using ultra-low power operational amplifiers (OPA) and instrumentation amplifiers, the expected quiescent current will be less than 1 mA. This estimate assumes 14 OPA channels that utilize 50 µA each (OPA2313) and 5 INAs that utilize 40 uA each (INA2321) [96, 97]. Due to the low quiescent current of the analog circuitry, required to run the PPG LEDs will dominate during the recording mode. If the LEDs require a current of 150 mA when on and they are pulsed at a duty cycle of 5%, the resulting an average power consumption is 7.5 mA per wavelength.

The overall system power consumption is estimated in Table 3.4. This table takes into account the sleep current and the recording current for each of the main components. The efficiency of the voltage regulators are not taken into account in order to simplify the estimate. Assuming that the seat will be in use for 10 minutes a day, the overall daily average power consumption is 1.55 mW. The integrated seat has been designed to hold a 3000 mAh primary lithium battery with a nominal voltage of 3 V. Without using compressed sensing for the PPG, this would result approximately 242 days, or 7.9 months of theoretical battery life.

	Active			Sleep	Daily	
	Power Management	**%/Day**	**Average**	**Power**	**Average**	**Percent**
Power	0.18 mW	2.77%	4.9 µW	0.43 µW	5.35 µW	0.34%
BLE112	10.5 mW	5.55%	0.58 mW	2.55 µW	0.59 mW	37.76%
MSP430FR5969	0.42 mW	1.39%	5.8 µW	0.74 µW	6.57 µW	0.42%
ADXL362	6.3 µW	1.39%	0.087 µW	0.79 µW	0.89 µW	0.06%
AT45DB641E	14.7 mW	0.24%	35.9 µW	0.3 µW	36.2 µW	2.33%
Analog	66.0 mW	1.39%	0.92 mW	0 mW	0.92 mW	59.08%

Table 3.4: Estimated Integrated System Power

A deployed FIT seat has many use-cases, allowing different individuals access to data in the cloud. In addition to the subject being able to access their data through a custom built Android app, doctors can theoretically have direct access to the subject's data either via a web app or a similar Android app. Furthermore, researchers can access the data using MATLAB or Python for advanced analytics. This can lead to cloud based analysis where the subject, their physicians, and their family can be warned of a decline in cardiac health using only automated algorithms. This will allow for subject intervention, reducing the likelihood of hospitalization and cardiac events such as sudden cardiac death and heart attacks despite having a large number of deployed devices. There are many use cases that become feasible given this design.

3.7 Use-Cases and User Adoption

There are four main use cases for the FIT seat. The first is with managing cardiovascular disease for individuals that have already been diagnosed (e.g., with heart failure). The seat can be used to reduce the number of yearly doctor visits while also providing an early warning system for changes that could be detrimental to ones health. A similar use case is for those who have a family history of cardiovascular disease. The seat can then be used for determining the current risk of cardiovascular disease. It can also be used to prevent or provide warning of unexpected cardiac events, such as a heart attack or sudden cardiac death.

The third potential use case for the FIT seat is for the monitoring of the elderly, such as one's parents or grandparents. In this case, the measurements from the FIT seat can be used to determine if medication is being taken, monitor weight gain or loss, and monitor cardiac function over time. Finally, the last presented use case is for parents interested in monitoring their young children or children interested in monitoring their elderly parents. This unexpected use case was discovered during the ethnographic in-home interviews. Many parents were interested in automatically monitoring their children's weight and stress levels (through HRV). A schematic overview of many of these use cases, and the types of individuals a subject would like to have access to their data is shown in Figure 3.32.

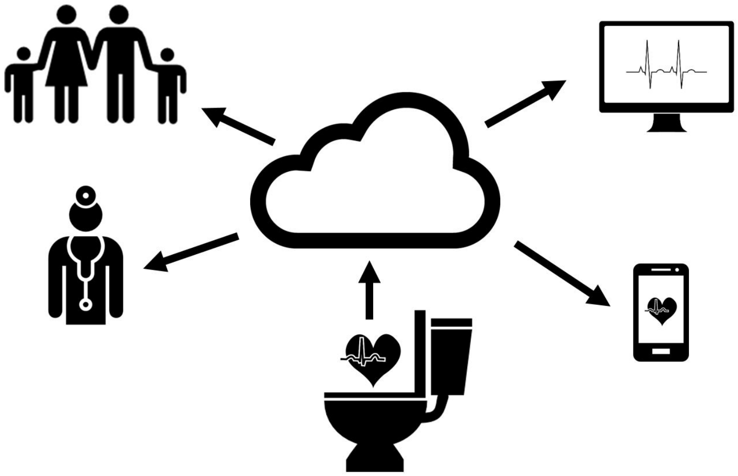

Figure 3.32: The cardiac data captured from the FIT seat can be used by individuals to self monitor their cardiac health, physicians to monitor patients, and even used by family members to monitor their loved ones.

This system has the potential to change how a consumer's cardiac health is monitored. The use of the BCG provides novel insights into cardiac function that were previously not available without the use of an ultrasound machine, requiring a visit to the doctors office or hospital. In comparison to the new wave of wearable medical devices that only use ECG or PPG to monitor ones HR and HRV, this system contains a multitude of sensors than can be used in combination to provide a large breadth of measurements. Additionally, the FIT seat is used while a subject is sitting down and stationary, compare to a wearable device that is prone to motion artifacts when worn on the wrist

The major obstacle for realizing the full utility of this device will be user adoption. This was specifically invested during the early stages of the project through in-home interviews with 22 individuals. Through the use of a professional ethnographer from Storyline, user adoption of this technology was gauged. Three key criteria for this study are outlined below.

There are 16 quotes that highlight the results from this market research:

1. “I think the benefits of it may be bigger than they expect.”
2. “Right now, I don’t need [the FIT], but it’s nice to know that you could go out and get one if you had to.”
3. “They’re my parents and I don’t want them to die.”
4. “This is definitely a unique concept for remote patient monitoring.”
5. “[It] just seems so radical.”
6. “There’s not one person in the world who doesn’t sit on a toilet.”
7. “I would like to track and make sure I’m still healthy all the time. Make sure I’m healthy and not dying slowly.”
8. “It should just know when my behind sits on it.”
9. “If the doctors buy in and see value to it, then they’re going to have a lot more influence.”
10. “Whatever it is, catch it early.”
11. “I might not have to go to the doctor’s every three months.”

12. “Who cares if someone knows your blood pressure?”
13. “I just don’t want people feeling weird . . . wondering ’what is that?’”
14. “What are these lines? You ain’t clean your toilet seat?”
15. “They need to think outside of what they’re sold on; which is the butt.”
16. “When do they come out? Can I be the first to know?”

These results highlight some of the key challenges, necessary features, and potential pitfalls of this seat from a user-adoption standpoint. Generally, the device was well accepted by individuals. Both privacy and how inconspicuous the device is are the most important issues that must be overcome. Furthermore, user adoption will be much greater if physicians support the device and can aid in the monitoring of an individuals health.

3.8 Conclusion

The presented fully integrated toilet seat for cardiovascular monitoring is the first self-contained, deployable device that can measure ECG, BCG, and PPG waveforms from a subject in his or her home. The final version of the FIT seat is waterproof, cleanable, self-contained, and easy to install. It requires no subject interaction when taking measurements, allowing the system to be easily integrated into one’s habits. The FIT seat shows promise within the health-care industry and within the consumer market.

The FIT seat will be verified using two rounds of human subject testing, with both normative and heart failure patients. While in-home studies are not presented herein, the FIT seat will be used for future studies both in the home, in the lab setting, and in the hospital. This work paves the way for future studies by creating a robust tool for medical data acquisition in the home, leading to innovations in biomedical signal processing, medical trend studies, and personalized, preventative cardiology.

Chapter 4

Algorithms and Signal processing

4.1 Introduction

Advanced algorithms are integral to the success of the FIT seat due to the non-standard location on the body and the type of sensors utilized. Many custom algorithms were developed for use with the FIT seat, focusing on signal quality algorithms and best-in-class feature delineation algorithms. Additionally, this chapter details the verification of the present algorithms independent of the FIT seat, in order to ensure that no bias is introduced when using these algorithms to verify the data captured from the FIT seat. These automated algorithms are required for the adoption of the FIT seat, since the amount of data acquired is well beyond what can be manually analyzed by trained experts.

4.2 Automated Analysis Overview

Parameters are extracted from the FIT seat data in a similar process for all studies. The extracted parameters are then analyzed as needed for each study. Analysis starts by defining all of the recordings that need to be processed by specifying restrictions for querying data in the secure database. Analysis parameters include a list of recordings to analyze and signal and channel specific parameters, such as which channel will be used as a gold-standard and which channels should be analyzed. All channels are then scaled as needed to convert the normalized voltage signals to the correct units, such as newtons (N) for BCG.

The first step in analysis is the most critical: signal quality classification. Since the data acquired from the FIT seat is not always acquired in a controlled environment, poor quality sections of the signal need to be rejected. This ensures that noise and other artifacts do not impact the extraction of important medical parameters, which could have a detrimental effect on the conclusions drawn from the recordings. Regions within the captured waveforms that are not of sufficient quality are not analyzed.

The beats within the remaining regions are then delineated using signal specific feature delineation algorithms. The most prominent feature captured by the FIT seat is the R-peak in the bECG. The R-peak is subsequently used by many of the other channels as a robust reference point. Beat-by-beat measurements, such as HR and HRV are calculated from the beat delineation.

Before ensemble averaging, each beat undergoes a second set of signal quality checks, where poor quality beats are not included in the ensemble average. After the ensemble averaged waveform is generated (Section 4.8), intra-beat features are delineated (e.g., T-wave) and intra-beat timing intervals and amplitude parameters are extracted (e.g., QRS

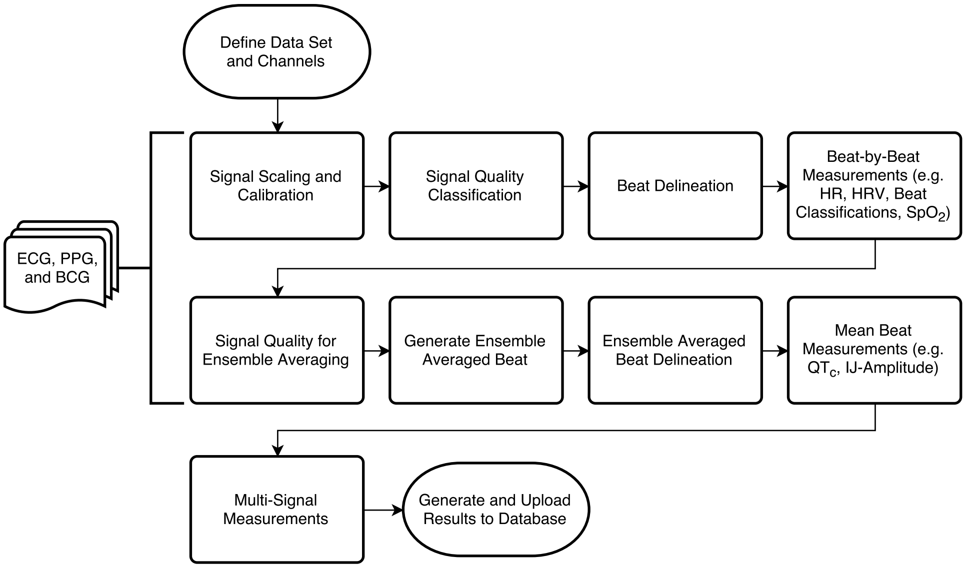

Figure 4.1: Analysis of all FIT seat data undergoes a similar process. After specifying which recordings will be analyzed, signal quality is used to reject sections of poor quality waveforms. Beats are then delineated, which are used to generate ensemble averaged beats.

duration). After each waveform is analyzed, multi-signal measurements are calculated (e.g., pulse transit time). An overview of this process is shown in Figure 4.1.

4.3 Signal Quality

4.3.1 ECG

Rejecting regions of poor signal quality is necessary for accurately analyzing the bECG as it is more prone to noise and motion artifacts than traditional ECG systems. Custom algorithms were developed to automatically assess signal quality and reject noisy waveform segments using two signal quality indices (SQIs): one based on the kurtosis and a second that performs spike detection. The kurtosis is a statistic measure that is commonly used to determine ECG signal quality [98, 99, 100]. The kurtosis is defined as the fourth moment about the mean (μ_4), divided by the standard deviation to the fourth power (σ^4), as shown in (4.1). The kurtosis measures the "tailedness" of a distribution, where a normal distribution has a kurtosis of three. When the kurtosis is lower than three, the distribution under test has longer tails than a normal distribution. Typically, the kurtosis is calculated across a large window of at least 10 seconds and is used to locate large motion artifacts or excessive baseline wander [98]. A clean, sinus rhythm ECG with no motion artifacts nor baseline wander has a kurtosis greater than five [101].

$$Kurt[X] = \frac{\mu_4}{\sigma^4} = \frac{E[(X-\mu)^4]}{(E[(X-\mu)^2])^2} \tag{4.1}$$

To identify waveform segments with excessive in-band noise, a small moving window of 2 seconds is used herein to calculate the kurtosis from a bandpass filtered ECG in order to isolate the QRS complex, with a filter bandwidth of 5-15 Hz. By using a smaller window, the kurtosis measure is no longer dominated by episodic large motion artifact or baseline wander. A kurtosis threshold of 3.6 was empirically chosen for this work based on the normative subject data. A separate, more stringent threshold of 5 was used when generating ensemble averaged beats (Section 4.8). An example of the resulting kurtosis value compared to the threshold of 3.6 for a typical waveform is shown in Figure 4.2.

Large amplitude spikes due to motion artifacts are detected using a second stage SQI. Spikes are identified as an increase in the moving standard deviation, which is calculated using a 2 second window. A threshold of 1.5 times the standard deviation of the entire signal was empirically determined to provide robust rejection of noisy spikes. Figure 4.2 shows an example of the resulting SQI and threshold.

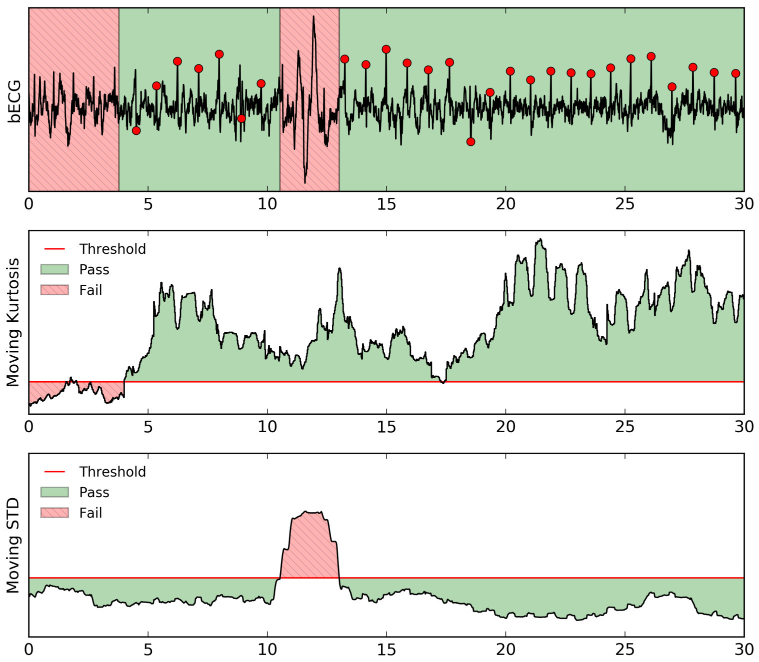

Figure 4.2: Signal quality is calculated using a moving kurtosis and standard deviation. The first signal quality index rejects regions with in-band noise that have a kurtosis below a threshold of 3.6 and the second rejects noisy spikes that have a moving standard deviation greater than 1.25 times the overall standard deviation. R-peak delineations are shown to indicate where each beat is located within regions that have passed the signal quality test.

4.3.2 BCG and PPG

Unlike the ECG R-wave, the BCG and PPG do not have a feature that is clearly defined with a distinct shape. The PPG signal and BCG signal morphology is very similar to motion artifacts, making it challenging to determine signal quality without reference points for each beat. For the FIT seat, a simultaneous ECG will always be available when capturing the PPG and BCG, allowing the R-peak to be used as a reference for every single beat. Both the BCG and PPG use the same algorithm to classify signal quality.

To determine the signal quality of a single BCG or PPG beat, correlation and amplitude based approaches are used to ensure consistent signal quality between beats. Beats that are dissimilar to the local neighborhood are considered poor quality and are not included in ensemble averaging (Section 4.8). Correlation is used to ensure similar shape, while amplitude testing ensures that large shaped motion artifacts are rejected.

The Pearson correlation coefficient is calculated between each beat and the neighborhood ensemble average beat. The neighborhood ensemble average beat is calculated by averaging each of the beats within a 15 seconds (the neighborhood), using the methods described in Section 4.8. The beat under test is not included when calculating the ensemble average. If fewer than 2 beats are within the neighborhood, the ensemble average is not calculated and the beat is rejected. If the beat under test has a Pearson correlation coefficient of less than 0.8 when compared to the neighborhood ensemble average, it is rejected.

Similarly, the amplitude based approach rejects individual beats that do not have a similar RMS value or vary greatly in amplitude compared to the ensemble average beat. The ensemble average is calculated for a neighborhood of 15 seconds. The RMS and the range of the ensemble average beat is calculated for each beat under test. If the RMS of the beat under test is less than 1/4 or more than 2 times the ensemble average RMS value, it is rejected. Additionally, if more than 1/8th of the ensemble averaged beat differs from the neighborhood ensemble average by more than 1/4 of its range, it is rejected.

After undergoing both signal quality checks, the resulting ensemble averaged beat is much cleaner and does not incorporate wildly varying sections of the signal. This is illustrated in Figure 4.3, where large variations in the bPPG impact the mean beat if they are included in the stack during ensemble averaging.

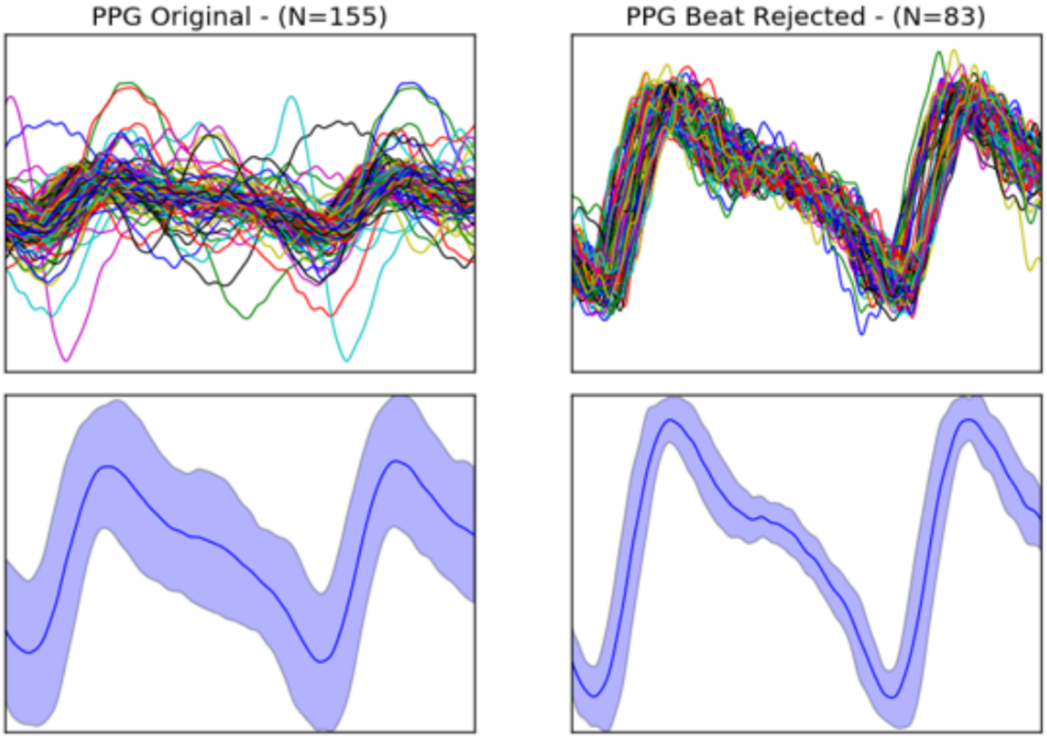

Figure 4.3: By rejecting beats with poor signal quality, the resulting ensemble averaged beat (solid blue line on the bottom) and associated standard deviation (light blue region) contains less smearing and has a higher amplitude accuracy than if every beat was included. This is illustrated using the bPPG, where approximately 46% of the total number of beats are rejected due to poor signal quality. An overlay of all of the beats utilized (top) when generating the ensemble average (bottom) is also shown.

4.4 Beat Classification

In order to compare and verify different delineation techniques and algorithms, a consistent method for benchmarking such algorithms must be utilized. A gold-standard waveform and feature must be used in order to determine the effectiveness of each algorithm as described herein. A gold-standard can be either a hand-annotated dataset or a dataset annotated automatically using a proven algorithm. Additionally, surrogate waveforms can be used as a gold standard when a similar feature is located. As an example, it is possible to use the ECG R-R interval as a gold standard for locating the PPG foot or peak. This works under the assumption that the heart rate as measured on the ECG should be the same as that measured on the PPG.

To benchmark the location of interest it must be compared to the gold standard, resulting in one of three possibilities: a true positive (TP), a false negative (FN), or a false positive (FP). Feature locations identified within the acceptance interval of the gold standard are considered a true positive (TP). Locations that are not within the acceptance interval of the gold standard are false positives (FP). If a feature is not found within the acceptance interval of the gold standard, it is considered a missed beat, or a false negative (FN). Using this classification, the sensitivity and positive predictive value can be calculated.

The sensitivity (Se) is found using both the number of TPs and FNs, as shown in (4.2). Sensitivity represents the percentage of beats that are correctly identified.

$$Se = \frac{TP}{TP + FN} \tag{4.2}$$

The positive predictive value (PPV) is shown in (4.3) and represents the percentage of the beats found that are not false positives. In other words, it is the measure of the percentage of extra beats out of every beat that was located.

$$PPV = \frac{TP}{TP + FP} \tag{4.3}$$

The sensitivity shows how likely the algorithm is to miss a beat, while the PPV shows how likely the algorithm is to find an incorrect beat.

The acceptance interval used will vary depending on the feature being analyzed, the desired accuracy, and the signal that is used. The acceptance interval allows for a small (yet acceptable) variation in the resulting feature location. As an example, an acceptance interval of 100 ms can be used for the ECG R-peak since the QRS complex may be as large as 200 ms. A smaller acceptance interval of 19 ms can be used for the PPG in order to accept only the most accurately delineated beats.

For the sensitivity and positive predictive value, a larger acceptance interval produces better results. On the other hand, when calculating the average temporal accuracy of only true positive beats, a larger acceptance interval could produce worse results as beats with greater error are included. The larger the acceptance window (and associated allowable error), the larger the temporal error will be. Care must be taken when choosing the correct acceptance interval depending on which feature is being analyzed.

4.5 ECG Delineation

4.5.1 Algorithm

ECG R-peaks are delineated on a beat-by-beat basis using a modified version of the well-known Pan-Tompkins (PT) algorithm [102]. The raw ECG signal is processed in order to isolate the QRS complex both in the frequency domain and the temporal domain. A first order Butterworth bandpass filter with a bandwidth of 5-15 Hz is used on the input ECG waveform; the same filter that was used in the signal quality algorithm (Section 4.3). A five-point derivative of the filtered ECG is taken and the resulting waveform is then squared. The squared signal is low-pass filtered using a third order Butterworth filter with a -3 dB cutoff frequency of 8 Hz, such that the resulting waveform will have smooth, individual peaks for each QRS complex. The cutoff frequency of 8 Hz was chosen to match the duration of a prolonged QRS complex, which is 120 ms [35, 37]. Two thresholds are calculated from the resulting signal using a 5 second moving average, where the upper threshold is 1.25 times the moving average and the lower threshold is 0.3 times the moving average. Example waveforms from various stages of the modified algorithm are shown in Figure 4.4, including both thresholds.

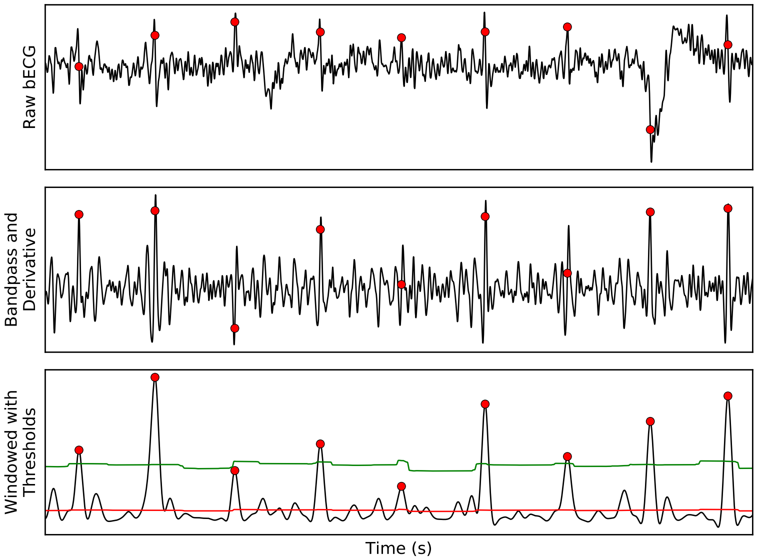

Figure 4.4: The modified PT algorithm processes the raw ECG signal in order to isolate QRS complexes for delineation. Dual thresholds are calculated using a moving window average and are continually updated, rather than just updated when an R-peak is found. The resultant R-peaks are often not exactly at the peak since the processing introduces shifts in the R-peak location, necessitating a refinement stage.

Each peak in the processed signal is located from largest to smallest amplitude with a minimum peak distance of 200 ms between peaks, corresponding to the cardiac refractory period [102]. Peaks that have an amplitude greater than the larger threshold are determined to be R-peaks. The median beat interval is calculated using all beats within 20 seconds of the current interval under test, in order to allow for natural variations in HR over time. If any of the resulting beat intervals are greater than 1.5 times the median beat interval, the lower threshold is used to locate any missing peaks.

This algorithm differs from the original PT algorithm in [102], which was designed for real-time functionality on an embedded system, by using alternate filtering approaches and by using a different mechanism for calculating the dual thresholds. A Butterworth filter with a bandwidth that better isolates the constituent frequencies of the QRS complex is used and a third order low-pass filter was used in place of moving window integration. The modified PT thresholds are continuously updated to incorporate magnitude information from the peak, baseline noise, motion artifacts, and other ECG features in order to dynamically adjust to extreme changes in signal quality typical of dry electrodes.

While locating the exact peak of the R-wave is not critical when calculating HR and HRV, exact accuracy is needed when ensemble averaging in order to avoid feature smearing. Both the PT and the modified PT algorithm do not always locate the exact peak of the R-wave since the exact location is smoothed out by the processing stages, as shown in Figure 4.4. The R-peak location is refined by locating the two largest peaks in the squared derivative of the filtered ECG signal, within 150 ms of the original R-peak location. These two peaks bound the search window for the R-peak, which is defined as the first zero crossing of the first derivative of the filtered ECG signal.

Once the ensemble averaged beat is generated (see Section 4.8), the Q-wave onset, S-wave end, and T-wave end become clearly visible on the bECG, allowing a custom algorithm to accurately locate each feature. The Q-wave onset is defined as the return to baseline before the Q-wave peak, if visible. The algorithm locates this feature by finding the closest maximum or minimum of the second derivative (zero-crossing of the third derivative) to the left of the Q-wave peak. A high-pass filter with a cutoff frequency of 5 Hz is used before locating the Q-wave peak, which ensures that a Q-wave-like feature becomes visible even if one is not present in the raw ECG signal. Similarly, the S-wave end is defined as the return to baseline after the S-wave peak on the high-pass filtered ECG. The algorithm locates the inflection point of the second derivative (zero-crossing of the fourth derivative) after the S-wave peak, as the T-wave can obscure the local extrema of the second derivative. The QRS duration is calculated as the time between the Q-wave onset and S-wave end.

For the purposes of this work, the T-wave is located by finding the zero crossing of the second derivative (first derivative extrema) after the minimum of the second derivative. This results in the T-wave end being defined as the return to baseline after the maximum point of the downslope (or upslope, as this method is independent of polarity) of the T-wave. The corresponding QT interval is defined as the interval between the Q-wave onset and the T-wave end.

These algorithms have not been designed to robustly extract features for non-standard morphologies, such as those present during disease state. For example, the heart failure population has a prolonged QRS duration that changes the frequency content of the QRS complex. The QRS complex also may not have a well-defined peak or S-wave end, requiring the use of proprietary software or manual expert annotations. Creating a mean beat delineation that is robust to different morphologies is out of the scope of this work and may be investigated in the future.

4.5.2 Validation on Standard Databases

Methods

The modified PT algorithm with signal quality based classification is verified using the annotated MIT-BIH Arrhythmia Database (MITDB) and European ST-T Database (EDB) as a gold-standard [103, 104]. The MITDB contains 48 records that are each 30 minutes in duration and the EDB contains 90 records that are each 120 minutes in duration, provided by PhysioNet [105]. The signals from the MITDB and EDB have not been resampled, as the modified PT algorithm does not require the ECG to be a specific sample rate. The bxb function in the WFDB application [105] was used to determine the sensitivity and PPV of the algorithm compared to the gold-standard annotations using a standard acceptance window (e.g. match window) of 150 ms. The signal quality algorithm described in Section 4.3 is used to indicate periods of shutdown, where the classification results are tallied separately. The beats that would be missed during the shutdown period are not included when calculating the number of false negatives, which are described in Chapter 4.

Results and discussion

The algorithms presented herein have been tested on the MITDB and the EDB to ensure that there is no bias introduced by the delineation algorithms when comparing the bECG to the Lead II ECG. Both the MITDB and EDB are standard databases that contain hand annotated gold-standard references and are commonly used to verify beat delineation algorithms. The sensitivity, PPV, and accepted signal quality percentages for the MITDB and EDB are shown in Table 4.1.

Database	Total Beats	Se	PPV	SQI Pass
MITDB	107504	99.58%	99.95%	98.07%
EDB	760603	99.87%	99.80%	96.55%
Cumulative	868107	99.83%	99.82%	96.73%

Table 4.1: QRS Classification on Standard Databases

The algorithms presented herein have a cumulative (total) sensitivity of 99.83% and PPV of 99.82% across both databases, which is comparable to best-in-class algorithms that typically have a sensitivity and PPV over 99.5%, with very few over 99.8% [106]. Further improvements on standard databases may be possible if the algorithms were tuned for waveforms collected with traditional wet electrodes. Three of the most successful ECG delineation algorithms utilize the wavelet transform [107, 108, 109]. These algorithms have achieved an error rate of less than 0.34%. A detailed comparison of state-of-the-art algorithms is shown in Table 4.2. The success of these algorithms can be attributed to both the basis function used during pre-processing and adaptive thresholding techniques.

	MITDB		EDB	
Algorithm	**Sensitivity**	**PPV**	**Sensitivity**	**PPV**
Present work	99.57%	99.95%	99.87%	99.80%
Saadi et al. [110]	99.90%	99.87%	99.84%	99.71%
Martinez et al. [111]	99.71%	99.97%	99.73%	99.67%
Martinez et al. [107]	99.80%	99.86%	99.61%	99.48%
Di Marco et al. [112]	99.77%	99.86%	99.81%	99.56%
Li et al. [113]	99.89%	99.94%	N/A	N/A
Pan et al. [114]	99.75%	99.54%	N/A	N/A
Bahoura et al. [108]	99.83%	99.88%	N/A	N/A

Table 4.2: Delineation Algorithm Comparison

The present delineation algorithm parameters have not been tuned for use with these databases since they were designed for use with the bECG. Performance on these databases is expected to improve if the algorithms were tuned for wet electrode use. This modified Pan Tompkins algorithm has best-in-class sensitivity and PPV for the EDB, which has many more annotations and variety than the MITDB. These results demonstrate the accuracy and utility of the approaches described herein.

4.6 PPG Delineation

4.6.1 Introduction

A novel and easily implemented delineation algorithm is presented, which allows the foot of the photoplethsymogram to be located with sufficient accuracy for heart rate variability applications. This algorithm combines classical delineation techniques with the robustness of the wavelet transform. It can be implemented with a set of FIR filters and simple non-adaptive thresholding, making it suitable for real-time ambulatory applications. Results show that the accuracy of the algorithm matches that of a standard electrocardiogram delineation algorithm, the current standard for heart rate variability applications. The algorithm presented herein is also compared against four state-of-the-art delineation algorithms. Using a database that contains exercise data from thirteen patients across six activity levels and 7012 beats, a temporal accuracy of 3.8±2.6 ms (mean±std) was achieved with a sensitivity of 99.29% and a positive predictive value of 99.23%.

The wavelet transform (WT) is powerful and simple to implement since it is a cascaded set of FIR filters [107]. The WT has been used in ECG delineation [107, 109] and to reduce motion artifacts in both the PPG and ECG [115, 116]. This work extends upon previous research by using a specific wavelet scale to locate each PPG beat (beat segmentation) before delineation. The performance of the wavelet transfer derivative delineation (WTDD) technique is compared with the performance of four state-of-the-art delineation algorithms: one PPG delineation algorithm [117] and three arterial blood pressure (ABP) delineation algorithms [118, 119, 120]. Comparing PPG delineation algorithms to ABP based algorithms is appropriate since they both have the same temporal features and very similar beat morphology [120].

In [117], [119], and [120], a manually annotated database was used to verify the delineation algorithm, while in [118], a synchronized ECG was used. To avoid human error and inconsistent results, the QRS complex in a synchronized ECG was used as a reference for determining the accuracy of the proposed PPG delineator, rather than a manually annotated database.

The temporal accuracy, sensitivity, and the positive predictive value (PPV) were used to quantitatively compare each algorithm's performance. All of these metrics are influenced by the acceptance interval, which is used for determining if delineated beats are valid. A large acceptance interval will result in an improved sensitivity and PPV. The acceptance interval has the opposite effect on the temporal accuracy. It allows less accurate beats to be included when calculating the temporal accuracy, thereby degrading this metric. For this reason, a large acceptance interval of 19 ms is used in this work. To demonstrate the robustness of the WTDD algorithm, exercise data was used that contains motion artifacts, baseline wander, and a variety of heart rates across a range of patients.

4.6.2 Algorithm

A single photoplethysmogram (PPG) beat contains three distinct features: the foot, the peak, and the dicrotic notch as shown in Figure 4.5. The foot was selected for delineation due to its steep up-slope and high correlation to ECG timing [118].

The wavelet transform derivative delineation (WTDD) algorithm consists of two phases, as shown in the block diagram in Figure 4.6. The first phase locates the valid range for each beat, also known as beat segmentation. The valid range for the PPG foot is found using the wavelet transform in combination with a simple moving average window filter. Once the

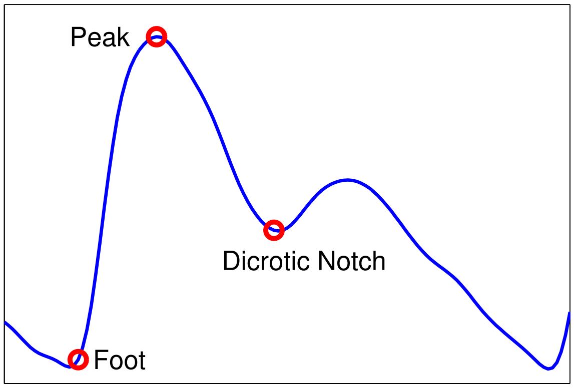

Figure 4.5: An example PPG beat shows the locations of the foot, the peak, and the dicrotic notch.

valid range is determined, the wavelet transform (WT) is no longer used. In phase two, the valid range and a filtered version of the original waveform is used to determine PPG foot location.

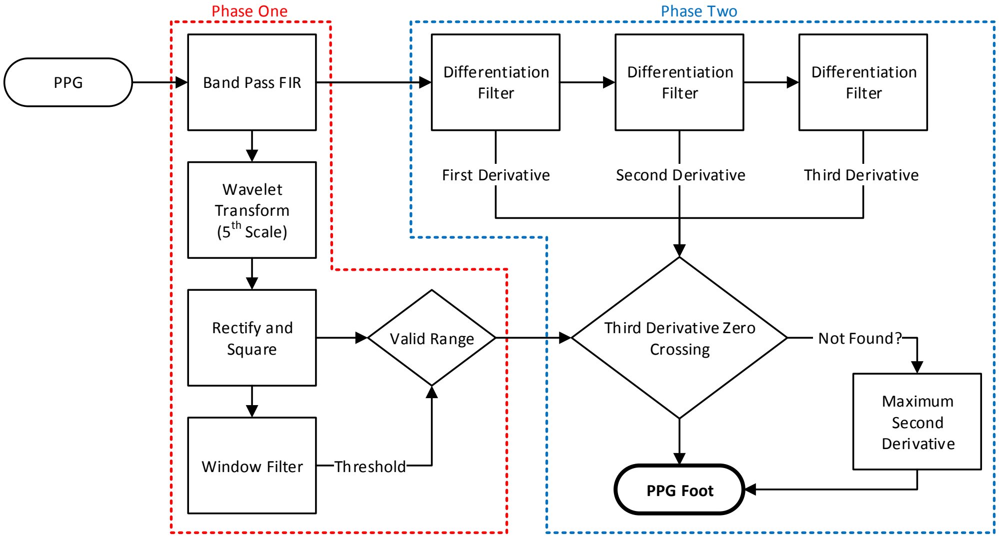

Figure 4.6: Block diagram of the wavelet based PPG delineation algorithm. The wavelet transform is used with a simple moving average threshold to locate the valid range in phase one. The foot location is found using the first three derivatives of the original PPG signal in phase two.

Phase One

The wavelet used for beat segmentation is the quadratic spline wavelet, where the prototype wavelet is the derivative of a smoothing function (Gaussian). Each wavelet scale represents the derivative of a different range of frequencies contained in the original signal [107]. In this work, the fifth wavelet scale was chosen since it contains the characteristic frequencies of the PPG foot.

The wavelet transform (WT) can be implemented using an FIR filter bank; the filters used herein are those shown in [121]. This filtering is typically done by down-sampling the signal after each stage. Rather than down-sampling the entire signal, the method utilized herein up-samples the FIR filter taps [107]. Not only does this reduce the complexity of implementation, but it allows temporal features to remain synchronized throughout each wavelet scale.

By rectifying and squaring the fifth wavelet scale (referred to as the processed wavelet), distinct peaks appear at the start of each beat; this process is shown in Figure 4.7. The processed wavelet is used to generate the threshold, which determines the valid range for the PPG foot. This threshold is non-adaptive – it is created by using a moving hamming window of 5 seconds, which functions as a low-pass FIR filter. The valid range (search window) for the PPG foot is defined as the range where the processed wavelet signal is above the threshold.

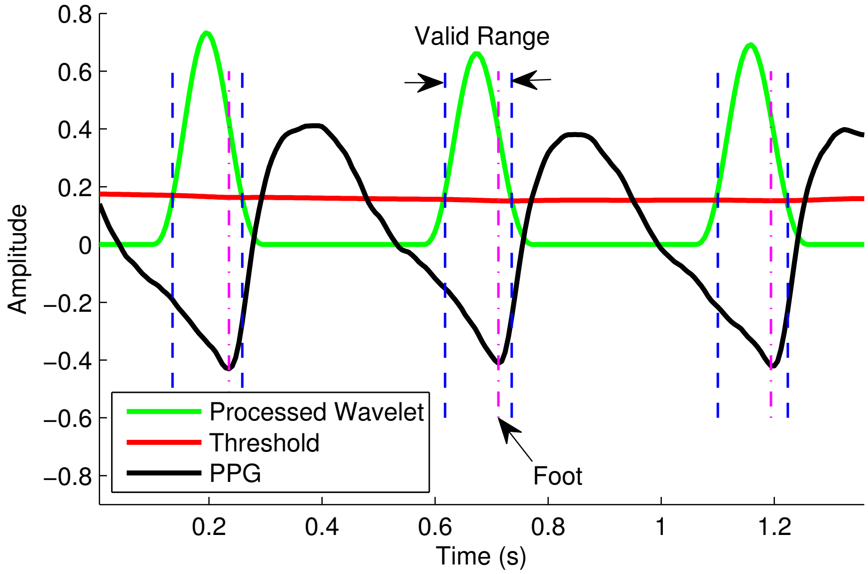

Figure 4.7: Each beat is located using a squared and rectified wavelet transform (Processed Wavelet). The valid range is found by locating the points where the threshold crosses over the processed wavelet. Foot locations are then identified within the valid range.

Phase Two

The PPG is filtered using a bandpass filter with a bandwidth of 0.5-5 Hz. The first, second, and third derivatives of the PPG are found using a 51-tap FIR differentiation filter. The location of the PPG foot is defined as the local maximum of the second derivative within the valid range, representing the signals maximum upward acceleration. Algorithmically, this is found by searching for the first zero-crossing of the third derivative within the valid range such that both the first and second derivative are positive. If such a zero-crossing is not found within the valid range, the maximum value of the second derivative is used as the location of the PPG foot.

The physiological data set used to validate this algorithm was obtained under informed consent in a protocol approved by the Rochester Institute of Technology, Institutional Review Board for Protection of Human Subjects. The Biopac MP36 (Biopack Systems, Inc., Goleta, CA) was used to capture synchronized ECG and ear PPG from thirteen test subjects at a sample rate of 50 kHz. In order to more closely match the Nyquist sampling rate found in typical PPG measurement systems, both measurements were decimated to a sample rate of 160 Hz.

A recumbent bike was used to vary the activity level of the test subject in order to test how well the WTDD algorithm performs across a range of physiological states. One minute measurements were captured at six different physiological states for each subject. These physiological states include the subject at rest while sitting, while standing, and while supine; in addition to three levels of increasing activity, each with an higher heart rate.

The R-peaks in each QRS complex were found using the method published by Pan and Tompkins in [114]. The PPG foot and the R-peak are synchronized by shifting the ECG forward, by the median offset for each beat in the measurement [118]. After synchronization, the temporal accuracy is defined as the absolute value of the difference between the R-peak and the PPG foot, for correctly identified beats.

The foot location was compared to each R-peak, resulting in one of three possibilities: a true positive (TP), a false negative (FN), and a false positive (FP). When foot locations are identified within the acceptance interval of the R-peak, it is considered a true positive (TP). Foot locations that are not within the acceptance interval of a R-peak, are false positives (FP). If a foot is not found within the acceptance interval of the R-peak it is a missed beat, or a false negative (FN). The acceptance interval used in this paper is 19 ms, which corresponds to three sample periods.

4.6.3 Delineation Verification

The sensitivity, PPV, and temporal accuracy of the algorithms presented in [117, 118, 119, 120] are compared to the WTDD algorithm in Table 4.3. These results show that the algorithm presented herein has a sensitivity and PPV equivalent to previously published algorithms, while having significantly better temporal accuracy.

Algorithm	**Signal**	**Beats**	**Sensitivity**	**PPV**	**Interval**	**Time**
WTDD	PPG	7012	99.29%	99.23%	19 ms	3.8±2.6 ms
[117]	PPG	2900	96.89%	94.55%	12 ms	N/A
[118]	ABP	39848	99.31%	99.74%	20 ms	5.18±12.81 ms
[119]	ABP	42569	99.36%	98.43%	16 ms	N/A
[120]	ABP	2564	99.96%	98.73%	8 ms	4.87±12.94 ms

Table 4.3: PPG Delineation Results

When compared to [117], this algorithm performs significantly better for both the sensitivity and the PPV, while the temporal accuracy was not reported. This method uses a similar pre-processing approach, where it rectifies the average of the PPG derivative. It then uses adaptive thresholding to recognize each beat. This algorithm, while fairly simple to implement, does not perform as well as the algorithm presented herein. This is most likely caused by incorrect beat segmentation, which is addressed by the use of the WT herein.

The algorithm proposed in [118], which locates the arterial blood pressure (ABP) waveform peak, is often used as the standard to which other delineation algorithms are compared. This algorithm uses a slope sum function, adaptive thresholding, and a local search strategy for locating each beat. The decision rule for locating each beat is a complex process, which results in a stellar sensitivity and PPV. While the temporal accuracy was not directly presented in [118], an estimate was calculated using a histogram reported in [118] by calculating the standard deviation by locating the range where 95% of the results were included. Despite a large acceptance interval and the use of a localized search strategy for locating each peak, the temporal accuracy of [118] was inconsistent, resulting in a large standard deviation which will negatively impact heart rate variability applications.

In [119], the proposed algorithm locates the ABP waveform peak. This algorithm first estimates the heart rate using a band pass filter; the heart rate is then used to adaptively calculate the cutoff frequencies for the filtering stage. This algorithm is highly complex and may cause implementation issues in resource constrained systems, such as those used in real-time, ambulatory heart rate variability applications. Peak detection is completed using rank-order (percentile-based), non-linear filters, and a nearest neighbor algorithm. Rather than using manual annotations to test the validity of their approach, they use QRS detection – the same approach taken herein. The temporal accuracy was not included in [119].

The algorithm presented in [120] is a complete ABP waveform delineator. It locates the foot, the peak, and the dicrotic notch of the ABP waveform. This algorithm uses derivative calculation, zero-crossing detection, and adaptive thresholding to segment each beat. Two datasets were presented in this paper. Only one data set was used when calculating the time error of the foot detection, thus the results for only this dataset are presented in Table 4.3. The sensitivity of [120] is remarkably high, especially considering a very small acceptance interval was used. While the sensitivity of the WTDD algorithm is not as high as in [120], the temporal accuracy of [120] has significant variation, which can negatively impact heart variability applications. The temporal accuracy is especially poor considering such a small acceptance interval was used. The spread of the temporal error (the standard deviation) will result in incorrect HRV metrics, since it is the standard deviation in heart rate that directly causes heart rate variability. The goal for these algorithms is to minimize the standard deviation due to algorithmic error so that only physiological variation remains.

Rather than using an adaptive technique for beat recognition, the algorithm presented herein utilizes the WT for its simplicity. Using the WT does not sacrifice accuracy; on the contrary, it provides an incredible resilience to noise. The example shown in Figure 4.8 demonstrates how the PPG can be accurately delineated, despite significantly different beat to beat morphologies. This includes baseline wander and significant changes in amplitude, which is most likely caused from motion artifacts.

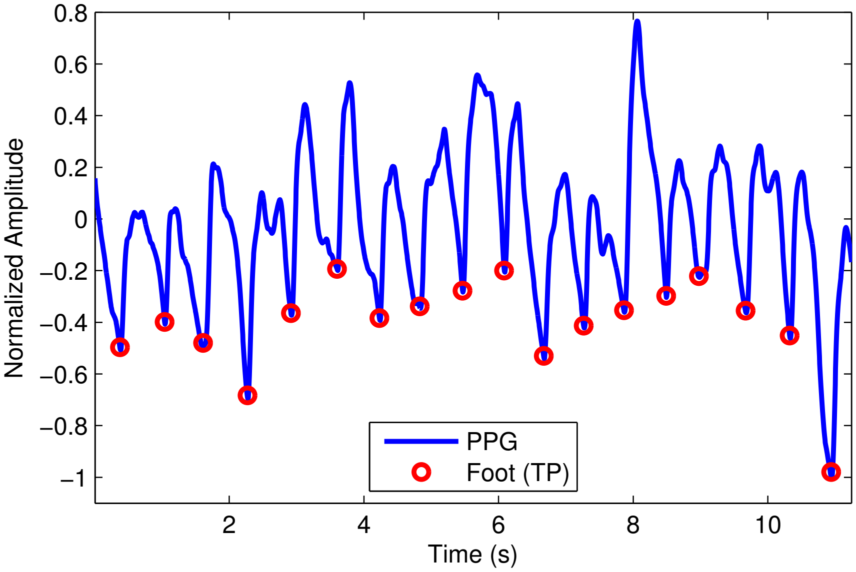

Figure 4.8: An example showing the correct delineation of non-ideal PPG signal with significantly different beat to beat morphology. True positives for the WTDD algorithm are marked in red.

While the WT allows for highly accurate beat segmentation, using the WT alone would not result in a high enough temporal accuracy for HRV applications. It is for this reason that a two phase approach was used for locating each foot. A high level of reliability results from the use of the WT, while the high level of accuracy is achieved by using the derivatives of the original signal for foot detection.

This algorithm can be applied to non-contact photoplethysmography methods – enabling new types of devices and applications. An example of such an application is when the heart rate is extracted from a video of the face [122, 123] or from a smart phone [124]. By simply adding a video camera to everyday devices, this algorithm can allow heart rate variability to be used for determining stress levels and monitoring the level of focused attention in situations where the use of a PPG or ECG is inappropriate. Examples include use in an automobile or when monitoring an infant. The PPG delineation algorithm presented herein is highly successful for accurately delineating the PPG foot. This approach has wide applicability, not only for the PPG foot, but other PPG features and waveforms. Future work should investigate the extension of this algorithm to detection of other PPG features, such as the dicrotic notch and peak.

The WTDD algorithm can enable the proliferation of the PPG for use in ambulatory heart rate variability applications. The combination of the wavelet transform and standard derivative based methods, result in an algorithm that is as sensitive and reliable as the best existing algorithms, while significantly improving upon the temporal accuracy. Such an algorithm can be implemented on a standard low-power microcontroller, rather than a more specialized device such as a DPS or FPGA. The ease of implementation of this algorithm makes it well suited for portable, low complexity, cost efficient medical devices.

4.7 BCG Mean Beat Delineation

The BCG is not delineated on a beat-by-beat basis, as motion obscures the signal in almost all cases. As such, ensemble averaging (see Section 4.8) is required in order to locate each feature within the BCG. The first step in delineating any signal, is finding the most prominent feature and using it as a reference for all subsequently located features. For the ECG, this signal is the R-wave peak and for the PPG, this signal is the foot. While the IJK complex is typically the most prominent in the BCG, this is not always the case. A BCG beat often contains a notched J-wave or a J-wave with low absolute amplitude. While there are many different BCG features, the peak of the BCG's first derivative was empirically determined to be the most consistent feature.

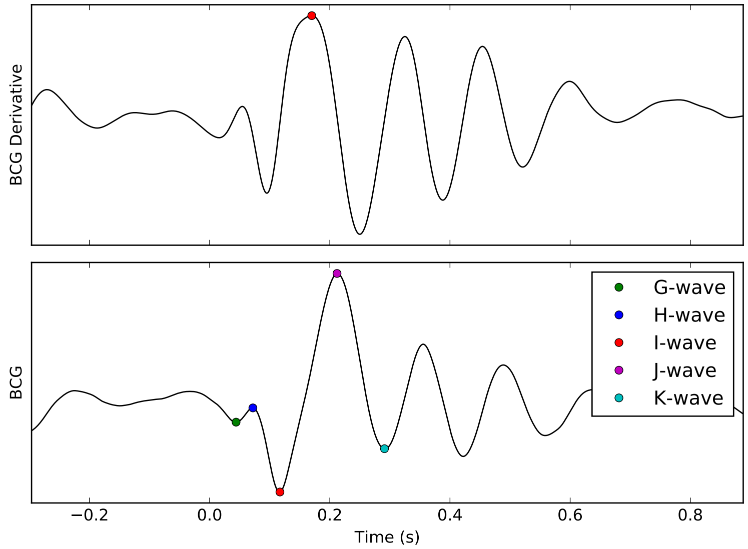

Figure 4.9: The ensemble average BCG beat is delineated by first locating the peak of the derivative and then subsequently locating each of the major BCG waves relative to the derivative peak. The G, H, I, J, and K-wave delineations are shown relative to the BCG derivative peak.

This feature is always located within 100 ms to 300 ms of the R-peak for normative subjects. More importantly, it is the only large positive peak within this range. This single beat BCG delineation algorithm locates this feature by finding the maximum of the filtered derivative of the BCG (0.5-15 Hz bandwidth) within this range. The resulting point is always between the I-wave and the J-wave.

The I-wave and J-wave are located by looking for the next zero crossing to the left and right of the derivative peak, respectively. The unfiltered derivative is used when locating these zeros in order to maintain the original temporal resolution of the signal. This is shown in Figure 4.9, where the BCG and the filtered derivative is shown with each delineated feature marked. The remaining waves (G, H, and K waves) are found by looking for the matching zero crossing in the unfiltered BCG derivative.

4.8 Ensemble Averaging

Ensemble averaging is a technique used in cardiovascular signal processing to reduce noise and improve feature prominence for a single averaged beat. For example, features such as the T-wave may not be visible on a beat-by-beat basis, however ensemble averaging allows these features to become clear and easily located. This work uses the standard ensemble averaging technique, where each beat is stacked relative to a consistent feature, such as the R-peak, and then averaged sample-by-sample as shown in Figure 4.10. Only sections of the signal that pass the signal quality index algorithm are included when generating the ensemble average.

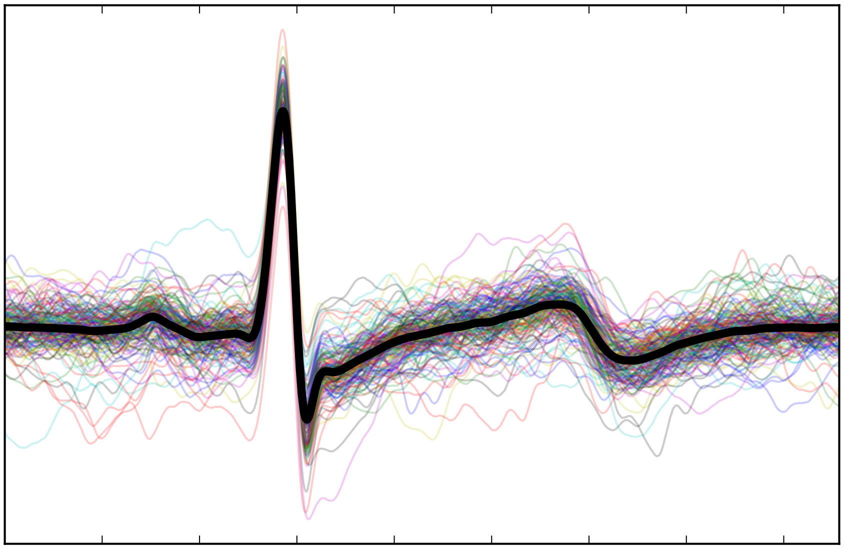

Figure 4.10: Ensemble averaging aligns multiple beats based on a common feature such as the R-wave peak in order to calculate an average beat. This allows small features to become prominent, despite not being clearly defined on a beat-to-beat basis. This example utilizes bECG from a normative subject.

4.9 Conclusion

The present algorithms enable the data acquired during use of the FIT seat to be accurately analyzed. The FIT seat measurement modalities create many challenges that have been overcome using these custom algorithms, such as the increased noise in dry-electrode ECG systems. While these algorithms were designed specifically for the FIT seat, they can be utilized on any system that contains noisy waveforms. Specifically, the signal quality algorithms presented herein provide a unique approach to rejecting data that should not be analyzed. This is integral to the success of the FIT seat.

Chapter 5

Human Subject Testing and Gold-Standards

5.1 Introduction

The human subject studies described herein were performed under informed consent using a protocol approved by the institute review boards at the Rochester Institute of Technology and the University of Rochester Medical Center. Human subject testing has been performed in two phases. The first phase verifies the FIT seat functionality on normative subjects, and the second phase verifies its ability to accurately acquire signals and extract parameters from the heart failure population. These studies have been designed specifically to validated the bECG waveform and to provide additional insights into the mechanisms behind the BCG waveform.

5.2 Normative Study – Phase I

In this phase, FIT sensors have been hard-wired to a biomedical data acquisition system (Biopac and LabView DAQ system) enabling time synchronized collection of FIT data with clinical measures (12-lead ECG, respiration, SpO_2, echocardiogram, aortic pulse wave velocity). Baseline feature extraction algorithms have been developed for the bECG, bPPG, and bBCG. The goal of Phase I is to determine if the FIT Seat can measure cardiology variables as accurately as current generation commercial medical equipment. Normal subjects (healthy college students and faculty) have been tested at rest and after mild exercise. The goal of post exercise testing is to determine the ability of the FIT seat to measure changes in the cardiology variables across physiological states.

Differences in individual variables and waveforms have been assessed using correlation, classification metrics, and the Student's T-test with paired observations. HR calculated from the ECG are compared to the same variables measured by FIT Seat bECG, bPPG and BCG. A difference of $p \leq 0.05$ are considered statistically significant when using the T-test.

Normative testing was performed on 26 healthy subjects with no history of heart disease. The data used herein was obtained under informed consent in a protocol approved by the Rochester Institute of Technology Institutional Review Board for Protection of Human Subjects. The laboratory used for subject testing was transformed into a hospital-like setting, as seen in Figure 5.1. The instrumentation in a Biopac MP150 system was used to amplify and filter a 12-lead ECG, bECG, two ear PPG, SpO_2, respiration strap, and a thigh cuff (when needed). Custom instrumentation was used for the bPPG, IR temperature sensor, and four BCG channels. A National Instrumentsc RIO-9075 CompactRIO DAQ system was used to digitize the signals from both the Biopac instrumentation and the FIT seat.

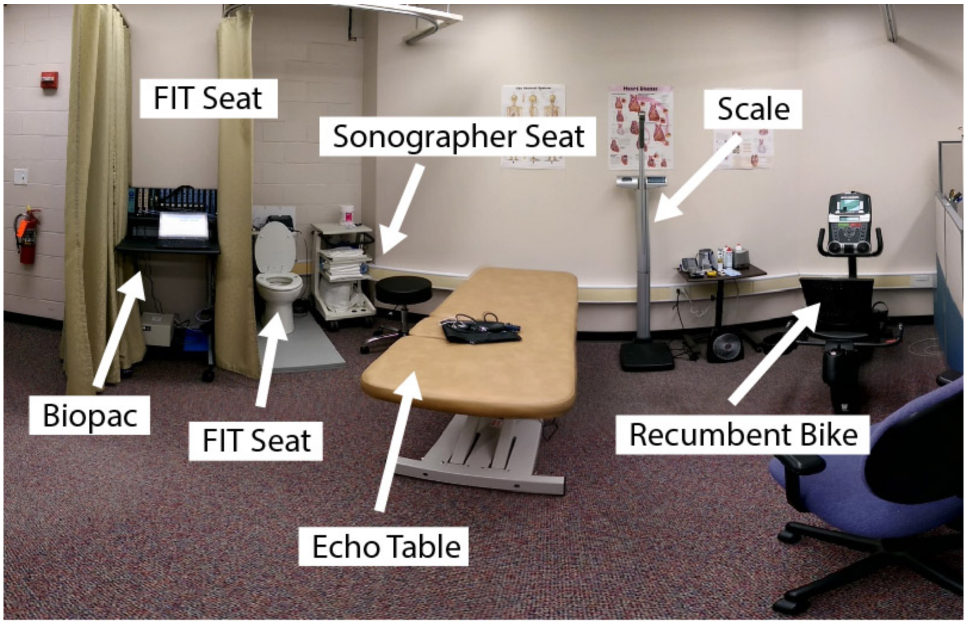

Figure 5.1: Two layers of privacy curtains were added to the lab for normative subject testing. The subject sits behind the second layer of curtain on the toilet seat while the data is acquired on a laptop and the sonographer takes picture on the echocardiogram.

Before the procedures were started, the subject's relevant medical history was taken as well as their height and weight with a Health o meter Professional 500KL Eye Level Digital Medical Scale. Additional measurements were taken so that the length of their aorta can be estimated. Finally, an initial echo of the subject was taken to ensure that there were no cardiac conditions that would prohibit them from performing the tasks defined in the following procedures. The testing consisted of five protocols:

1. Resting FIT measurements
2. Resting FIT + sitting echo
3. Resting supine echo
4. Post stress supine echo
5. Post stress FIT + sitting echo

In the first protocol, six 150 second (2.5 minute) long recordings were created with the subject on the FIT seat. Between each recording, the subject was instructed to stand up. When they were seated again, they took a BP measurement from a wrist cuff (Omron BP652N 7 Series), and then the next recording was started.

For recordings 1-4, the subject was instructed to sit up straight and attempt to remain still. For recordings 5-6, the subject was instructed to lean forward between 45-60 degrees. In recordings 1-2, they were instructed to hold their breath for 15 seconds, 2 minutes into the recording. For the last four recordings, the subject was instructed to hold their breath for 15 seconds, 2 minutes into the recording, and to perform a Valsalva maneuver for 5 seconds, 1 minute and 45 seconds into the recording.

The second protocol consisted of the subject sitting on the FIT seat while the sonographer took simultaneous echo captures. Every time a capture was taken, a 10 second retrospective clip was generated in the NI DAQ system. There is a total of 23 clips in this phase. For the first 16 clips, the subject was asked to sit upright. For the remaining 7 clips the subject was asked to lean forward. Five of the clips consisted of a pulse wave Doppler, where the subject's blood pressure was taken with a wrist cuff. Additionally, the thigh cuff waveform was captured for these clips.

The third and fourth protocol consisted of the subject lying supine on an echo table while the sonographer took a total of 21 and 16 echo captures respectively, at least two times each. After the third protocol, the subject was asked to raise their HR to 75% of their maximum heart rate on a recumbent bicycle. This step was repeated after the fourth protocol was completed. The last protocol is very similar to the resting FIT + sitting echo (protocol 2). Rather than taking 23 clips, only 16 clips were taken when the subject was sitting upright. Four of the clips consisted of a pulse wave Doppler, which included the subject's blood pressure (taken on the wrist) and the thigh cuff waveform.

For all echocardiograph measures, Lead I was connected to the GE Vivid i ultrasound system for time synchronization of all measures with the echo images. The protocols involving combined FIT + echo measures enable synchronization of cardiac event timing relative to ECG and all FIT seat parameters.

5.3 In-Hospital Study – Phase II

Heart Failure subject testing has been completed 25 subjects in a single-center observational study of patients admitted for heart failure. Patients were recruited shortly before discharge to have FIT testing combined with traditional transthoracic echocardiographic (GE Vivid i) and electrocardiographic measurements of cardiac function. A commercially available Biopac MP150 instrumentation system was used to amplify and filter a 12-lead ECG, two ear PPG, SpO_2, respiration strap, and a thigh cuff plethysmogram. Custom instrumentation integrated into the FIT seat was used to capture the bECG, two bPPG channels, IR temperature, four weight channels and four BCG channels. A National Instruments cRIO-9075 CompactRIO DAQ system was used to digitize the signals from both the Biopac instrumentation and a trigger based sync signal generated by the FIT seat, which allows for time synchronized capture of all waveforms. The ECG was also captured by the ultrasound system with manual clip capture synchronization enabling alignment of the ultrasound measures with the NI DAQ system captures.

Before the procedures were started, the subject's relevant medical history was taken. The latest height and weight measurement from the subject's chart was noted. Physical measurements of bony landmarks relative to the seat were taken to enable estimation of aorta length (when combined with ultrasound measures as defined below). The testing consisted of three protocols: resting FIT measurements, resting FIT + sitting echo, and resting supine echo. Exercise was not performed due to the physical limitations of heart failure subjects.

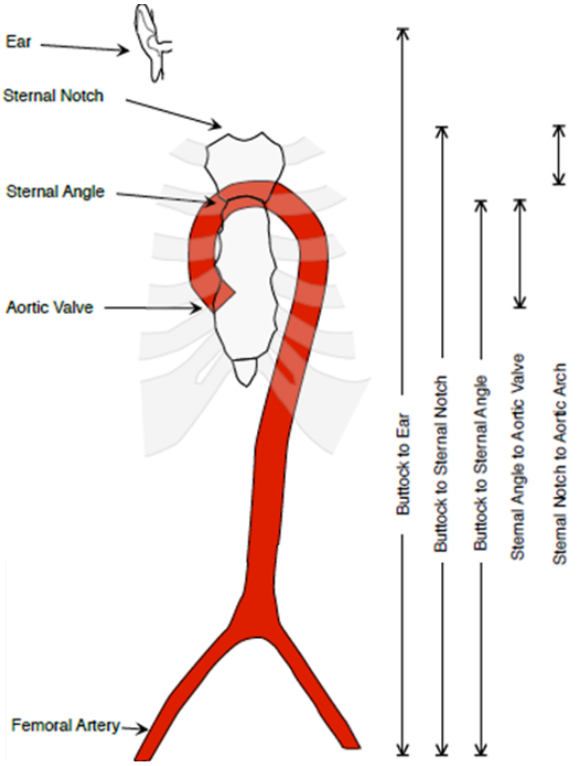

Figure 5.2: The aortic length of a subject can be estimated from a combination of superficial measurements and ultrasound based measurements. This method for estimating the total aortic length incorporates the aortic arch, making it robust and accurate compared to empircal based estimations that utilize only superficial measurements. Image courtesy of Karl Q. Schwarz, MD.

The length of the artery from the aortic valve to a selected end point along the artery (AL) can be determined based on direct subject measurement (external). Measurements are done on an individual in a seated position. The distance between the sternal notch (SN) and the sternal angle (SA) is measured, either directly or by reference to the seating platform top (B). The distance between sternal angle (SA) and aortic valve (AV) is measured, e.g., via ultrasound imaging. The distance between sternal notch and aortic arch (AA) is measured, e.g., via ultrasound imaging. The 5 measurements that are made are as follows. These measurements are shown in Figure 5.2.

1. Buttocks to Sternal Notch ($\mathrm{B_{SN}}$).
2. Buttocks to Sternal Angle ($\mathrm{B_{SA}}$).
3. Sternal Angle to Aortic Valve ($\mathrm{SA_{AV}}$).
4. Sternal Notch to Aortic Arch ($\mathrm{SN_{AA}}$).

The first three measurements are made with a tape measure while the subject is sitting on the FIT and the last two are made with 2D ultrasound imaging, either to identify the intercostal space with the aortic valve (item 4) or by imaging from the sternal angle towards the aortic arch (item 5). The sternal angle and notch are bony protuberances that are easily palpated and used by surgeons and other providers to locate anatomical structures. Above the sternal angle is an ultrasound window to view the aortic arch (and measure distance). The sternal notch is used to identify the second intercostal space. As noted above, ultrasound is used to find the intercostal space most aligned with the aortic valve and the space number is calculated based on the sternal notch.

The pulse wave distances are calculated using the following:

$$AV_{Buttocks} = (B_{SN} - SN_{AA}) + (SA_{AV} + (B_{SN} - B_{SA}) - SN_{AA}) \tag{5.1}$$

In the first protocol, six 150 second (2.5 minute) long recordings were captured with the subject on the FIT seat. A single recording session consisted of a traditional cuff-based blood pressure (GE Carescape v100) measurement for systolic and diastolic pressure, followed by FIT measures. Between each recording, the subject was instructed to stand up to introduce positioning differences and associated impact on signal quality / characteristics when the subject was able. Directly before the next recording was started, the blood pressure measure was repeated.

For recordings 1-2 the subject was instructed to sit up straight and attempt to remain still. The recordings consisted of normal respiration with a 15 sec of breath hold. The start time of the breath hold was manually captured. For recordings 3-4 the subject was instructed to sit upright. The recordings consisted of normal respiration with a 15 sec breath hold, followed by a 5 second Valsalva maneuver. The start times for breath hold and Valsalva maneuver were manually captured. For recordings 5-6, the subject was instructed to lean forward between 45-60 degrees and the sequence of measures outlined for recordings 3-4 were repeated (including Valsalva).

The second protocol consisted of the subject sitting on the FIT seat while the sonographer took simultaneous echo captures. For each capture that was taken, a marker was saved in the recording noting the time of capture. There are a total of 23 clips in this phase. For the first 16 clips, the subject was asked to sit upright. For the remaining 7 clips the subject was asked to lean forward at 45-60 degrees as in Procedure 1. Five of the clips consisted of a pulse wave Doppler, where the subject's blood pressure was taken with a wrist cuff. Additionally, the thigh cuff waveform was captured for these clips to be used for PWV determination (ultrasound aortic valve opening to thigh cuff pulse wave arrival used in combination with aorta length).

The third protocol consisted of the subject lying supine on an echo table while the sonographer took a total of 21 echo captures, at least two times each. This provided comprehensive, high quality echo measurements including left ventricular volume, systolic volume, cardiac output and cardiac index. For all echocardiograph measures, Lead II was connected to the

GE Vivid i ultrasound system for time synchronization of all measures with the echo images.

Chapter 6

The Buttocks ECG (bECG)

6.1 Introduction

Tracking changes in the electrocardiogram (ECG) from subjects on a daily basis can be critical in diagnosing and managing cardiovascular disease such as heart failure and hypertension. A toilet seat is the ideal device for monitoring a subject's ECG in their home since it is used consistently and requires no change in habit. This work presented in this chapter demonstrates the ability to accurately capture clinically relevant ECG metrics across subjects and physiological states using a toilet seat based buttocks ECG (bECG), enabled by advanced custom algorithms designed for noisy ECG signals. When validated on standard databases, the custom QRS delineation algorithm presented herein has an overall sensitivity and positive predictive value (PPV) of over 99.8% on the MITDB and EDB. A study across 25 subjects at both rest and post-stress shows that 81.3% of the bECG captured from a toilet seat is of sufficient quality for analysis, with lead II showing the highest morphological correlation to the bECG. The bECG has a QRS sensitivity and PPV of over 98.4% compared to Lead II with a HR accuracy within 0.05±0.87 bpm and a HRV accuracy of -3.50±8.96 ms. The QRS duration and QT_c interval have an accuracy of -0.40±7.43 ms and -9.36±18.91 ms, respectively.

6.2 Toilet Seat bECG for In-Home Monitoring

By integrating an ECG into a toilet seat, many of the challenges associated with in-home monitoring are addressed. The resulting cardiovascular monitoring system can be integrated into the natural routine of a subject, enabling measurements to be taken at the same time of the day before any stimulants (e.g. sugar, caffeine, nicotine, etc.) or food. This results in a daily stable measurement over time that is critical for accurate trend analysis. Issues with preparation and subject error are greatly reduced, since skin contact is automatic and has sufficient pressure to create a consistent electrode interface at a consistent location for each individual.

There are examples in literature demonstrating that it is possible to capture an ECG from a toilet seat [73, 74, 75, 76, 77, 78]. Only the work presented in [76] has quantitatively compared the seated ECG on a toilet seat to a gold-standard ECG measure, where both non-contact and wet electrodes placed on the thigh were compared to a standard limb lead ECG. Their results showed that manual R-peak delineation resulted in less than a 2 ms error in location and that the estimated HR was within 0.003 bpm for a single test subject. To date, there has not been a quantitative comparison between the bECG HRV, QRS duration, QT_c interval, waveform morphology to a clinical 12-lead ECG.

The work presented herein assesses the bECG's diagnostic capabilities compared to the 12-lead ECG in a controlled study, by quantitatively comparing the accuracy of extracted R-peaks, HR, HRV, waveform morphology, QRS duration, and QT_c interval. Simultaneous bECG and ECG recordings are captured from 25 subjects both at rest and post-stress. The purpose of this study is to demonstrate the feasibility of this system for accurately monitoring key parameters in a healthy population, as a precursor to studying the HF population and long-term trend based studies.

6.3 Choosing a Gold-Standard

6.3.1 Methods

In order to determine the accuracy of the bECG QT_c interval and QRS duration, a standard ECG lead is required as a gold-standard. Each of the 12 standard leads is a projection of the heart dipole and is unique in shape. The bECG is a non-standard lead, so correlation analysis was used to determine which of the 12 standard leads most closely matches the bECG. Correlation analysis was performed on the ensemble averaged beats of each lead from every recording. In order to minimize errors that are introduce by timing differences in the R-peak locations, R-peaks from a single channel were used across all 12-leads in order to ensure a consistent reference point when ensemble averaging. The R-peaks from chest lead V1 were chosen as a reference for all other leads as it contained the least amount of motion artifacts.

Pearson's correlation coefficient, which is a measure of the linear correlation between two variables, was used to determine how closely related the ensemble averaged beats were to the bECG beat. This measure is calculated by dividing the covariance of the two variables by the product of their standard deviation. Resulting values are between 1 and -1 (where both extremes represent perfect correlation) Tukey boxplots were generated across the normative subject dataset, with whiskers 1.5 times the interquartile range to show the range of correlations between each lead. A paired Student's t-test is used to determine if the highest correlated leads are statistically equivalent, or if there is a statistically significant difference in the correlation to the bECG.

6.3.2 Results and Discussion

As the heart dipole changes magnitude and orientation during the cardiac cycle, ECG features measured on each differential pair have different timing, amplitude, and orientation. Differences in shape impact the extracted cardiovascular intervals and the clinical interpretation of any given ECG lead, which is easily conceptualized by looking at the differences between the standard 12-lead ECG. In order to determine the lead that the bECG is most similar to, correlation was chosen as it is a quantitative measure of linear dependence between two signals. Correlation results between the bECG and each of the standard 12-leads are shown in Figure 6.1, where the leads are in order of highest median correlation.

The bECG has the highest correlation to Lead II, -aVR, and aVF, with median correlations of 0.911, 0.908, and 0.898 respectively. The correlations for aVR, V1, aVL, and V2 have been inverted to facilitate visual comparison for high negative correlation. Despite having used R-peaks from V1 as reference points for the ensemble averaging of all 12-leads, there is no bias towards V1 in the correlation analysis as it has lower than average correlation to the bECG. Since each of the 12-leads were time synchronized, a paired Student's t-test was used to determine statistical significance for differences in calculated lead correlations, as

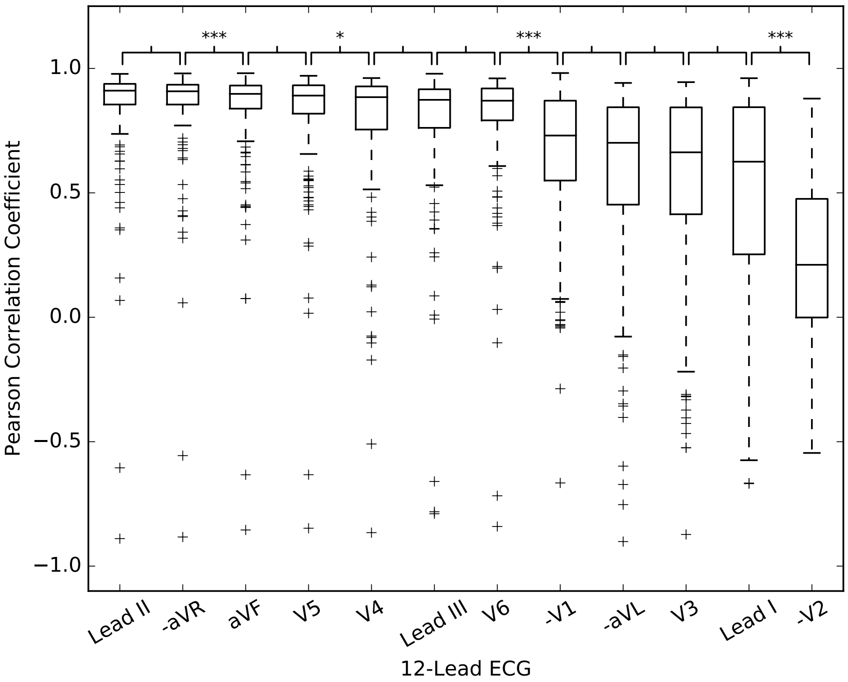

Figure 6.1: Box plots across all normative subjects (N=140) show the correlation between the bECG and the standard ECG leads. Leads aVR, V1, aVL, and V2 have been inverted to facilitate visual comparison. Leads are organized from right to left by best correlation. The top three correlated leads were Lead II, aVR, and aVF with median correlations of 0.911, 0.908, and 0.898 respectively. Statistical significance is tested using a paired Students t-test (*$p < 0.05$, **$p < 0.01$, and ***$p < 0.001$).

shown in Figure 6.1. While there was no statistically significant difference between -aVR and Lead II (p=0.32), Lead II was chosen as the gold-standard for the bECG since -aVR is an augmented lead calculated from Lead II.

6.4 Delineation

6.4.1 Methods

The efficacy of the bECG is evaluated by comparing clinically relevant parameters to those extracted from the highest correlated limb lead, as determined using the methods presented in Section 6.3. Beat classification is used to determine how consistently and accurately beats can be located on the bECG. The bECG signal quality must be sufficient for robust determination of beats, otherwise it cannot be used for further analysis. Six recordings from each normative subject are used in these analyses: five at rest, and one post-stress.

The sensitivity and positive predictive value (PPV) (also known as precision) are then calculated for the bECG waveform using the corresponding beat delineations from the gold-standard ECG channel. Feature locations identified within 100 ms on either side of the gold standard is considered a true positive (TP), while reported time indices that are not within this acceptance interval are false positives (FP). If a corresponding feature is not found within the acceptance interval of the gold standard feature it is considered a missed beat, or a false negative (FN). The interval used when analyzing standard databases is 150 ms based the bxb function provided by PhysioNet [105]. A more stringent acceptance interval of 100 ms was chosen, as it is half the myocardium refractory period of 200 ms [102]. This ensures that multiple beats will not be present for a single gold standard beat within the acceptance window.

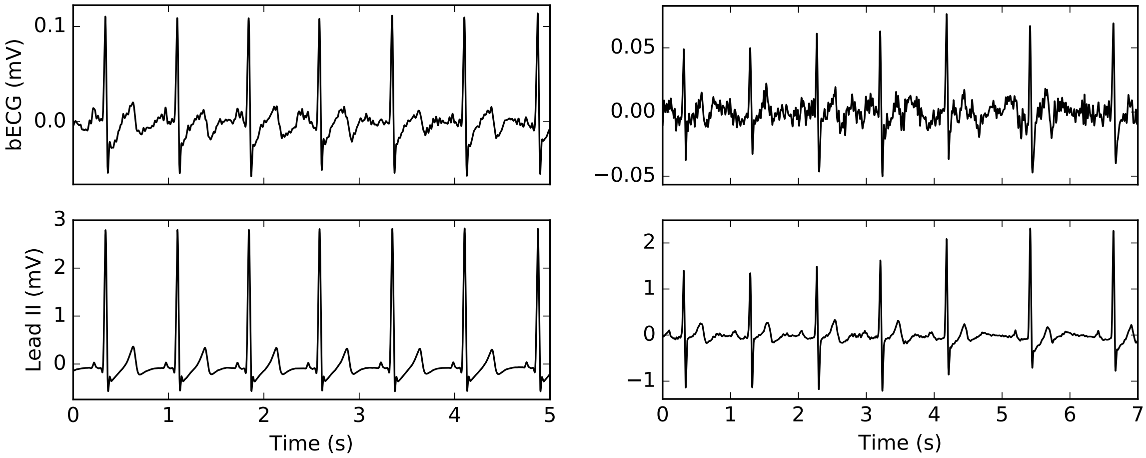

(a) Superior

(b) Average

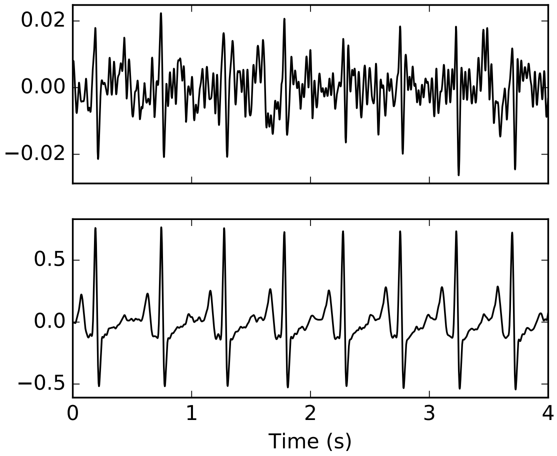

(c) Poor

Figure 6.2: The signal quality of the bECG can change across subjects and measurements as it is captured using active, dry electrodes. Three examples of signal quality are shown for the bECG. The superior example (a) shows the best signal quality achieved from the bECG study. The average example (b) shows the typical signal quality of the bECG. The poor example (c) shows a very noisy waveform that was determined to have sufficient quality for analysis.

6.4.2 Normative Results and Discussion

One fundamental difference between the standard clinical ECG and the bECG is the signal amplitude. Both the electrode location relative to the heart dipole and the type of electrode can reduce signal amplitude. Example bECG waveforms that have been preprocessed with a bandpass filter (1-45 Hz) and notch filter (60 Hz) for visualization are shown in Figure 6.2, illustrating superior, average, and poor signal quality compared to a time synchronized Lead II. Each of these waveforms have passed the SQI test, and were considered to have sufficient quality for analysis. Utilizing signal quality effectively and having robust algorithms is an absolute requirement in this application, since the bECG is acquired using dry electrodes and is much more prone to noise and motion artifacts than typical ECG signals. Despite the challenges with dry electrodes on a toilet seat, the percentage of acceptable waveforms and corresponding sensitivity and PPV is more than sufficient for accurate estimation of physiologic parameters.

One subject was rejected from inclusion in the present study due to a prolonged QRS duration and abnormal ECG morphology, as verified by a cardiologist. Of the remaining 25 subjects, there were a total of 13 male and 12 female subjects ranging from 20 to 50 years of age, with a mean age of 26.7 years. Across 25 subjects with a total of 375 minutes of data, 81.3% of the bECG passed the signal quality algorithm with an overall sensitivity and PPV of 98.7% and 98.5% respectively, compared to Lead II. Summary statistics and per-subject statistics are shown in Table 6.1. Motion artifacts result in transient noise in the bECG waveform as the electrode interface changes whenever the subject moves on the seat. As such, the bECG motion artifacts are more subject dependent than if wet electrode were used. The signal quality across subjects were very polarized, with 16 out of the 25 subjects having over 90% of the bECG waveforms pass the signal quality check compared to subjects 2, 5, and 25 which all had less than 40%. A total of 8 recordings were completely

Subject	**Se**	**PPV**	**SQI Pass**
1	99.8%	99.7%	94.3%
2	95.0%	91.8%	15.8%
3	99.9%	100.0%	93.9%
4	94.4%	97.4%	66.9%
5	99.6%	98.7%	37.8%
6	96.4%	97.1%	91.6%
7	99.3%	98.8%	96.7%
8	99.9%	99.4%	92.0%
9	97.1%	97.1%	65.0%
10	98.2%	97.5%	84.2%
11	99.7%	98.9%	94.9%
12	99.7%	99.1%	95.4%
13	99.9%	100.0%	98.1%
14	99.9%	99.8%	93.8%
15	100.0%	99.9%	94.3%
16	99.0%	98.6%	91.8%
17	99.5%	99.0%	74.6%
18	99.8%	98.0%	91.0%
19	99.9%	99.4%	95.8%
20	97.6%	98.3%	93.8%
21	100.0%	99.6%	91.7%
22	98.2%	98.8%	83.1%
23	86.9%	85.9%	75.9%
24	96.6%	98.2%	91.2%
25	97.4%	96.4%	29.6%
Total	98.7%	98.5%	81.3%

Table 6.1: Buttocks ECG QRS Classification Results for Normative Subjects

rejected because 100% of the waveform in those recordings failed the signal quality metric for QRS delineation.

6.4.3 Heart Failure Results and Discussion

ECG R-peaks were delineated using a custom, automated algorithm following acceptable region identification with the SQI algorithm. 25 subjects were evaluated, none were excluded. The SQI algorithm resulted in 64.8% of the bECG having sufficient quality for analysis. Data rejection was polarized, with 16 subjects having over 60% of bECG segments accepted, and 6 subjects having less than 25%. Many HF subjects have a patient monitoring system, an IV, and a swan catheter at all times, which periodically resulted in poor Lead II signal quality. On average, 92.8% of Lead II data had acceptable signal quality. Only periods when both the bECG and Lead II had acceptable signal quality were analyzed. Further investigation is required to explore causative factors impacting robust bECG capture in the HF subject population.

The sensitivity and positive predictive values were then calculated for the bECG waveform using the Lead II ECG as the gold standard reference. Results are presented in Table 6.2 for all subjects. A total of 179 recordings were analyzed, of which 158 were of suitable quality for inclusion in the analysis (i.e. some part of them passed the automated SQI algorithm for both bECG and Lead II). An overall sensitivity of 79.2% suggests the bECG provides sufficient waveform quality to enable robust R-wave determination as compared to the standard Lead II ECG. Similarly, the positive predictive value (PPV) of 83.7% suggests a reasonably high true positive rate. Both measures used an acceptance interval of ±75 ms. Given the abnormal QRS morphology in the HF subjects, the normative R-peak delineator may find a location anywhere within the QRS as an R-peak. A typical QRS duration for

Subject	Se+	PPV	SQI Pass
101	95.4%	93.1%	94.9%
102	88.7%	95.3%	57.3%
103	78.2%	90.2%	79.8%
104	6.9%	50.0%	2.5%
105	84.3%	95.4%	59.5%
106	64.6%	65.6%	96.2%
107	92.0%	99.2%	92.7%
108	77.1%	74.8%	63.2%
109	94.0%	94.5%	92.3%
110	82.2%	77.6%	98.8%
111	53.6%	62.0%	42.0%
112	57.9%	64.9%	77.3%
113	53.6%	54.9%	79.4%
114	98.5%	96.7%	21.1%
115	12.6%	12.9%	94.0%
116	3.6%	14.8%	7.8%
117	55.9%	76.9%	79.0%
118	54.1%	57.5%	13.6%
119	90.0%	99.5%	99.0%
120	99.5%	99.9%	96.0%
121	81.0%	92.3%	88.6%
122	37.5%	51.9%	53.2%
123	60.1%	80.7%	24.6%
124	70.3%	75.4%	86.0%
125	34.9%	36.5%	13.4%
Overall	79.2%	83.7%	64.8%

Table 6.2: Sensitivity, positive predictive value, and percentage of waveforms that pass SQI in the analysis for the HF subjects.

a HF patient is great than 120 ms, and in extreme circumstances can be over 150 ms. The same acceptance interval used for the normative analysis (±100 ms) was chosen. After subject testing was initiated, many of the first patients had ECG amplitudes much lower than expected. Lower ECG amplitude can be attributed to massive cell death in cases of extreme heart failure.

6.5 Heart Failure Arrhythmia Analysis

6.5.1 Methods

In order to show that the FIT bECG can be used for arrhythmia analysis, professional grade Holter analysis software (M12A Holter System software by Global Instrumentation) was used to detect arrhythmias on both the FIT bECG and Lead II ECG after initial preprocessing and filtering. The following parameters were calculated using this software:

1. Number of beats located
2. Number of ventricular ectopic beats
3. Number of supraventricular ectopic beats
4. Average HR

The total number of beats located and the average HR are compared to those found using the custom algorithms discussed in Section 6.4. The Holter software does not classify signal quality, and as such will find a different number of beats for the FIT bECG compared to the Lead II ECG. Comparing the HR and beats located to custom algorithms provide a reference for comparing the number of ectopic beats between the FIT bECG and Lead II ECG. This also provides a frame of reference for what is expected from a professional grade ECG delineation and analysis algorithm. Recordings from Protocol 1 are only 2.5 minutes in length, making them ill-suited for use with the Holter software, which has been designed for use with longer recordings. One recording (from Heart Failure Protocol 2) was used for the arrhythmia analysis with the Holter software, as it is typically over 5 minutes in length.

6.5.2 Results and Discussion

Each of the 25 files from the heart failure population were manually converted to a format the Holter software could analyze. The bECG is a non-standard lead and has a much lower amplitude than the standard leads. As such, the software was unable to analyze 14 of the 25 recordings. In these cases, the software found fewer than 50% of the FIT bECG beats compared to the Lead II ECG (rejection criteria). These recordings were excluded from the arrhythmia analysis. The noise present on the bECG is atypical of a chest worn ECG with gel electrodes, which will negatively impact the software's ability to correctly classify and delineate beats.

As expected, the correlation between the FIT bECG and the Lead II ECG heart rate is very high for the 9 recordings analyzed, as shown in Figure 6.3-(a). The percent of ventricular and supraventricular ectopic beats are shown in Figure 6.3-(b) and Figure 6.3-(c) respectively. These values are compared as percentages, since the total number of beats located are different for the bECG and the Lead II ECG. This is also the default output for the Holter software, as it is typically used to report on an entire 24 hours (or more). These percentages correlate very well for the relatively small number of beats present in the recordings. This highlights the power of the bECG in capturing important arrhythmia

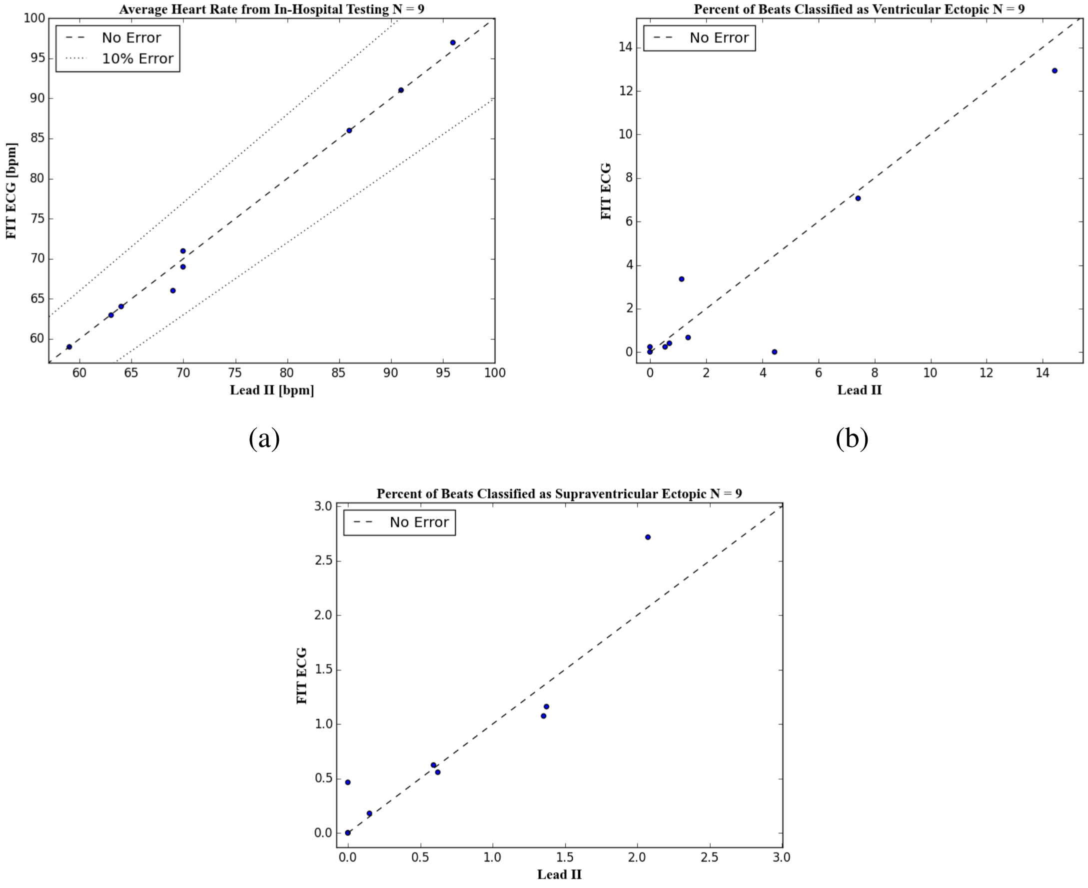

(a)

(b)

(c)

Figure 6.3: The average heart rate for the bECG very closely matches the heart rate from the Lead II ECG (a), the percentage of heart beats in the bECG that are classified as a ventricular ectopic beat closely match the Lead II ECG (b), and the percentage of heart beats in the bECG that are classified as a supraventricular ectopic beat closely match the Lead II ECG (c) as determined by the commercial Holter analysis software for the HF population.

information from shorter uses of the FIT seat.

6.6 Cardiac Intervals

6.6.1 Methods

For each recording the HR, HRV, QRS duration, and QT_c interval measured from the bECG are compared to the gold standard limb lead with the highest correlation to the bECG. The HR for a specific recording is calculated by taking the median RR interval after rejecting RR intervals that were more than 60% out of tolerance to the initial median RR interval. Multiple methods can be used to calculate HRV, however in this work the standard deviation of the RR intervals (SDNN) is used.

QT_c and QRS intervals are extracted from the delineated feature timing on the ensemble averaged waveform for both the bECG and Lead II ECG. Results are compared using Bland-Altman plots. Correcting the QT interval for different heart rates is necessary when looking for trends or comparison across recordings. The corrected QT interval (QT_c) is calculated using the Bazett formula [40].

6.6.2 Normative Results and Discussion

Heart rate and heart rate variability are calculated per recording for the bECG and Lead II ECG waveforms for all subjects at rest and post-stress. A total of 142 recordings were analyzed with matched pairs shown as a Bland-Altman plot in Figure 6.4. The automated delineation algorithms resulted in an excellent agreement between the bECG and the gold-standard HR, with all data points having less than 2 bpm error and virtual no bias. The SDDN heart rate variability is clustered very close to the zero error line, but with positive bias induced by a small number of significant outliers. While the results are excellent for a dry electrode system and no skin preparation, further enhancements to the automated SQI algorithm may offer opportunities to further improve results.

The more stringent requirements on signal quality when creating the ensemble averaged beats result in the rejection of additional segments compared to the statistics described in Table 6.1; on average 85.9% of the delineated R-waves in Table 6.1 were used to generate ensemble averaged beats. Results are presented as Bland-Altman plots for the bECG QRS duration and QT_c interval in Figure 6.5 (a) and (b).

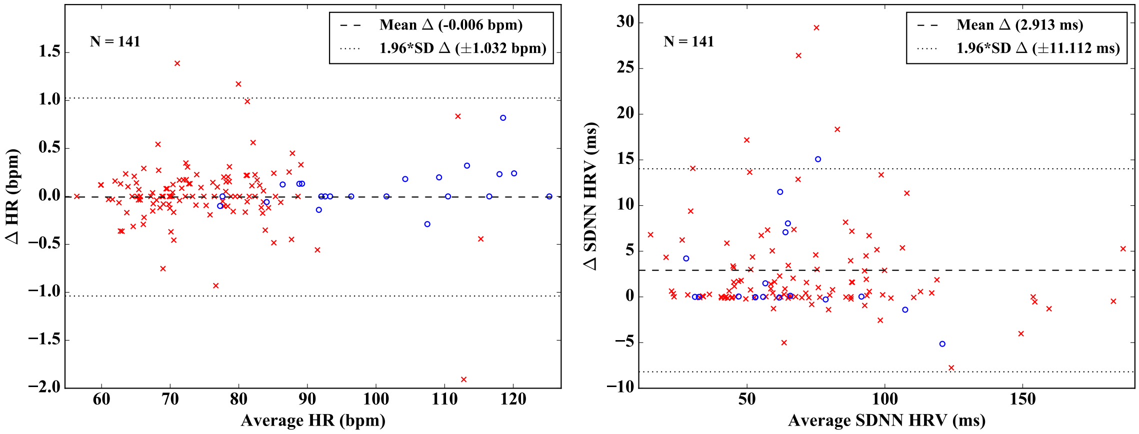

(a) (b)

Figure 6.4: Heart rate (a) and heart rate variability (b) extracted from the bECG signal for both rest (red x) and post-stress (blue o) are closely aligned with those extracted from the gold standard Lead II ECG. The dashed line shows the mean error, while the dotted lines show 1.96 times the SD corresponding to a 95% limits of agreement.

The bECG QRS durations are generally within 10 ms compared to those extracted from the Lead II ECG. The Bland-Altman plot show near zero bias in the measures and a 1.96 times standard deviation of 14.56 ms. The visible 1 ms quantization in Figure 6.5 (a) is caused by

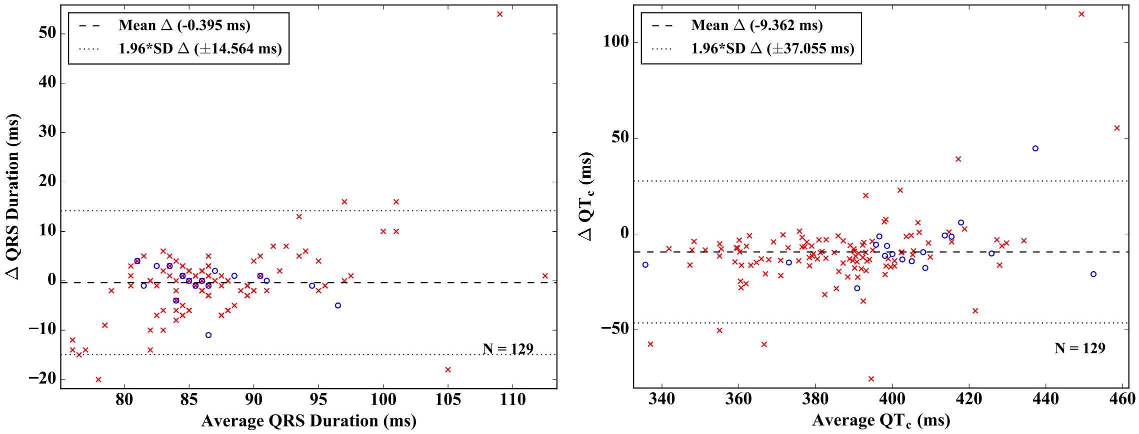

(a) (b)

Figure 6.5: The error in the bECG QRS duration compared to Lead II (a) shows a very low error of less than 15 ms (for within 95% limits of agreement), corresponding to 15 samples. The QT$_c$ interval (b) shows excellent agreement between the bECG and Lead II extractions compared to what can be achieved though manual determination with a caliper (between 20-40 ms) [125]. Data points for both rest (red x) and post-stress (blue o) are shown.

the 1000 Hz sampling rate. The bECG based QT$_c$ interval extractions are generally within 25 ms of those extracted from the Lead II ECG, with an overall negative bias. The Bland Altman plot shows a -9.36 ms bias in the QT$_c$ interval with an error of 37.06 ms (1.96 times the SD). Manual determination of QT interval with a caliper has an error between 20-40 ms [125], and for four different automated approaches the standard deviation in QT differences to a gold-standard is over 20 ms for each [126].

This indicates that the bECG QT$_c$ interval compared to the gold-standard, which has a standard deviation of 18.91 ms, is more than sufficient for diagnostic purposes. A small number of significant outliers greatly impact the error calculated from the standard deviation. Since the Q, S and T wave feature locations are more sensitive to noise than the R-wave delineation, improved signal quality classification algorithms have the potential to improve QRS duration and QT$_c$ interval estimation more so than the other results presented herein.

6.6.3 HF Results and Discussion

The bECG was captured on HF subjects using fully integrated instrumentation in the FIT seat and compared to the traditional Lead II ECG. While the Lead II ECG is captured with traditional adhesive gel electrodes on the chest, the bECG relies on dry skin contact with the buttocks and is more sensitive to motion artifacts. These motion artifacts result in transient noise in the bECG waveform. The automated SQI algorithm rejects these regions of poor signal quality. The accepted segments can then be used for feature delineation and waveform averaging. Examples from two subjects of Lead II and bECG ensemble averaged waveforms are shown in Figure 6.6. While these waveforms present new challenges for feature delineation algorithms due to their non-standard shape, the bECG reliably captures waveform morphology as compared to the Lead II ECG.

Heart rate was calculated per recording for the bECG and Lead II ECG waveforms for 25 heart failure subjects at rest. A total of 158 recordings were analyzed with matched pairs plotted in Figure 6.7. The automated algorithms for R-wave determination resulted in an excellent agreement between the two lead vectors, with nearly all data aligned along the perfect correlation line, and all but three values well within the ±10% error bounds.

The algorithms for estimating HRV, QRS, and QTc interval failed to produce acceptable results on the HF population. They were developed for the normative subject population with classic ECG morphology. However, this HF population has non-standard waveforms; some with additional waves within the QRS complex resulting in delineation errors. Additional work is required to refine the algorithms for robust and consistent time accuracy on the identified features. The current algorithms fail on both the bECG and Lead II ECG waveforms, suggesting a fundamental algorithm issue rather than challenges with the bECG specifically.

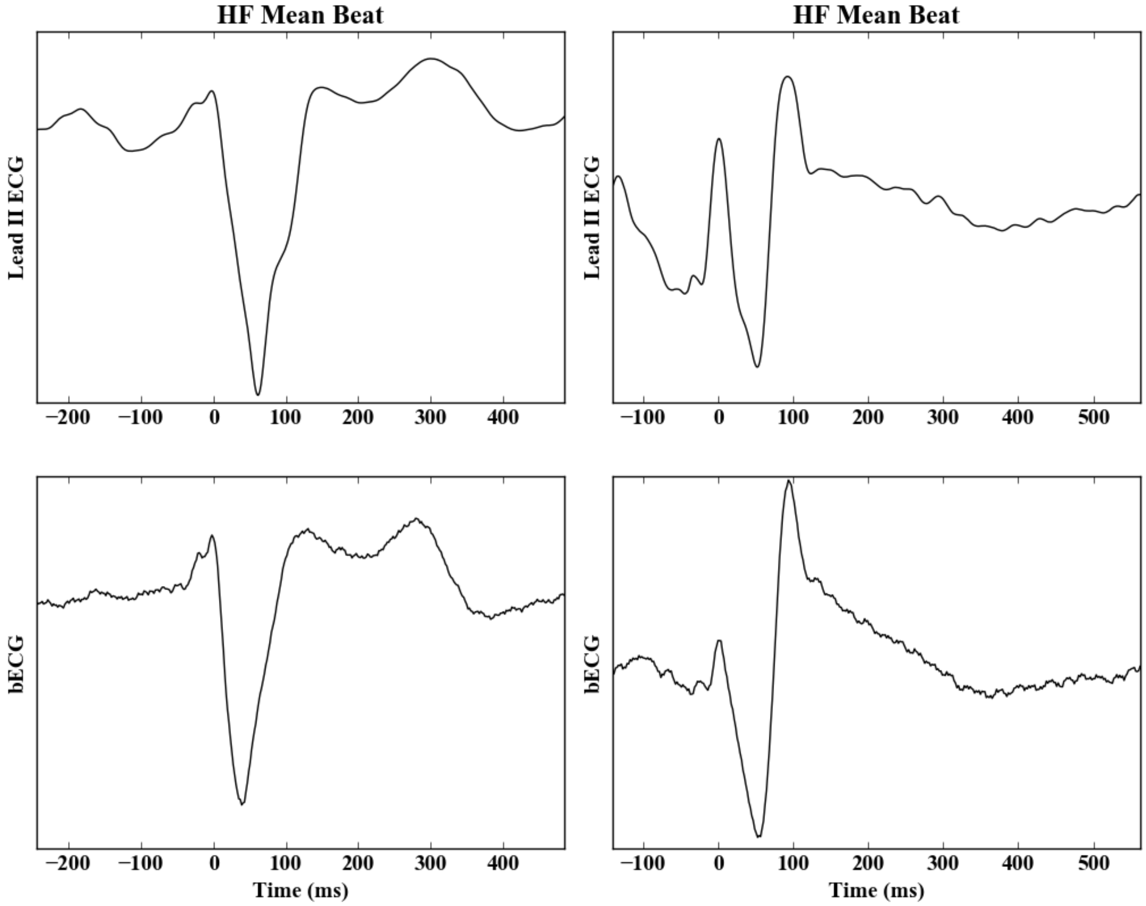

(a) (b)

Figure 6.6: Example ensemble averaged waveforms from two heart failure (HF) subjects (a) and (b) with Lead II (top) and bECG (bottom). The bECG reliably captures waveform characteristics in this diseased population, but the non-standard waveform shape creates challenges for feature delineation.

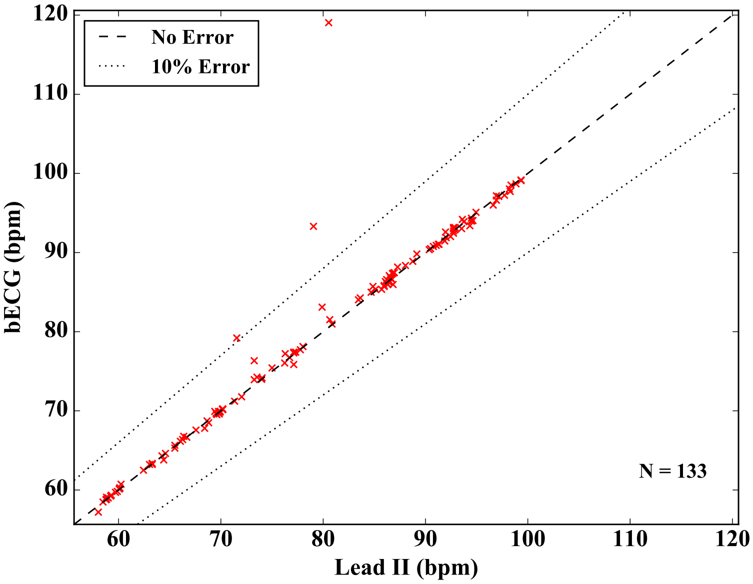

Figure 6.7: Heart rate extracted from the bECG signal are closely aligned with those extracted from the gold standard Lead II ECG. The dashed line represents perfect correlation, while the dotted lines represent ±10% error. Data from 25 heart failure subjects.

6.7 Conclusion

The work presented herein demonstrates that a toilet seat based dry electrode buttocks ECG (bECG) provides robust determination of HR, HRV, QRS duration, and QT_c interval as compared to a standard Lead II ECG captured using traditional gel electrodes. Advanced ECG signal processing algorithms custom designed for noisy, dry electrode ECG signals have been presented for use with the bECG. A key component of these algorithms is the classification of ECG signal quality, which allows automatic rejection of noisy segments before feature delineation and interval extractions. The bECG was most closely correlated to standard Lead II with an average HR and HRV accuracy of 0.02±0.5 bpm, and -3.33±12.27 ms respectively. Similarly, the estimated QRS duration has an accuracy of -0.38±6.6 ms and the QT_c interval has an accuracy of -9.8±22.6 ms. By further improving the signal quality classification algorithm, it is expected that the accuracy of all the bECG measures compared to a gold-standard Lead II will be greatly improved.

These results lay the foundation for future studies by demonstrating the accurate extraction of key cardiac intervals from the bECG as compared to a clinical gold-standard on a normative population. Future studies will investigate the clinical utility of the bECG for heart failure subjects and the ability of a deployed, self-contained, toilet seat based system to monitor long-term trends in the home. Such a device has the potential to capture long-term trend data that has been previously unattainable, as it facilitates daily measurements taken at rest prior to food and stimulants (e.g. caffeine, nicotine, etc.) at consistent times each day, with no required change in habit. This, in combination with intra-day circadian trends will enable new approaches and capabilities in the diagnosis and treatment of cardiovascular disease for those with heart failure, hypertension, and those undergoing chemotherapy treatments.

Chapter 7

BCG, PPG, and Blood Pressure

7.1 Introduction

Robust non-invasive absolute blood pressure estimation using pulse wave velocity (PWV) has not been demonstrated in literature. Many devices exist that require a patient based calibration that is only valid for the current physiologic state [51, 127, 128, 129]. The ability of these systems to produce accurate blood pressure measurements break down over time and require constant recalibration.

This chapter discusses the steps needed to robustly estimate blood pressure from the FIT seat using PWV. A per-subject calibration is used, which will not break down over time. This calibration leverages a first principle, physics based hemodynamic model of the aorta to generate a per-subject calibration that is ultimately used to estimate diastolic blood pressure [130, 131, 132, 133]. The BCG is used for proximal timing of the pulse transit time and the bPPG is used for distal timing. Advanced signal processing techniques allow for the robust extraction of timing features from the BCG and bPPG. Extreme accuracy is critical when calculating the pulse wave velocity, as small timing differences result in large blood pressure variation.

7.2 PPG Delineation

The PPG plays an integral roll in the estimation of blood pressure, since accurate peripheral pulse wave timing is critical to the extraction of the pulse transit time. This sections demonstrates that the bPPG on the FIT seat contains robust foot timing that can be used for blood pressure estimation.

7.2.1 Thigh Cuff as Failed Gold-Standard

It was initially believed that a thigh cuff based plethysmogram could be used as a gold standard for FIT bPPG timing. As the pressure necessary to acquire a pulse varies based on a subject's blood pressure the effects of pressure on feature timing was also investigated. The timing consistency of the thigh cuff foot was tested on three subjects, for pressures between their systolic and diastolic BP.

A single recording for each subject was captured, where the thigh cuff pressure was slowly decreased from 10 mmHg above the subject's systolic BP to 10 mmHg below their diastolic. The delay between the R-peak and the foot of the thigh cuff plethysmogram was used to determine the time shift of the foot relative to pressure. A plot is generated showing the

R-peak to thigh cuff foot timing on a beat-to-beat basis for the entire recording.

In order for the thigh cuff to be used as an acceptable gold standard, the foot locations must be consistent across a range of cuff pressures. As demonstrated in Figure 7.1, the location of the thigh cuff foot varies drastically as the thigh cuff pressure is changed. These figures show how the foot location changes as the thigh cuff is deflated from 10 mmHg above a subject's systolic BP to 10 mmHg below a subject's systolic BP. This process was repeated twice, as indicated in the figure.

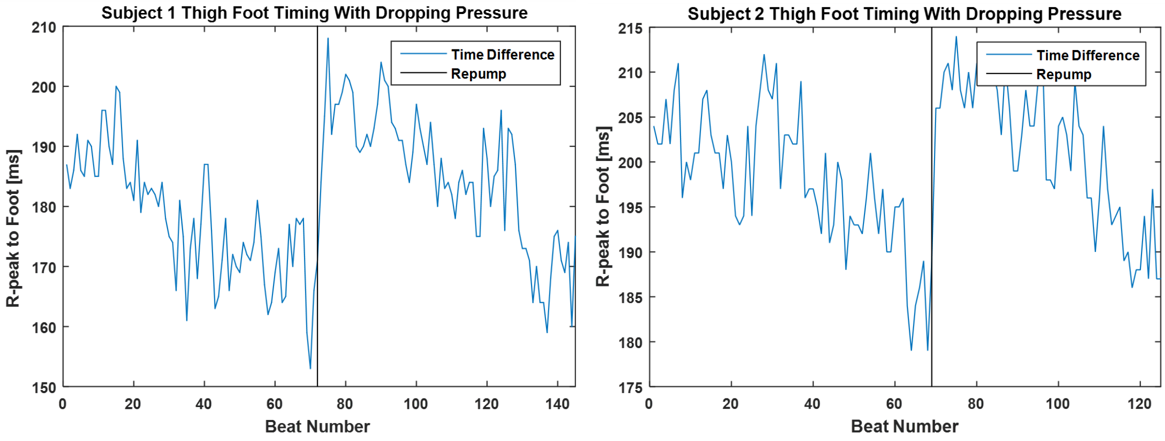

(a) (b)

Figure 7.1: Change in thigh cuff foot timing for Subject 1 (a) and Subject 2 (b) relative to R-peaks from a Lead II ECG as the thigh cuff pressure varies across time.

Both subjects show a change of over 30 ms between systolic and diastolic pressures. These results are valid under the assumption that the pulse arrival time is not drastically changing throughout the course of the recording (2 minutes). This indicates that the thigh cuff based foot locations cannot be used as an accurate temporal gold standard for the bPPG.

Given that the thigh cuff is only present during a small percentage of a subject's overall data and that there is a variable time shift between features, better options exist for determining bPPG foot classifications. The ECG R-peaks from Lead II are better suited for this purpose, given that it is a very clean and reliable signal present continuously throughout all recordings. Assuming that the pulse arrival time does not change drastically within a single recording, the difference between the ECG R-peaks and bPPG feet can be considered a per-recording constant and removed before classification.

7.2.2 Buttocks PPG (bPPG) Delineation Results

Methods

The FIT bPPG is used to estimate both pulse transit time and blood oxygenation (SpO2). The efficacy of the FIT bPPG was determined by comparing waveform delineations to those found in a gold-standard Lead II ECG waveform. Custom algorithms were developed to automatically assess signal quality and reject noisy waveform segments as described in Chapter 4. The bPPG foot locations are found in order to preliminarily locate each beat. These locations are found using a derivative based method with a narrow bandpass filter. For this study, the bPPG foot is defined as the maximum point in the second derivative (point of maximum upward acceleration).

Once the foot locations are found, a neighborhood is defined for each beat and the beat under test is compared to the beats within the neighborhood using correlation. If the correlation is below a pre-determined threshold, the beat is considered to be of poor quality. This correlation based SQI is generated on a beat-by-beat basis, with accepted and rejected regions determined using a simple threshold in combination with segment length criteria. The percent of data rejected is captured in the delineation statistics. Final foot locations were then recalculated taking into account signal quality classifications. This ensures that noisy parts of the signal do not cause incorrectly delineated beats.

The sensitivity and PPV of the bPPG feet are found using the Lead II R-peaks as a gold-standard. An acceptance interval of ±75 ms was chosen over a small interval, since it will better indicate how many beats were correctly located rather than how accurate the delineations are in time. This is especially important since the delay between ECG R-peaks and bPPG feet is not constant on a beat-by-beat basis. The time shift between these two features is called the pulse arrival time, and it needs to be removed before classifying each beat. The average delay between the R-peak and bPPG foot is found using cross correlation. To visualize ability of the bPPG to accurately estimate the heart rate (HR), the bPPG based HR is plotted versus the corresponding Lead II extractions.

Normative Results and Discussion

The sensitivity and positive predictive values were then calculated for the bPPG feet using the Lead II ECG R-peak as the gold standard reference. Results are presented in Table 7.1 for all subjects across rest and post-stress protocols. A total of 150 recordings were analyzed. Approximately 45% of all bPPG data was of suitable quality for inclusion in the analysis (i.e. they pass the automated SQI algorithm). While this number is much lower than the bECG, it still results in sufficiently long regions of acceptable bPPG that can be used to estimate HR, pulse transit time, and SpO_2.

The bPPG within in the FIT seat that was used for normative testing was a very early prototype. Due to DAQ restrictions (all data was continuously acquired on a single DAQ), the two wavelength bPPG could not be pulsed as is typically done. As such, the bPPG consisted of two photodetectors each outfitted with optical filters to separate out each wavelength. These filters result in attenuation of the bPPG. Furthermore, the added distance between the photodetector and the body resulted in additional attenuation of an already small sig-

Subject	Sensitivity	PPV	Pass SQI
3	86.6%	96.7%	44.2%
4	64.0%	89.3%	43.2%
5	82.1%	92.3%	40.7%
6	95.8%	98.9%	84.5%
7	76.5%	91.3%	16.7%
8	88.4%	95.3%	41.4%
9	73.8%	90.9%	12.8%
14	73.3%	89.4%	26.2%
15	77.8%	94.8%	26.6%
21	91.0%	97.4%	72.6%
24	85.3%	92.8%	30.6%
26	74.2%	86.8%	39.7%
27	96.0%	99.1%	87.5%
31	88.7%	93.7%	61.6%
32	86.2%	92.3%	9.3%
33	97.2%	99.6%	90.8%
35	70.9%	82.0%	6.2%
36	85.3%	95.2%	57.6%
38	70.4%	87.1%	13.8%
41	96.3%	99.3%	82.4%
44	88.2%	96.1%	64.1%
63	89.0%	95.7%	56.9%
84	80.3%	88.4%	22.7%
85	93.5%	99.1%	74.9%
88	64.9%	73.0%	10.2%
Overall	**89.8%**	**96.5%**	**45.2%**

Table 7.1: Sensitivity, positive predictive value, and percentage of waveforms that pass SQI in the bPPG analysis for the normative subjects at rest and post-stress.

nal. Supply noise was also problematic since this prototype used for normative testing was more prone to mains noise than future the current version of the seats. These issues have all been addressed in the next current version of the seat, which uses a custom integrated PPG AFE that pulses each LED (removing the need for optical filters) and optimizes signal to noise ratio on a per-sample basis.

Despite lower than desired signal quality, the overall sensitivity of the bPPG was still 89.8%. The much higher positive predictive value (PPV) of 96.5% suggests a very high true positive rate compared to the sensitivity. This is a desirable algorithm behavior, since it is better for the algorithm to miss beats than to incorrectly identify beats where none exist.

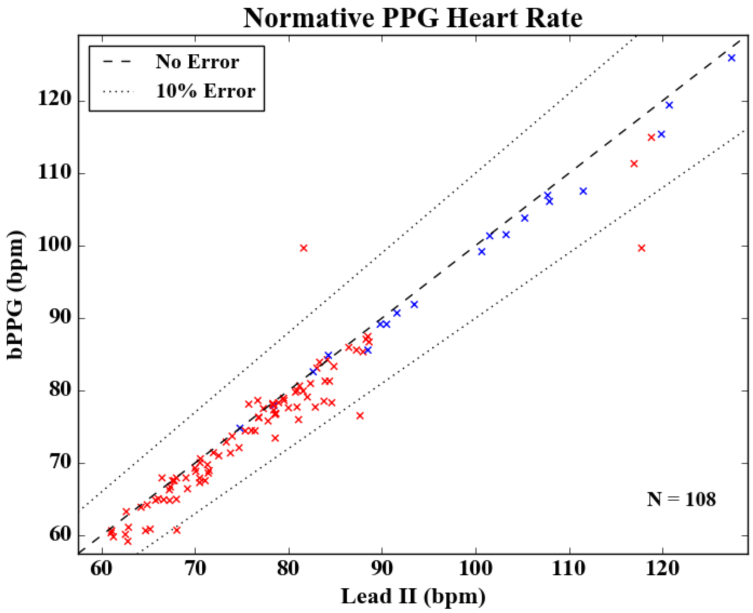

Figure 7.2: Heart rate as extracted from the bPPG signal is closely aligned with that extracted from the gold standard Lead II ECG. The dashed line represents perfect correlation, while the dotted lines represent ±10% error. At rest (red) and post-stress (blue) extractions are shown.

Heart rate is calculated per recording for the bPPG and Lead II ECG waveforms for 25 normative subjects at rest and post-stress. A total of 108 recordings were analyzed with matched pairs plotted in Figure 7.2. The automated algorithms for PPG foot detection resulted in an excellent agreement between the two lead vectors, with nearly all data well within the ±10% error bounds. The errors in HR are likely due to noise in the bPPG waveform impacting delineation accuracy. While the results are excellent for the system as described, further enhancements to the bPPG instrumentation and optics are expected to significantly improve results.

Heart Failure Results and Discussion

The sensitivity and positive predictive values were then calculated for the bPPG feet using the Lead II ECG R-peak as the gold standard reference. Results are presented in Table 7.2 for all subjects across protocols 1 and 2 (Chapter 5). A total of 179 recordings were analyzed. Approximately 51% of all bPPG data was of suitable quality for inclusion in the analysis (i.e. they pass the automated SQI algorithm). While this number is much lower than the bECG, it still results in sufficiently long regions of acceptable bPPG that can be used to estimate HR, pulse transit time, and SpO_2.

The overall sensitivity of the bPPG was still 88.4%. The much higher positive predictive value (PPV) of 93.1% suggests a very high true positive rate compared to the sensitivity. This is a desirable algorithm behavior, since it is better for the algorithm to miss beats than to incorrectly identify beats where none exist. These results show an overall improvement in signal quality by approximately 6% compared to normative subject testing despite the reduction in signal quality with the HF population. This is attributed to enhancements made with the integrated electronics.

Heart rate is calculated per recording for the bPPG and Lead II ECG waveforms for 25 heart failure subjects at rest. A total of 179 recordings were analyzed with matched pairs plotted in Figure 7.3. The automated algorithms for PPG foot detection resulted in an excellent agreement between the two lead vectors, with nearly all data well within the ±10% error bounds. The errors in HR are likely due to motion artifacts in the bPPG waveform impacting delineation accuracy.

Subject	**Sensitivity**	**PPV**	**Pass SQI**
101	40.7%	93.8%	5.3%
102	97.4%	98.8%	77.8%
103	76.1%	90.5%	36.7%
104	41.6%	99.2%	23.1%
105	96.6%	98.6%	76.8%
106	84.6%	90.3%	55.6%
107	84.3%	96.0%	70.0%
108	79.9%	85.2%	61.6%
109	74.8%	92.6%	13.2%
110	33.3%	62.5%	1.0%
111	68.5%	68.8%	85.1%
112	96.5%	94.4%	65.4%
113	79.3%	85.7%	43.7%
114	81.9%	80.4%	49.5%
115	98.9%	100.0%	96.1%
116	94.3%	98.5%	77.2%
117	94.7%	96.1%	74.7%
118	89.0%	83.5%	40.3%
119	94.4%	99.2%	81.4%
120	77.4%	97.9%	18.8%
121	80.0%	94.0%	40.3%
122	85.0%	82.5%	59.1%
123	95.8%	98.5%	81.9%
124	96.7%	96.9%	97.4%
125	93.4%	96.5%	89.1%
Overall	**88.4%**	**93.1%**	**51.4%**

Table 7.2: Sensitivity, positive predictive value, and percentage of waveforms that pass SQI in the bPPG analysis for the normative subjects at rest and post-stress.

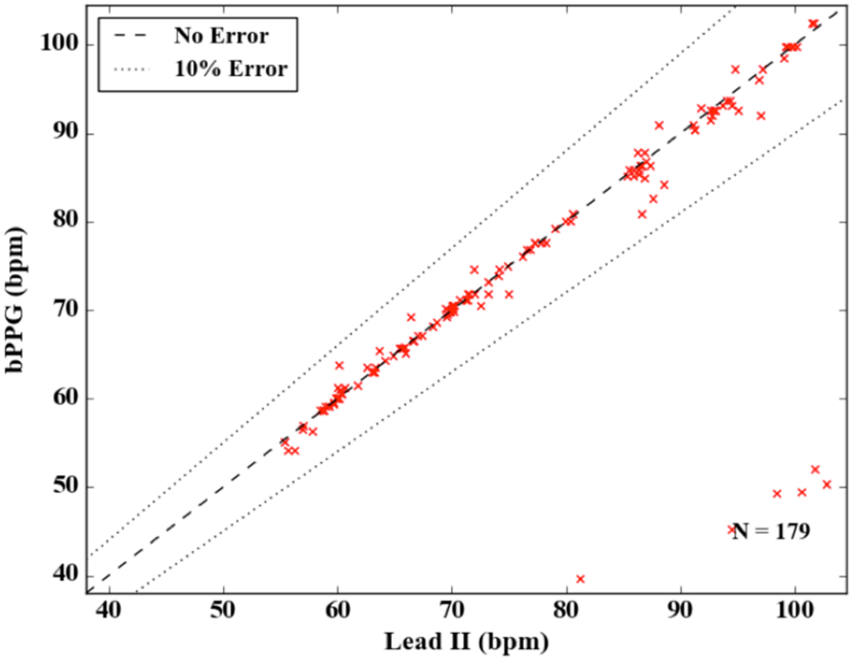

Figure 7.3: Heart rate as extracted from the bPPG signal is closely aligned with that extracted from the gold standard Lead II ECG for the HF population. The dashed line represents perfect correlation, while the dotted lines represent ±10% error.

7.3 Blood Pressure and BCG Timing

7.3.1 Methods and Calibration

Arterial radii and wall thickness in the aorta are measured using an ultrasound machine at systolic by a cardiologist (Karl Q. Schwarz, MD), diastolic and mean arterial blood pressures [130]. An example capture from the ultrasound machine is shown in Figure 7.4, where three measurements are taken for each blood pressure.

By capturing these features at multiple pressures, a physics based model can be used to create a subject specific PWV_p (pressure dependent pulse wave velocity) to blood pressure curve (Figure 7.5). This is used to estimate diastolic BP. From this curve, a 6 ms time shift

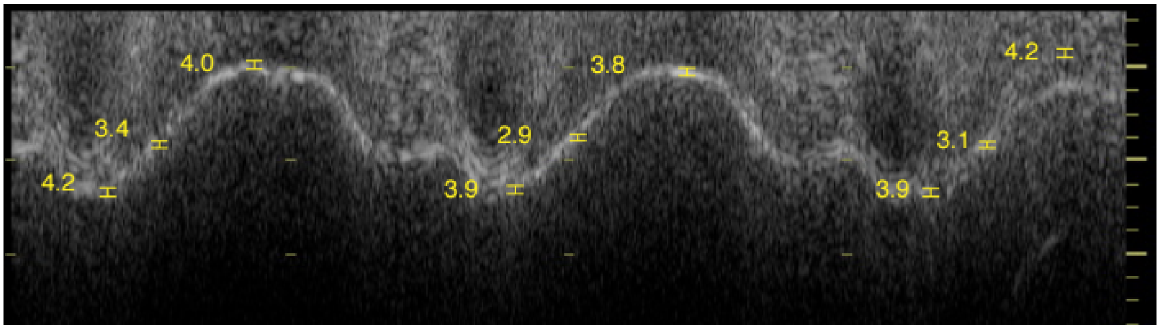

Figure 7.4: Example calibration measurements from a test subject, captured from a GE Vivid i echocardiogram. The aortic wall thickness is measured at three distinct arterial pressures. These values are used to create a PWV to BP curve from a physics based model.

in the pulse transit time (for a subject with an aortic length of 0.63 m) corresponds to a 10 mmHg shift for diastolic blood pressure. This highlights the need for the algorithms developed throughout this work, which focuses on a high temporal accuracy for delineated features.

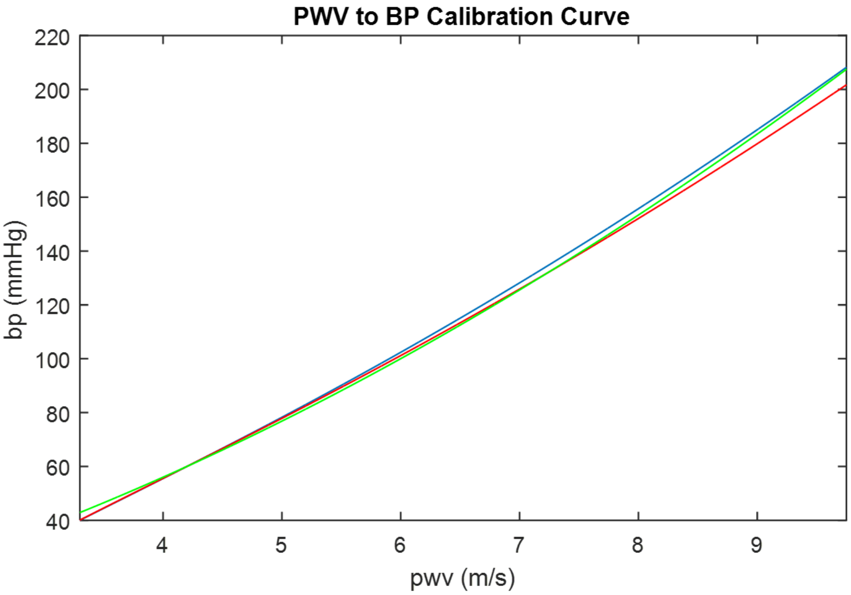

Figure 7.5: From the ultrasound based calibration, the pulse wave velocity to blood pressure curve is created using the first principle physics based hemodynamic model of the aorta. Three curves are shown, based on errors in the aortic measurements.

The measured PWV from the FIT seat ($\mathrm{PWV_m}$) consists of both the pressure dependent PWV ($\mathrm{PWV_p}$) and a flow velocity ($\mathrm{V_f}$), as shown in (7.1) [131, 132]. The flow velocity is the bulk flow of blood due to ventricular ejection, while the pressure dependent PWV is created during ejection. The pressure dependent PWV, which is used to estimate blood pressure using the subject calibration curve, cannot be measured directly, except when the flow velocity is zero.

$$PWV_p + V_f = PWV_m \tag{7.1}$$

In diastole, the flow velocity is zero, making the measured PWV equal to the pressure dependent PWV. For systolic blood pressure, the flow velocity is non-zero. In order to estimate systolic blood pressure using the physics based model, the flow velocity first needs to be estimated and subsequently subtracted from the measured PWV. The pulse wave velocity can be calculated from the pulse transit time and the aortic length (measured as described in Chapter 5).

7.3.2 In-Home Data

A single subject underwent the calibration procedure described Section 7.3.1, the result of which is an individualized $\mathrm{PWV_p}$ to BP curve. The resulting aortic dimensions are shown in Table 7.3. The same subject used a FIT seat in their home for the duration of this test. The subject was instructed to measure their blood pressure three times before sitting on the FIT seat. Multiple blood pressure recordings were required due to the high variability of in-home automated blood pressure cuffs. The three blood pressure readings (taken using an Omron 10 Series BP786N Upper Arm cuff) are used to calculate an average gold-standard blood pressure for each FIT recording, creating a single time point for this test. The subject was also instructed not to perform a bowel movement (BM) during this event, as blood

Ao Diameter Diastole (cm)	2.9390
Ao Diameter Mid Systole (cm)	3.0473
Ao Diameter End Systole (cm)	3.0753
Ao Wall Diastole (cm)	0.1663
Ao Wall Mid Systole (cm)	0.1117
Ao Wall End Systole (cm)	0.1157

Table 7.3: Aortic Dimensions for BP Calibration

pressure is expected to change during a BM.

A total of 38 blood pressure events were captured by the subject throughout the course of 11 weeks. 36.8% of the events were rejected due to poor signal quality in the FIT recordings. This is expected, as the FIT seat was not in a controlled hospital or laboratory environment. The resulting 24 events were then used to estimate the subject's blood pressure over time.

7.3.3 BCG Interval Timing

A FIT seat based pulse transit time (PTT) can be calculated by using the bBCG for proximal timing and the bPPG for distal timing. The $\mathrm{PWV_m}$ is calculated from the measured PTT and an aortic length, where the aortic length is estimated from a combination of superficial and ultrasound based measurements. For the diastolic pulse transit time, the starting point (proximal) is the moment of ventricular ejection and the end point (distal) is the onset of the peripheral pulse. For systolic pulse transit time, the starting point is the moment of peak flow velocity, which approximates peak ejection pressure, and the end point is the moment of peak pressure at the peripheral pulse.

The timing of each BCG feature is compared to the ultrasound based valve opening time, shown in Figure 7.6. These results were generating using manual annotations of the BCG, not automated algorithms. Figure 7.6-(a) shows the offset and standard deviation of each BCG feature compared to aortic valve opening, while Figure 7.6-(b) compares the same feature to the moment of peak velocity. The gold standard timing values for valve opening and peak ejection were measured from a simultaneous ultrasound captured on each normative subject. The start of diastolic pulse transit time (valve opening) is not well defined on the BCG, as the closest feature (G-wave) has a large standard deviation. The I-wave, despite being offset in time, has a much lower standard deviation when compared to valve opening than any other feature.

This indicates that the G-wave is not the best feature to use for accurately locating valve opening. As an example, the moment of valve opening can be estimated by adding a negative offset to the I-wave, or any feature associated with the I-wave or its integrals. This offset could be expressed as a fixed time interval, as a percentage of the heart rate period, or as a combination of both. When using the I-wave location, the combined total of this negative offset should be between 73 ms and 129 ms on a per subject basis (taking into account two standard deviations), based on the mean and standard deviation of the difference between the I-wave and valve opening.

The foot location on the bPPG was chosen to be the diastolic pulse transit time end point because it is the most prominent and well defined feature of the PPG. The true endpoint of the diastolic PTT is the PPG minimum, which is much less prominent and less consistent than the PPG foot. The average time difference between the bPPG foot and minimum is 35 ms. The diastolic pulse transit time is calculated from the moment of valve opening to the bPPG foot as shown in Figure 7.7. The aortic valve opening time is calculated from the BCG I-wave using a temporal offset.

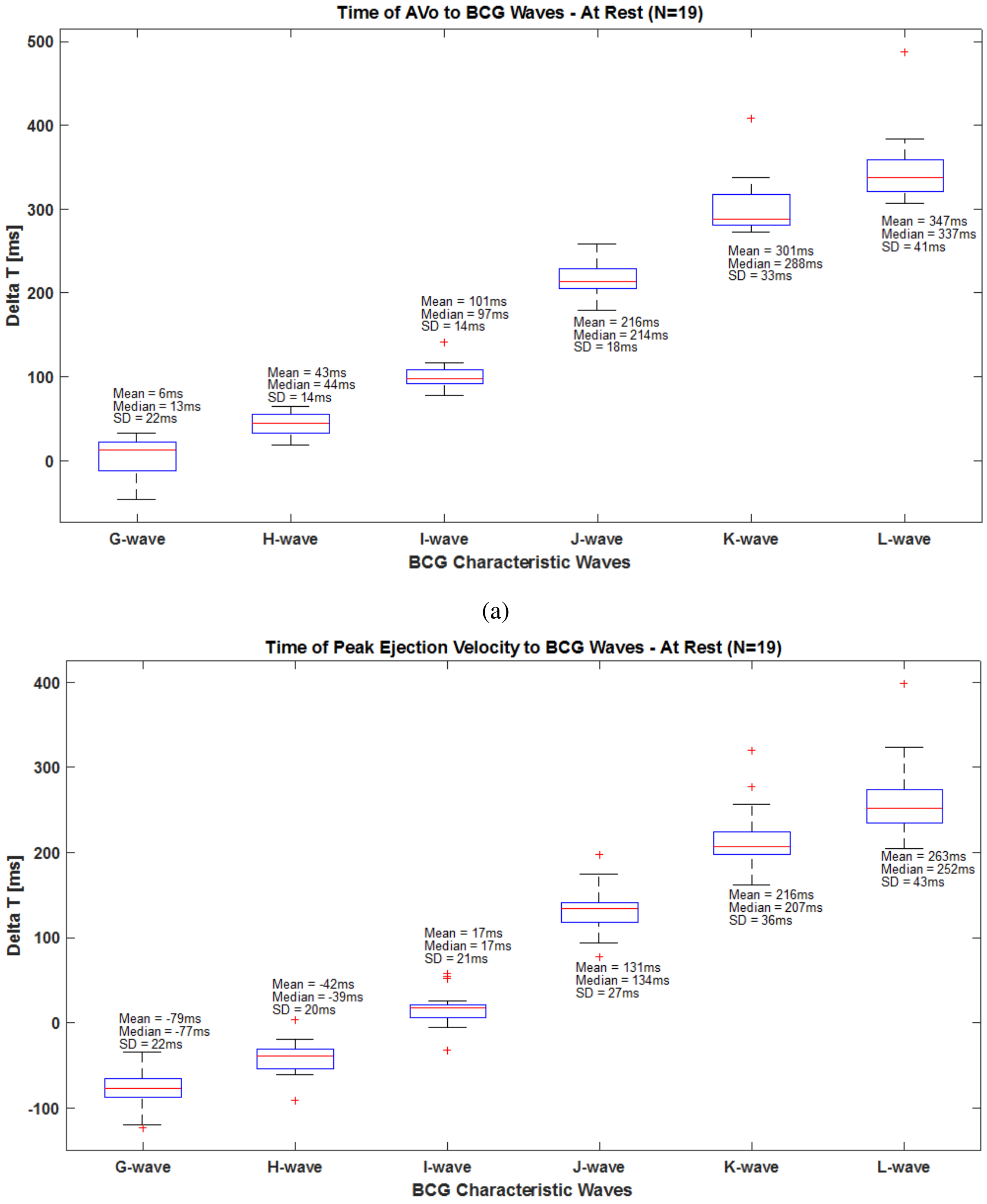

(a)

(b)

Figure 7.6: The timing difference from aortic valve opening (AVo) to each BCG wave indicates that the G-wave is the closest approximation, although the I-wave with a fixed temporal offset may yield a more consistent determination due to the smaller standard deviation of measure (a). The timing difference between the moment of peak ejection to each BCG wave indicates that the I-wave location is the closest in proximity to the moment of peak ejection velocity, with an offset of 17 ms (b).

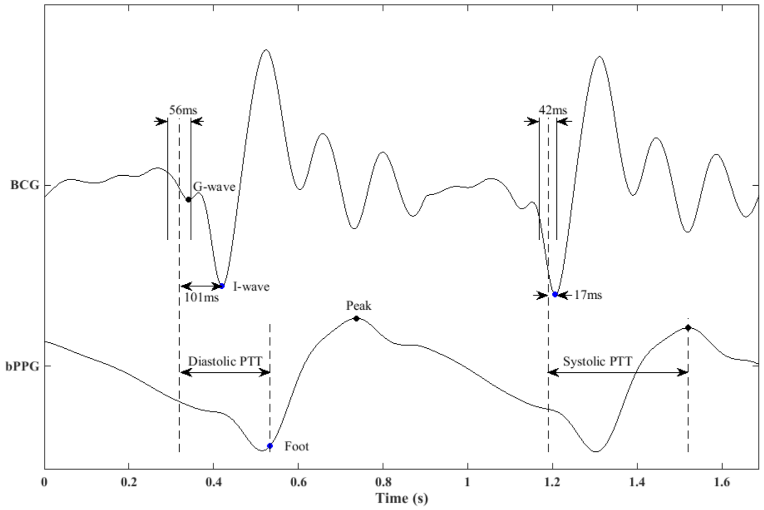

Figure 7.7: The start of the systolic and diastolic pulse transit times can be estimated by time shifting the I-wave appropriately. There is variability across patients when shifting from the I-wave. This variability can be reduced by integrating a time shift that is proportional to the HR period, or by choosing more prominent features.

7.3.4 BCG Features for Diastolic BP Estimate

An optimization based approach was used to explore BCG feature correlation with the moment of ventricular ejection as there is no definitive, temporally aligned feature for accurately estimating when this event occurs. The BCG measured by the FIT seat is proportional to acceleration, due to the sensor and measurement modality chosen. By taking the integral(s) of the BCG, other non-standard features relating to ejection velocity or displacement become apparent. The optimization algorithm determines the feature and associated time shift that best correlates with ventricular ejection.

Equation (7.2) is used to model diastolic PWV_p from two distinct features measured with the FIT seat. Flow velocity is zero for diastole, so it is not included in this equation, making PWV_m equivalent to PWV_p. The end point for the diastolic $PTT_{td,end}$ is the bPPG foot location, which is well defined and does not require a time shift. As of the potential starting features for $\mathrm{PTT}_{\mathrm{td,start}}$ require a time shift, two constants (c_0 and c_1) have been included to account for this time shift. Constant c_0 incorporates a percentage of the HR interval (T_{hr}) and c_1 incorporates a fixed time delay. It is important to have both a constant time shift (c_1) and one that is dependent on HR (c_0), since it is not clear how BCG feature locations change relative to HR variability.

$$\frac{x_a}{t_{d,end} - AVo} = PWV_{m,diastolic} = PWV_{p,diastolic} AVo = t_{d,start} + c_0 * T_{hr} + c_1 \tag{7.2}$$

Potential starting features ($\mathrm{T}_{\mathrm{d,start}}$) include the I-wave of the BCG, the trough of the first integral (velocity), the peak of the second integral (displacement), and the following zero crossing of the second integral (displacement). These features are shown in Figure 7.8, where a typical BCG waveform has been integrated to clearly show the potential PTT start location. For each end feature, the associated time shift is found using the optimization process, allowing the PTT to be calculated using the bPPG foot ($\mathrm{t}_{\mathrm{d,end}}$). The resultant PTT is converted to a PWV using the aortic length (x_{a}).

Optimization is performed in order to minimize the error of the estimation compared to the range of the three daily gold-standard measurements (BP). The optimization structure is shown in (7.3). The constants c_0 and c_1 are used to estimate valve opening (AVo), which in turn is used to estimate the diastolic pulse transit time and pulse wave velocity using the subject's aortic length. The resulting pulse wave velocity is used to calculate the estimated blood pressure ($\hat{BP}$) using the subject specific curve. Optimization is performed on each of the aforementioned features (t_{start}), resulting in constants for each, where constant c_0 is a percentage of the heart rate period (T_{RR}) and c_1 is a fixed offset.

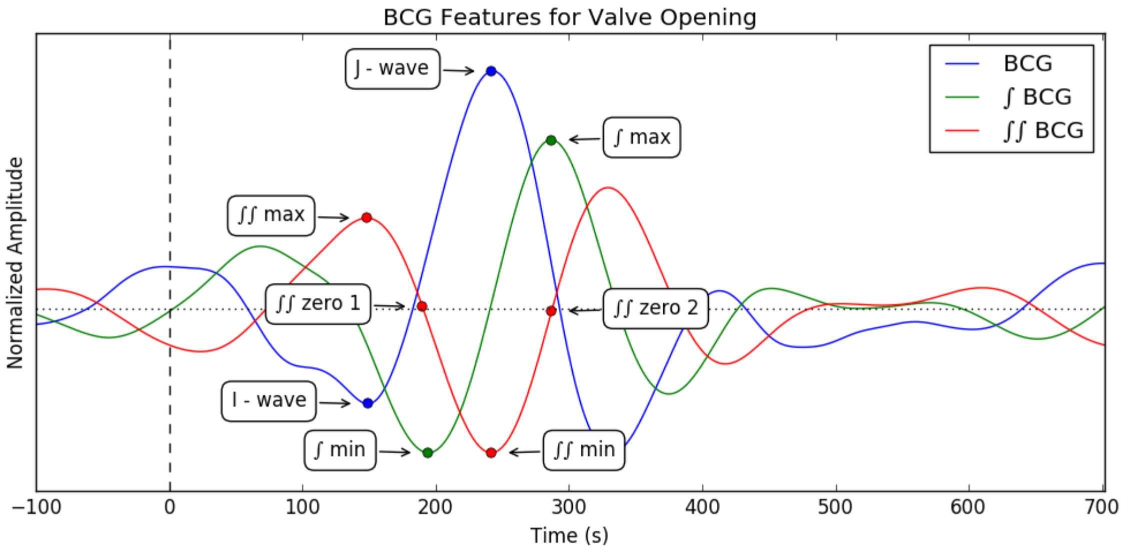

Figure 7.8: Eight different features are potential candidates for the starting point of the PTT. All of the potential features are related to the IJ complex and are on the BCG, the first integral of the BCG, or the second integral of the BCG. The feature that results in the best diastolic BP estimation is the first zero of the BCGs second integral ("$\iint$ zero 1").

$$
\begin{aligned}
&\operatorname*{argmin}_{c\in\mathbb{R}^2} E[f_e(\hat{BP}, BP)] \qquad \text{where} \\
&BP \in \mathbb{R}^3 \\
f_e(\hat{BP}, BP) = &\begin{cases} |\hat{BP} - \max(BP)| & \text{if } \hat{BP} > \max(BP) \\ |\hat{BP} - \min(BP)| & \text{if } \hat{BP} < \min(BP) \\ 0 & \text{otherwise} \end{cases} \\
PWV_m &= \frac{x_a}{t_{end} - AV_O} \\
AV_O &= t_{start} + c_0 * T_{HR} + c_1
\end{aligned}
\tag{7.3}
$$

The results from this optimization process indicate that the zero crossing of the second integral ("$\iint$ zero 1") is the feature which most consistently represents the moment of ventricular ejection. The matching constants, c_0 and c_1 are 5.1% of the HR period and 75 ms respectively. The average time shift can then be calculated by multiplying the average HR across all recordings by c_0 and adding the fixed offset from c_1. The resulting AVo timing as estimated by the optimization process can compared to the normative data valve opening AVo location, by taking into account the appropriate mean time shift for the normative data and the optimization based time shift. For each recording analyzed, 101 ms was subtracted from the I-wave location and used as the "normative mean AVo location". The AVo location as estimated from the zero crossing of the second integral is calculated using optimization based on the time shift of c_0 and c_1 and the average time shift between the bPPG minimum and foot. The difference between the "normative mean AVo location" and the optimization based location is then compared to the normative results in Figure 7.6. A mean difference of 3.8 ms was found between the normative data and the optimization based approach.

This is demonstrated in Figure 7.9, where the expected time shift range is shown in blue and the per-recording time shift range is shown in red. Additionally, this time shift is in line with what was extracted from the test subject's individualized calibration data (as compared to a synchronized echocardiogram), which showed a time shift of 103 ms, which is 2 ms different from the normative mean AVo timing. These points are shown as a green "x" in Figure 7.9. This partially validates the optimization based approach, where a custom time shift from a different feature results in a much more consistent estimate of aortic valve opening.

It was initially expected that the time shift associated with the chosen feature is not subject dependent, but would be fixed across a population. This has been tested across the normative data set, by utilizing the previously found constants. If this results in a low standard deviation error compared to the ultrasound based gold-standard, the constants can be considered globally valid on the normative population.

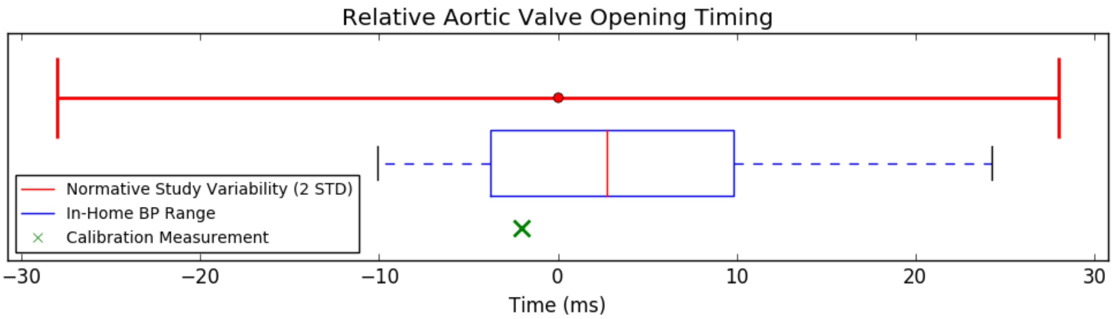

Figure 7.9: The estimate of aortic valve opening from the in-home study significantly improves upon the timing estimate for aortic valve opening across the normative population. This indicates that the resulting constants from the optimization based approach have a physical basis.

The results from these tests are shown in Table 7.4, where the resulting c_0 and c_1 from the 11-week optimization are utilized to estimate valve opening timing. The individual subject's timing captured during calibration using the ultrasound shows an error of 2 ms. The standard deviation for the entire normative population is 22 ms, while the standard deviation using a fixed offset from the I-wave is 14 ms. This indicates that the constants found for the previous subject are not valid across the normative population.

	Time Shift	**AVo Error**
11-Week BP Study	Optimized	10 ms (1-SD)
Echo Calibration	Optimized	2 ms (N=1)
Normative	Optimized	22 ms (1-SD)
Normative I-wave	Constant	14 ms (1-SD)

Table 7.4: Timing results across the normative population using the individualized constants from the 11-week trial, compared to the unoptimized I-wave timing.

Despite there being inherent measurement error in the AVo gold-standard, these results indicate that a per-subject time shift may be required to accurately estimate AVo. An alternative approach could utilize other timing intervals to calculate the time shift between each feature and AVo, resulting in a different model equation from that in (7.3).

7.3.5 Diastolic BP Estimate

Using the best feature ("$\iint$ zero 1") and associated constants, the resultant BP estimate shows excellent agreement with the cuff-based gold standard. The resultant BP estimates are compared to the gold-standard measurements in Figure 7.10. The darkest error bars represent the measured range (maximum and minimum) of the three BP cuff gold-standard values, without any error measurement error taken into account. On average, the diastolic BP estimate falls outside of the measured range by only 2.72 mmHg, which are well within the limits required by the AAMI standards organization [134].

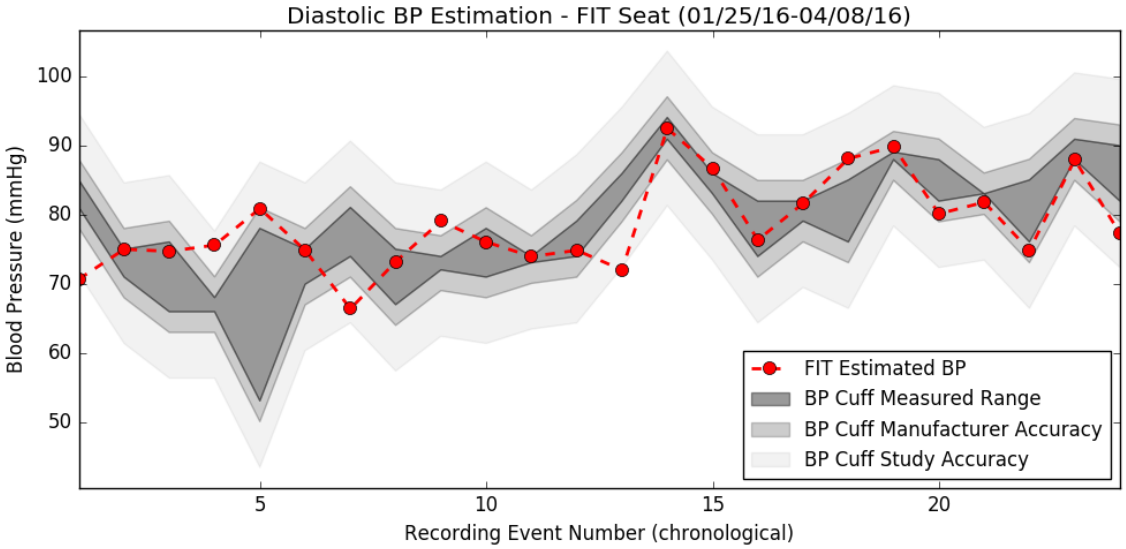

Figure 7.10: The diastolic BP estimate from the FIT seat accurately tracks trends in BP over the course of 6 weeks. The resulting accuracy is compared to the range of the gold standard measured using a commercial BP cuff. The errors in estimation are in line with what one would expect when accounting for the accuracy of the commercial BP cuff.

Blood pressure cuffs are notoriously inaccurate. The manufacturer quoted error for the BP cuff utilized was 2% or 3 mmHg, whichever is greater. A study where commercial BP cuff accuracy was compared to a hospital grade system was conducted at Ottawa Hospital in 2011 [135]. Across 210 clinical patients, blood pressure cuffs are off by more than 5 mmHg for 30% of the clinical patients [135]. This corresponds to a standard deviation of 4.8 mmHg. The mid-range error bars in Figure 7.10 incorporate the error quoted by the manufacturer of the BP cuff used by the subject. This is calculated by adding this error to the range of BP measurements. The lightest error bars are the measured values incorporating the error presented in the Ottowa Hospital study. This provides a reference for the type of accuracy that can be expected from devices currently used for in-home monitoring of BP.

7.3.6 Proposed Signal Processing Improvements

While signal processing algorithms can be continually improved, there are specific areas where improvement will directly improve the accuracy of BP estimation. This section outlines recommended area to focus on in future work, specifically ensemble averaging and signal quality algorithm improvements, with the goal of improving the temporal accuracy of features in the BCG and PPG.

Beat to beat variability between features introduces smearing in ensemble averaging. As an example, even though we know the bPPG foot can be used as the most robust end point for diastolic PTT, beat averaging still introduces smearing, which may introduce error in the timing extraction. This is illustrated in Figure 7.11, where the variability in the foot location is as high as 100 ms. The physiologic parameter or cause that can be attributed to these shifts is not known, unlike the shifts within the ECG. This variability may average out for a single recording, but the specific method of ensemble averaging impacts the location of each feature.

As such, ensemble averaging has a significant impact on estimating BP. Future work should investigate the best way to ensemble average both the bPPG and BCG, where the goal is

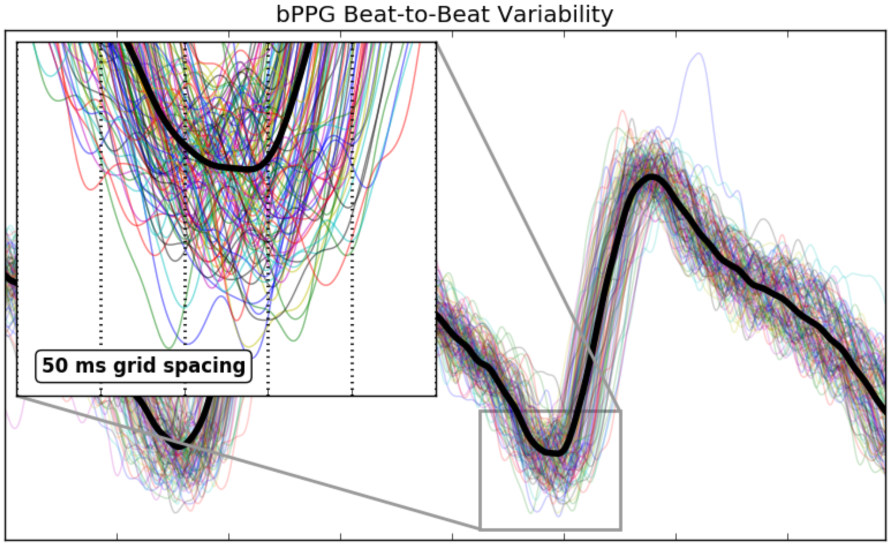

Figure 7.11: There is a large amount of beat-to-beat variability when ensemble averaging the bPPG relative to the R-wave peak. The PPG minimum and foot location can vary as much as 100 ms within a one minute recording. This introduces smearing in the ensemble averaged beat, potentially reducing the temporal accuracy of the feature.

to minimize feature smearing. Different types of beat resampling should be investigated, such as normalization to the RR-interval. Improved signal quality metrics for beat rejection will also have the potential to reduce feature smearing when ensemble averaging. This may include rejection criteria based on amplitude variations, and beat timing from preceding or subsequent beats.

With improved ensemble averaging techniques, the location and prominence of specific features may change. The surrogate features currently used when estimating BP may be replaced with features that are directly related to key physiologic events. As an example, the features (G-wave) closest in proximity to valve opening is currently non-distinct. With improved signal processing methods, the direct use of the G-wave or other more robust features may be possible.

7.4 BCG Amplitude and Cardiac Function

7.4.1 Methods

There are many ways to assess ventricular systolic contraction and cardiac function (e.g. LV stroke volume, stroke rate, strain, strain rate, among others). The rate of ventricular systolic ejection can be measured by using the product of the velocity of blood flow in left ventricular outflow tract (LVOT) and its area. The LVOT velocity is measured with pulsed wave Doppler ultrasound (Figure 7.12-(a)) and the LVOT area is estimated using the formula for a circle and the measured diameter (Figure 7.12-(b)). In the example shown, the LVOT diameter is 1.1 cm and the LVOT peak velocity is 100 cm/s, which yields a peak stroke rate of 346 cc/s.

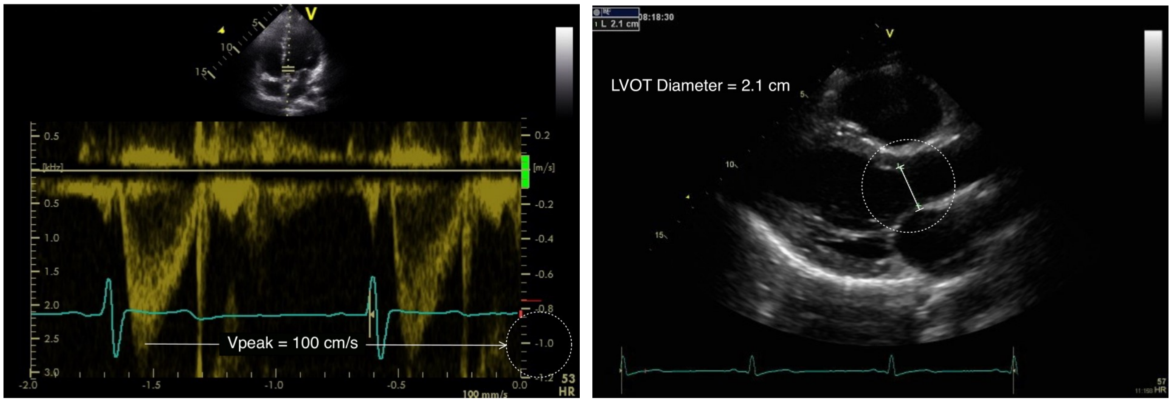

(a) (b)

Figure 7.12: An example Doppler ultrasound capture used to measure the LVOT velocity (a). This measure, combined with the LVOT diameter (b) can be used to calculate stroke rate. Courtesy of Karl Q. Schwarz, MD.

As the BCG is a measure of the mechanical activity of the heart, it is believed that the IJ amplitude has a correlation to stroke rate. This hypothesis will be validated by determining the IJ amplitude using the delineation algorithms described in Chapter 4 across all normative subjects. The ultrasound measure with the highest linear correlation will be presented.

7.4.2 Results and Discussion

The correlation between IJ amplitude and cardiac function is highlighted in Figure 7.13, where the rest and post-stress ensemble averaged BCG waveform is shown for a single subject.

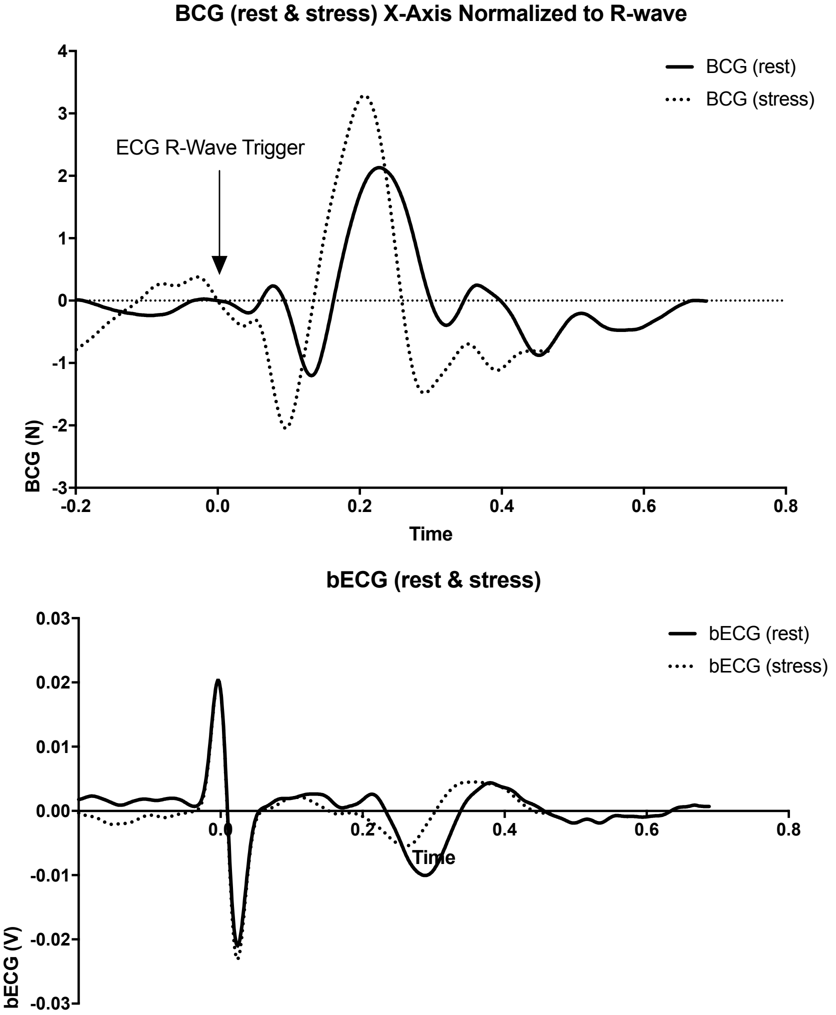

Figure 7.13: For a single subject, the BCG morphology remains consistent at both rest and post-stress. At post-stress, the IJK complex has been shifted towards the R-wave and the IJK amplitude has been significantly increase when compared to the rest ensemble average. The time axis (in seconds) is the same for both rest and stress. Courtesy of Karl Q. Schwarz, MD.

The correlation between ventricular systolic contraction is compared to the BCG using

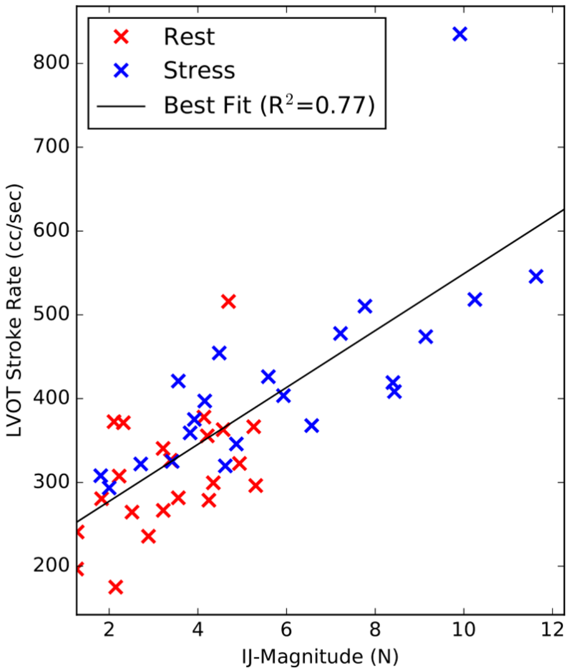

Figure 7.14: The correlation of BCG amplitude measures to stroke rate is shown for both rest and post stress. This measure has a very high linear correlation to the echocardiogram gold standard. The stroke rate has an R-value of 0.77 compared to the magnitude of the IJ-wave in the FIT BCG.

the rate of ventricular systolic ejection (stroke rate), shown in Figure 7.14-(a). There is a clear and distinct correlation between the magnitude of the BCG's first integral and the stroke rate. The stress data points are clustered at the higher range of both measures, indicating that the FIT seat is capable of discerning between physiologic states using the BCG. Heart failure echocardiogram analysis must be completed manually by a cardiologist due to abnormal BCG morphologies present in the heart failure population. However, it is expected that the HF results will be clustered closer to the origin due to the lower cardiac output and poor cardiac function of these subjects.

By looking at the IJ amplitude for three distinct groups of cardiac function, low (HF), normal (normative at rest), high (normative post-stress), a clear and statistically significant distinction can be made between each. This is shown in Figure 7.15. This highlights the ability of the BCG to differentiate between levels of cardiac function.

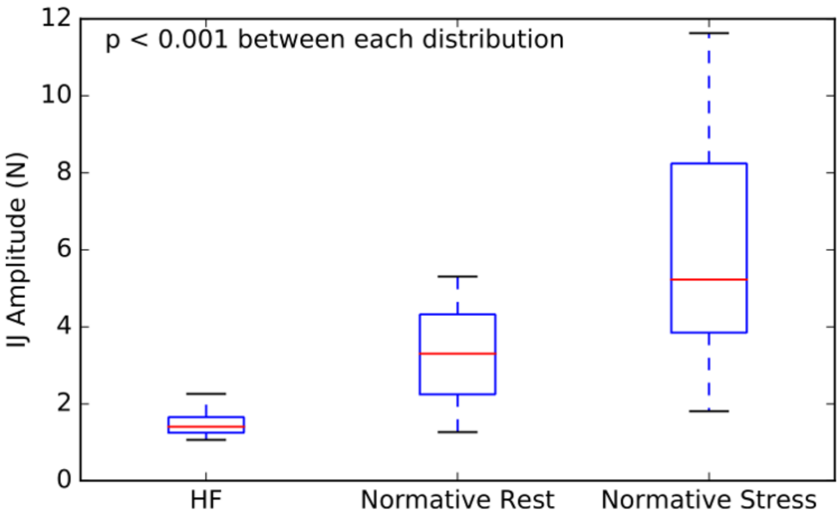

Figure 7.15: The IJ amplitude of the low (HF), normal (normative at rest), high (normative post-stress) groups of cardiac function have statistically significant differences. This demonstrates the ability of the FIT seat to differentiate between these groups.

7.5 Conclusion

The FIT seat can accurately measure diastolic blood pressure trends across time for a calibrated subject. An optimization based approach was utilized to find the optimal features for estimating pulse transit time. The estimated pulse transit time is converted to a pulse wave velocity using the aortic length, allowing direct BP estimation through a physics based model and a single ultrasound based calibration. Using FIT only measurements for six weeks, the estimated diastolic BP has an error of 2.72 mmHg on average when compared to an off the shelf BP cuff. The approach described herein did not successfully estimate systolic BP, however, it is believed that the BCG may be capable of estimating flow velocity, enabling accurate systolic BP estimation. This should be investigated through future human subject testing, designed specifically for the validation of blood pressure based approaches.

The bPPG delineation algorithm, which was validated in Chapter 4, demonstrates robust foot extractions from the normative and HF population. Additionally, the variability of different BCG features relative to key cardiac timing intervals has been demonstrated across normative subjects. These results enable the accurate extraction of diastolic blood pressure across subjects using a per-subject physics based calibration using the FIT seat. As such, the FIT seat is the first device to demonstrate blood pressure estimation across long periods of time without needing continual recalibration.

Chapter 8

Sub-Nyquist Compressed Sensing

8.1 Introduction

The work presented in this chapter demonstrates sub-Nyquist sampling of the photoplethysmogram (PPG) on custom hardware. The purpose of this work is to significantly reduce the power consumption of the PPG, which is the device that is responsible for the largest percent of power consumption compared to other medical instrumentation in the FIT seat. Existing sub-Nyquist techniques based on compressed sensing to reduce power consumption are not ideal for signals such as the photoplethysmogram, which require an energy source to generate the signal. By directly generating the compressed sensing measurement vector, the sampling and measurement stages can be combined, which allows the signal to be truly under-sampled. A novel system for the direct generation of the measurement vector ia proposed.

A custom photoplethysmogram analog-front-end is used to quantitatively demonstrate a significant reduction in power consumption using the methods presented herein. Furthermore, physiological signals often contain a characteristic spectrum, allowing the use of additional *a priori* information to create a weighting vector that can be used during reconstruction. This allows for a reduction in the number of measurements needed to accurately reconstruct the signal, which further reducing power consumption. These methods are tested across a range of subjects and physiological states to demonstrate robustness. An error rate of less than 3% for the normalized root mean square deviation, root mean square error, and temporal accuracy was achieved with an average sample rate one-tenth the Nyquist rate. Results show an overall decrease in power consumption by 83.5% for a custom photoplethysmogram analog-front-end, when sampling at one-tenth the Nyquist rate.

8.2 Background

Compressed sensing is the process of reconstructing a sparse signal from a small number of measurements[136, 137, 138, 139, 140]. It has been used in the past to reduce the power consumption of wireless transmission in medical devices [141, 142], but it has not been effective in reducing the power consumption that is associated with the analog-front-end during data collection. Classically, compressed sensing does not reduce the number of samples required, but rather reduces the number of measurements needed to reconstruct the original signal [143]. These measurements are generated from the Nyquist sample vector using a random sensing matrix. In essence, this is real-time block compression.

If the number of samples needed can be reduced, the PPG can see a significant improvement in power consumption. This can be done by using an identity based sensing matrix to combine the sampling and measurement stages. The identity based sensing matrix is structured so that matrix multiplication is not required when generating the measurement vector. By generating the measurement vector directly, rather than from a Nyquist based sample vector, a signal can be sampled at a rate less than Nyquist.

There have been many recent key advances in analog compressed sensing, but reducing the power consumption of the PPG requires a different approach. The digital to information converters presented in [144, 145, 146, 147] require the analog signal to be continuously present, so that it can be modulated at, or above, the Nyquist rate. The goal when using compressed sensing of the PPG is to reduce the on-time of the LED light source, which is not possible if the PPG signal needs to be modulated at or above the Nyquist rate.

The aforementioned digital to information converters and the analog compressed sensing method presented in [148] are very complex. For every compressed sensing measurement taken, separate analog modulation circuitry is required. This must be duplicated for every channel being measured, since the analog signal cannot be multiplexed. This makes scaling up to a large number of channels impractical.

It has been shown that compressed sensing can be used on a variety of physiological signals, including the ECG [149, 150, 151, 152, 153], the EMG [142], the EEG [154, 155], and the PPG [156, 157]. These physiological signals tend to have a characteristic frequency spectrum, which allow a weighting vector to be created from the use of additional *a priori* information.

The work presented in [156] and [157] originally proposed the use of weighted reconstruction and an identity based sensing matrix for sub-Nyquist sampling of the PPG. In this work we demonstrate this in a hardware platform and quantify the performance at different sub-Nyquist sampling rates across subject populations and physiological states. This effectively combines the sampling and measurement stages of compressed sensing in a custom PPG analog-front-end.

The identity based sensing matrix can be used on any signal that can be compressively sensed and that is sparse in the frequency domain, and weighted reconstruction can be used on any signal that contains a characteristic spectrum. In this work, the PPG signal was used to quantitatively evaluate both methods. Since PPG power is dominated by the illumination source [158, 159], this also served as a platform to evaluate potential power consumption reduction using these techniques.

Both a commercial PPG and a custom PPG analog-front-end (AFE) are used for testing the methods presented herein. The accuracy of these methods are tested across multiple subjects and physiological states using the commercial PPG. True sub-Nyquist sampling and the associated power savings is demonstrated with the custom hardware implementation.

8.3 Compressed Sensing Theory

8.3.1 Generating the Measurement Vector

The Nyquist-Shannon sampling theorem states that a signal must be sampled at a rate twice the maximum frequency of the signal being sampled for it to be perfectly reproduced [160]. However, sampling at the Nyquist rate is inefficient for signals that contain a relatively small amount of information with respect to their bandwidth.

The result from uniformly sampling a signal at the Nyquist rate is an N dimensional sample vector, $\vec{\mathbf{x}} \in \mathbb{R}^N$. In classic compressed sensing, the measurement vector $\vec{\mathbf{y}} \in \mathbb{R}^M$ is determined by multiplying the Nyquist sample vector with a sensing matrix ($\mathbf{A} \in \mathbb{R}^{M \times N}$) [137, 138], as shown in (8.1).

$$\mathbf{A}\vec{\mathbf{x}} = \vec{\mathbf{y}} \tag{8.1}$$

In compressed sensing, the number of measurements is much less than the number of Nyquist samples in the sample vector ($M \ll N$). This creates an under-determined linear system, which is then used as a constraint during reconstruction. The method originally proposed by Candes and Donoho uses ℓ_1 minimization (convex optimization) to reconstruct the original signal, $\hat{\mathbf{x}}$ [137, 138], as shown in 8.2.

$$\min_{\hat{\mathbf{x}} \in \mathbb{R}^N} \|\Psi \hat{\mathbf{x}}\|_1 \text{ subject to } \vec{\mathbf{y}} = \mathbf{A}\hat{\mathbf{x}}, \tag{8.2}$$

Successful compressed sensing, where $\hat{\mathbf{x}}$ approximates $\vec{\mathbf{x}}$, requires the original signal to be sparse in at least one domain, where sparsity is defined as the percentage of non-zero coefficients in $\vec{\mathbf{s}}$ of the sparse domain. This definition is relaxed when dealing with signals that contain noise; sparsity is then defined as the percentage of non-negligible coefficients [143]. The sparse domain coefficients $\vec{\mathbf{s}} \in \mathbb{R}^N$ are found by multiplying $\vec{\mathbf{x}}$ with the matrix transform $\Psi \in \mathbb{R}^{N \times N}$. An example of a sparse signal is shown in Figure 8.1, where the PPG is shown to be sparse in the discrete Fourier domain.

If the sparsity level is known, one can estimate the minimum number of measurements

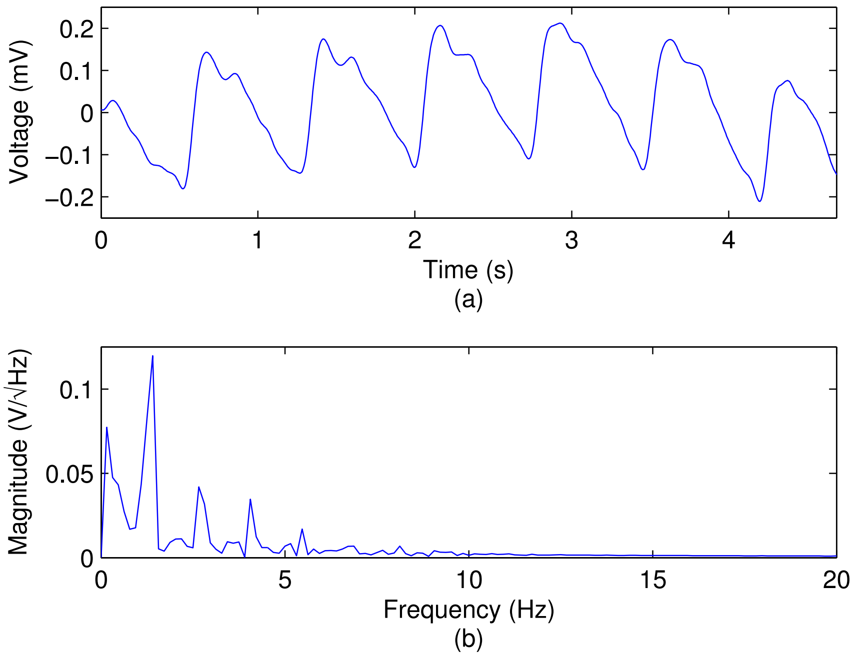

Figure 8.1: A short PPG clip (a) and its discrete Fourier transform (b) are shown.

M needed to accurately reproduce $\vec{\mathbf{x}}$ from the number of samples (N) and number of non-negligible coefficients (K) [143]. The lower bound for the number of measurements needed to represent the signal is shown in (8.3).

$$M \geq O\left(Klog(\frac{N}{K})\right) \tag{8.3}$$

The size of the sensing matrix ($M \times N$) is based on the number of measurements needed. This matrix must be incoherent to the domain in which the signal is sparse [143, 137]. Coherence is defined as the maximum correlation between elements in two matrices; in this case, $\mathbf{A}$ and Ψ. In other words, each row in $\mathbf{A}$ must be spread out in the sparse domain, allowing the maximum information to be captured from $\vec{\mathbf{x}}$. It has been shown that by using normal, uniform, or symmetric Bernoulli distributions to populate $\mathbf{A}$, it will be incoherent to Ψ with an overwhelming probability [143, 161].

When **A** is populated with a random distribution, all of the samples in $\vec{\mathbf{x}}$ are used to determine $\vec{\mathbf{y}}$. Such a sensing matrix would require all the digital values to have been previously sampled at the Nyquist rate. This can result in power savings for a system that simply needs to compress data before storage or transmission, but in applications where the act of capturing data requires a large amount of energy or resources, a different approach must be taken.

Given that only M measurements are required to represent $\vec{\mathbf{x}}$, only M samples should be needed for accurate reconstruction. By creating the measurement vector directly from the analog signal, only M samples are used, making Nyquist sampling unnecessary. This is illustrated in Figure 8.2 where the analog signal is randomly sampled, directly populating the measurement vector. This is compared to classic compressed sensing, which requires a sensing matrix to generate the measurement vector.

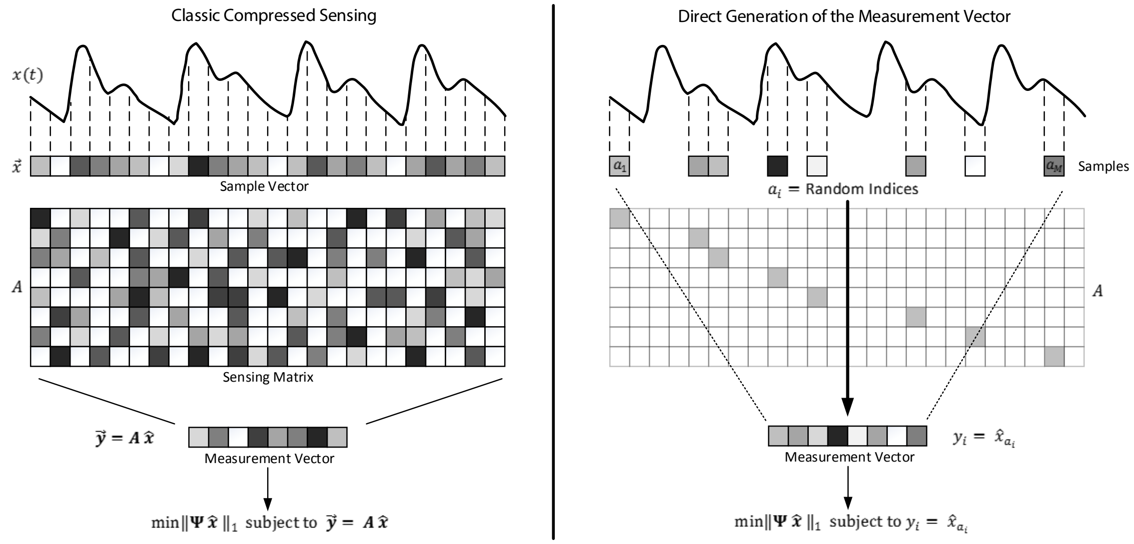

Figure 8.2: Classic compressed sensing creates the measurement vector from the Nyquist based sample vector and a sensing matrix. The sensing matrix is often random, requiring every Nyquist sample to be used and resulting in large matrix multiplication on the sensor node. By directly generating the measurement vector, the sensing matrix is removed from the compressed sensing paradigm. Not only does this simplify the sensor node, but it also allows for true sub-Nyquist sampling.

When generating the measurement vector directly, the notation shown in (8.4) can be used to reconstruct the desired signal. This results in the removal of the sensing matrix from the compressed sensing paradigm. In Figure 8.2 and (8.4), the vector $\hat{\mathbf{a}} \in \mathbb{R}^M$ contain random indices, so that each i-th value of $\hat{\mathbf{x}}$ is equal to the a_i-th value of $\vec{\mathbf{y}}$.

$$\min_{\hat{\mathbf{x}} \in \mathbb{R}^N} \|\Psi \hat{\mathbf{x}}\|_1 \text{ subject to } \vec{\mathbf{y}}_{\mathbf{i}} = \hat{\mathbf{x}}_{\mathbf{a_i}} \tag{8.4}$$

Given that a sensing matrix is still required for many forms of reconstruction, it is desirable to construct a sensing matrix that exactly represents the process of directly generating the measurement vector. Such a sensing matrix is created from an identity matrix, which is an orthogonal set of impulse functions. The process used for this is shown in (8.5), where $(N - M)$ random rows are removed from an identity matrix of size N to create $\mathbf{A}$.

$$\mathbf{A} = \begin{bmatrix} 1 & 0 & 0 & 0 & 0 & 0 \\ \cancel{0} & \cancel{1} & \cancel{0} & \cancel{0} & \cancel{0} & \cancel{0} \\ \cancel{0} & \cancel{0} & \cancel{1} & \cancel{0} & \cancel{0} & \cancel{0} \\ 0 & 0 & 0 & 1 & 0 & 0 \\ \cancel{0} & \cancel{0} & \cancel{0} & \cancel{0} & \cancel{1} & \cancel{0} \\ 0 & 0 & 0 & 0 & 0 & 1 \end{bmatrix} = \begin{bmatrix} 1 & 0 & 0 & 0 & 0 & 0 \\ 0 & 0 & 0 & 1 & 0 & 0 \\ 0 & 0 & 0 & 0 & 0 & 1 \end{bmatrix} \tag{8.5}$$

Previous research has shown that limited quantization and the use of structured matrices do not negatively impact reconstruction accuracy [150, 161, 142]. An identity based sensing matrix allows only one sample to be captured for each measurement needed, taking quantization and matrix structuring to their extremes.

Candes alludes to this method during a very important example when discussing incoherence [143], and Baheti proposes the use of impulse basis functions when constructing the sensing matrix [156, 157]. Their work shows that impulse functions are maximal incoherence to sinusoidal basis functions, such as those used in the Fourier domain. The methods presented herein improve upon this notion of using impulse basis functions by combining the sampling and measurement stages, as shown in Figure 8.2, and by demonstrating that the PPG can successfully be sampled at a rate less than Nyquist in custom hardware.

8.3.2 Weighted Reconstruction Using a Characteristic Spectrum

Compressed sensing theory states that the sparsity of the signal directly impacts the accuracy of reconstruction [138, 137]. Signal reconstruction is the process of finding the sparsest signal which adheres to the constraints imposed during measurement. The constraints typically used are from the under-determined linear system formed by the sample vector, measurement vector, and sensing matrix. Reconstruction is typically done by minimizing the ℓ_1 norm of the coefficients for the domain in which the signal is sparse. This type of convex optimization is shown in (8.2).

Other variations of this approach assume that a small measurement error is present, allowing for more robust reconstruction when the measurement vector's sparsity is affected by noise [162, 163]. Given that there exists many ways to solve this minimization problem, Dixon has completed a comparison of multiple techniques, including different types of convex optimization and greedy algorithms such as matching pursuit [162]. Their work has shown that although convex optimization is not the fastest method for reconstruction, it reliably provides accurate results.

Weighted reconstruction changes classic reconstruction by allowing a less sparse, but a more accurate signal to be chosen. The weighting vector is calculated in (8.6) using the characteristic spectrum $\bar{\mathbf{s}}$ of the signal, and the constant σ, which restricts the maximum possible value of the weighting vector. When a coefficient in the characteristic spectrum is zero, the maximum weighting becomes $1/\sigma$. For the work presented herein, $\sigma = 16$ is used.

$$[w]_i = \frac{1}{[\bar{s}]_i + \sigma} \qquad i = 0, 1, \cdots, N-1 \tag{8.6}$$

The coefficients of the reconstructed signal's sparse domain are scaled by the weighting vector during the optimization process in (8.7), placing a higher priority on the coefficients that are known to characterize the given physiological signal. This is done by minimizing the pointwise product of the weighting vector and the sparse coefficients.

$$\min_{\hat{\mathbf{x}} \in \mathbb{R}^N} \| \langle \vec{\mathbf{w}}, (\Psi \hat{\mathbf{x}}) \rangle \|_1 \text{ subject to } \vec{\mathbf{y}} = \mathbf{A}\hat{\mathbf{x}}, \tag{8.7}$$

The weighting vector effectively decreases the sparsity of non-characteristic signals by significantly increasing the coefficients which are not characteristic. This allows a reconstructed waveform to be chosen that will more accurately represent a given signal, despite the fact that it may be less sparse than other solutions. Many types of compressed sensing reconstruction (e.g. greedy algorithms) search for the sparest solution. For this reason, the weighting vector can be easily integrated into most compressed sensing reconstruction methods by modifying the sparse vector.

8.4 Methods

The identity based sensing matrix and weighted reconstruction are both tested in two separate phases. The first phase uses a commercial system to test robustness across subjects and varying physiological states, while the second phase uses a custom hardware implementation to measure the achievable power savings when compared to standard Nyquist based sampling. Each phase utilizes the same error metrics to benchmark the reconstruction accuracy. For all the tests presented herein, the Fourier domain was used as the sparse domain for the PPG.

8.4.1 Testing Across Subjects and Physiological States

The physiological data sets used were obtained under informed consent in a protocol approved by the Rochester Institute of Technology Institutional Review Board for Protection of Human Subjects. The Biopac MP36 (Biopack Systems, Inc., Goleta, CA) was used to capture synchronized ECG and ear PPG from six test subjects at a sample rate of 50 kHz [164, 165]. One minute measurements were captured at six different physiological states for each subject. These physiological states include the subject at rest while sitting, standing, and supine in addition to three activity levels that were varied using a recumbent bike.

To ascertain the reliability of these approaches across subjects and physiological states, each metric's average and standard deviation is calculated across six physiological states for each subject. The weighted reconstruction is compared to classic non-weighted reconstruction and the identity based sensing matrix is compared to the standard random

Gaussian sensing matrix. The comparisons are made using the error metrics discussed in Section 8.4.3.

In order to match the Nyquist sampling rate used in the custom hardware compressed sensing implementation, each one minute recording is decimated to a sample rate of 170 Hz. Each recording is tested at an undersampling ratio (USR) of 5, 10, 15, and, 20 with a vector size $N = 2040$, corresponding to a window size of 12 seconds. A single identity based sensing matrix and a single Gaussian based sensing matrix were used across all subjects and physiological states.

8.4.2 Direct Generation of the Measurement Vector in Hardware

In order to have complete control of the signal acquisition process, a custom PPG analog front end (AFE) was built. The physical implementation uses off-the-shelf components and consists of the AFE, a TI MSP430 microcontroller, power management, and a wireless module. The schematic used for the custom AFE is the same as shown in Figure 3.7.

The AFE consists of a photodiode, a transimpedance amplifier, and an amplification stage. The differential amplifier uses a DC reference to actively remove the DC offset from the output of the transimpedance amplifier. The DC reference is generated using the MSP430 by averaging samples measured from the output of the transimpedance amplifier. This DC value is only measured when the PPG is sampled, so that additional samples are not needed when directly generating the measurement vector.

The light source for the PPG consists of a red LED that is pulsed when a sample is acquired. The Nyquist sampling rate used herein is 170 Hz. The LED on-time is 0.99 ms for each sample, which corresponds to a duty cycle of 16.9%. Modern ultra-low power devices such as the integrated Analog Front-End from Texas Instruments (AFE4490) has a programmable duty cycle from 1-25%, with a typical duty cycle of 5% [166].

When the measurement vector is generated directly, there is no Nyquist sample vector for which to compare the reconstruction. In order to benchmark the sub-Nyquist sampled signals, 5 parallel ADC channels are used, one for the Nyquist rate and one for each USR being tested.

A total of 12 files, consisting of 18 minutes of PPG data were captured from a single subject at a sample rate of 170 Hz for verifying the custom AFE. The USRs and identity matrix used for reconstruction was the same as when testing across subjects and physiological states.

When measuring the AFE's power consumption and generating the measurement vector directly, separate vectors need to be captured for each USR. At a USR of 5, 10, 15, and 20, three measurement samples containing a total of four minutes of PPG data were captured from a single subject at rest within one hour. The AFE and LED currents were measured during each of these captures and then averaged to determine the corresponding power consumption for each USR.

8.4.3 Error Metrics

The overall signal quality is tested by using the NRMSD, shown in (8.8). This essentially measures the normalized RMS of the error signal between the reconstructed PPG and the original PPG.

$$NRMSD = \frac{\sqrt{E[(\vec{\mathbf{x}} - \hat{\mathbf{x}})^2]}}{(\vec{\mathbf{x}}_{max} - \vec{\mathbf{x}}_{min})} \tag{8.8}$$

The percent change in a signals RMS is used to determine how reconstruction errors affect the estimated SpO_2 levels. The percent difference between the RMS of the reconstructed vector and the original sample vector is calculated using (8.9). This is a normalized metric for showing how the RMS of the entire signal has changed.

$$RMS_{diff} = \frac{|RMS(\vec{\mathbf{x}}) - RMS(\hat{\mathbf{x}})|}{RMS(\vec{\mathbf{x}})} \tag{8.9}$$

The PPG foot represents the start of a single heartbeat [167]. The error in foot location is defined as the temporal difference between the reconstructed foot location and Nyquist foot location, shown in (8.10).

$$\Delta_{foot} = |t_{foot_{\vec{\mathbf{x}}}} - t_{foot_{\hat{\mathbf{x}}}}| \tag{8.10}$$

The wavelet transform derivative delineation (WTDD) algorithm presented in [165], was used to locate the foot in each PPG beat. The WTDD algorithm consists of two phases. The first phase locates the valid range for each beat, also known as beat segmentation. The valid range for the PPG foot is found using the wavelet transform (WT) in combination with a simple moving average window filter. The WT is implemented as a cascaded set of FIR filters. The second phase uses the valid range and the first three derivatives of the PPG signal to determine the foot location. The derivatives are calculated using FIR filters. This algorithm has been shown to be reliable and robust across subjects and physiological states.

8.5 Results and Discussion

8.5.1 Robust Reconstruction

The results shown in Figure 8.3 (left) compares weighted reconstruction to classic ℓ_1 reconstruction across subjects and physiological states. These results show that weighted reconstruction performs significantly better than non-weighted reconstruction, reducing both the overall error rate and the variation of the error for each error metric. This demonstrates that higher USRs can be used with weighted reconstruction while maintaining a given target accuracy, further increasing the usefulness of compressed sensing.

Weighted reconstruction does not add any complexity to the reconstruction system, therefore, it is very easy to implement. Only one additional vector multiplication is needed each time the ℓ_1 norm of the sparse domain is calculated. Existing systems do not need to be physically modified to utilize weighted reconstruction as it requires no changes be made to the sensor node, since the weighting vector is only used during reconstruction.

Furthermore, these results show that a single weighting vector can be used across a range of subjects and physiological states to increase the accuracy of the PPG. The characteristic spectrum never needs to be reprogrammed or updated since it is not something that is subject specific, it is specific to the physiological signal being measured.

Given that the identity based sensing matrix allows for fewer samples to be used when gen-

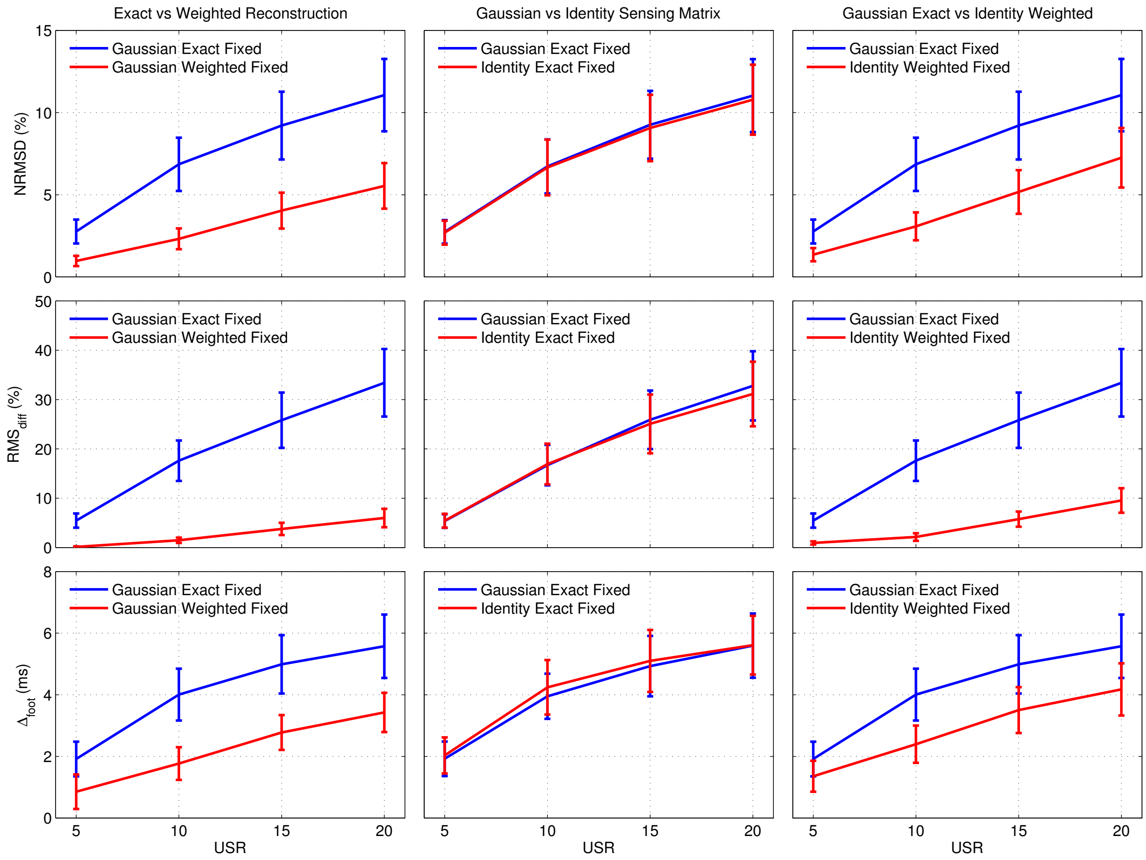

Figure 8.3: Classic exact reconstruction is compared to weighted reconstruction (left) across a wide range of USRs, subjects, and physiological states. Similarly, the identity based sensing matrix is compared to the random Gaussian sensing matrix (center). Finally, both weighted reconstruction and the identity based sensing matrix are compared to classic compressed sensing (right) using exact ℓ_1 reconstruction and a Guassian matrix. These results show that the identity based sensing matrix does not have any negative impact on reconstruction accuracy when compared to a Gaussian based sensing matrix and that weighted reconstruction significantly improves upon classic ℓ_1 exact reconstruction.

erating the measurement vector, it must be shown not to reduce accuracy when compared to the standard Gaussian based identity matrix. This is demonstrated by the comparison between the identity based and a Gaussian based sensing matrix in Figure 8.3 (center). These results show that there is no discernible difference between the accuracy of the Gaussian matrix and the identity based sensing matrix for the NRMSD, the RMS error, and the foot error.

The magnitude of the variance for each metric has also not increased, showing that robustness has not been reduced when using an identity based sensing matrix. This demonstrates that this sensing matrix can be used without any negative impact on reconstruction accuracy. Therefore, the measurement vector can be directly generated.

The results when using both weighted reconstruction and the identity based sensing matrix are compared to standard compressed sensing in Figure 8.3 (right). The overall error rate is reduced and the variance of the error is reduced when using both the identity based sensing matrix and weighted reconstruction. Compared to classic compressed sensing utilizing a Gaussian sensing matrix and ℓ_1 reconstruction, each metric shows a significant decrease in error.

These results have quantitatively demonstrated the validity of both the identity based sensing matrix and weighted reconstruction within the existing compressed sensing framework across subjects and physiological state.

8.5.2 Hardware Validation Using the Identity Based Sensing Matrix

A comparison of truly sub-Nyquist sampled PPG waveforms captured at different average sample rates, is shown in Figure 8.4. As the USR increases, additional extrema appear within the frequency range of interest and slope deformations start to become apparent. At an average sample rate of 8.5 Hz (USR = 20), the waveform extrema are both exaggerated and attenuated. This results in an overall decrease in signal accuracy.

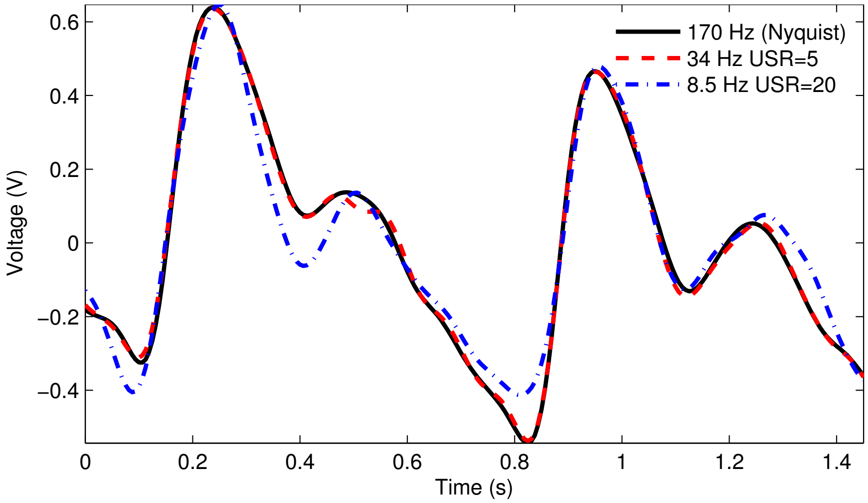

Figure 8.4: As the USR increases, the reconstructed signal becomes deformed. This deformation results in non-smooth slopes and elongated extrema.

The results when using both the identity based sensing matrix and weighted reconstruction on the custom hardware are shown in Table 1. These results are generated by comparing each simultaneously sub-sampled PPG signal to the Nyquist sampled PPG signal, as described in 8.4.2. This is done so that the weighted reconstruction and sub-sampling can be benchmarked using the error metrics shown in Section 8.4.3.

These results show similar error rates to the commercial hardware used in Section 8.5.1. This verifies that the hardware works as expected so that it can be used to demonstrate the possible power savings when directly generating the measurement vector.

USR	**NRMSD**	**RMS**$_{\mathbf{diff}}$	$\blacksquare_{\mathbf{foot}}$
5	2.18%	1.20%	2.79 ms
10	4.09%	3.79%	3.49 ms
15	6.05%	7.89%	4.07 ms
20	8.20%	13.14%	4.25 ms

Table 8.1: Reconstruction Results with Custom Hardware

8.5.3 Significant Power Reduction with Sub-Nyquist Sampling

When sub-Nyquist sampling a single PPG channel, there is a drastic reduction in power consumption. This is shown in Figure 8.5. These results show a continued decrease in power consumption as the average sample rate decreases. At an average sample rate of 11 Hz, the power consumption is reduced by 86.7%, which closely matches the theoretical power reduction of 87.7%. This corresponds to a very significant 7.5-fold increase in battery life.

The theoretical power consumption is calculated using the analog front end's quiescent power, which was measured to be 1.5 mW. The difference between the current consumption at Nyquist and the quiescent power will be scaled by the USR. The reduction in power consumption asymptotically approaches the circuit's quiescent power, as can be seen by the results shown in Figure 8.5, where the theoretical reduction in power is compared to the actual observed power consumption.

Devices with a lower quiescent power will see a more effective reduction in power consumption for lower average sample rates. Using advanced PPG designs or commercial devices such as those in [159, 166, 168], will show similar reductions in power based on the Nyquist and quiescent power consumption when generating the measurement vector directly.

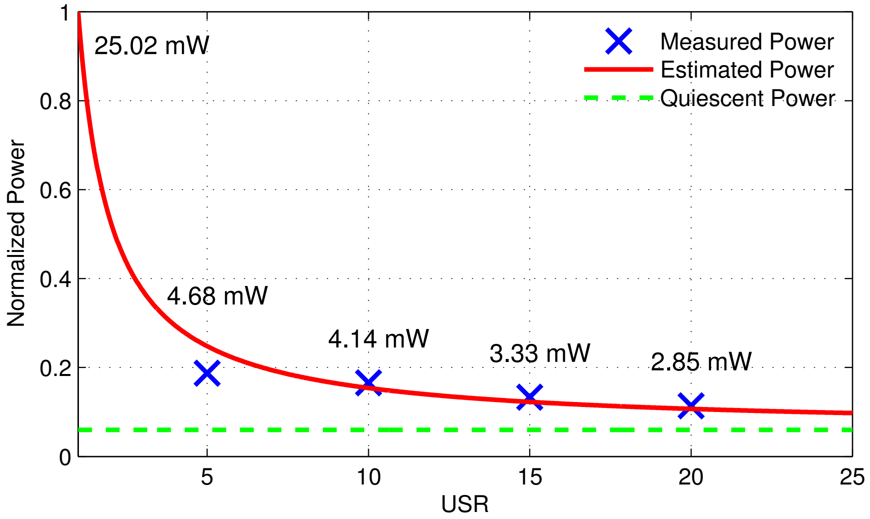

Figure 8.5: As the USR increases, the power consumption will approach the device's quiescent power. The actual measured power closely approximates the estimated power reduction based on the quiescent power and power consumption while Nyquist sampling.

In addition to consuming less power, systems which generate the measurement vector directly are less complex and easier to implement when compared to the existing compressed sensing framework. In this case, a sensing matrix is not used, reducing the memory requirements of the sensor node and removing the need for matrix multiplication. No preprocessing is needed. One can simply ”sub-sample, then send”.

Not only can this technique be used on signals which consume a large amount of power when generating the signal, it can be used when the ADC or the act of sampling consumes a large percentage of the device's power. Examples include high sample rate ECGs, or systems with many channels, such as an EEG or an implantable neural sensor array [169, 170]. While the exact amount of power savings will depend on the system and signal sparsity, the reduction in data rate is directly proportional to the USR.

8.6 Conclusion

This work has demonstrated for the first time in custom hardware, that compressed sensing can be used to sub-Nyquist sample the PPG. Compressed sensing can now reduce the power consumption of PPG analog-front-end circuitry without adding any complexity to the system, in addition to reducing the amount of data needed to represent the signal.

An overall power savings of 86.7% was achieved when sampling the PPG at a rate one fifteenth the Nyquist rate. This resulted in a NRMSD error of 4.26% an RMS error of 6.60%, and a foot error of 3.98 ms. By generating the measurement vector directly, the complexity of the sensor node is significantly reduced when compared to classic compressed sensing without sacrificing reconstruction accuracy.

Furthermore, weighted reconstruction increases the effectiveness of this compression by reducing the number of measurements needed for accurate reconstruction across subject populations and physiological states. This will be extended in future research by investigating custom physiological models to further increase the sparsity, and thus accuracy, of signal reconstruction.

The simple “sub-sample then send” paradigm has the possibility to effectively reduce the complexity of devices with a multitude of channels and minimize the power consumption when sampling a sparse signal. Future research will investigate the implementation of these methods on a large scale using devices with a large number of channels. The direct generation of the measurement vector and weighted reconstruction can be used in parallel with existing low-power technologies to create devices that achieve remarkably lower power consumption than is currently possible.

This has the potential to significantly improve the battery life of the FIT seat. The PPG alone results in over 75% of the device's overall power consumption. If the number of PPG samples can be reduced ten-fold, the battery life of the FIT seat can be improved from 8 months, to almost 2 years. This is a remarkable improvement that will help drive consumer adoption and patient compliance.

Chapter 9

Future Work and Final Remarks

9.1 Introduction

The present work details the design and verification of a revolutionary cardiovascular monitoring system incorporating commonly used medical instrumentation. The FIT seat has proven to be a robust cardiovascular monitoring device that can function unattended for months at a time. As this work lays the foundation for many future studies that can build upon the success of the present work. This chapter provides concluding remarks and details future studies and analyses, where the FIT seat can be used as a tool for automatic cardiovascular data acquisition. Additionally, the data captured herein as well as data captured throughout the course of future studies, can be used in the development and verification of algorithms utilizing machine learning.

9.2 Future Studies

9.2.1 In-Home Studies

Future in-home studies utilizing the FIT seat should be structured to investigate the systems ability to pick up trends, for both the normative and the heart failure populations. Normative and heart failure in-home studies can be run in parallel, where both subject groups should have the seat deployed in-home for a minimum of 90 days. This is recommended because it is the duration of the bundled payment provided to hospitals by the Centers for Medicare and Medicaid Service. Furthermore, over 40% of readmissions happen within the first 90 days after discharge.

This study should incorporate weekly visits for the in-lab testing of normative subjects, since they are expected to be mobile and do not have the physical limitations present in the heart-failure population. Gold standard measures captured during these visits will be used to verify the in-home trend results. Heart failure subject will not be able to participate in weekly visits, however their gold-standard measures can be updated during any hospital readmissions.

The normative population will demonstrate robust extraction of physiologic parameters, with the goal of tracking one's health. The heart failure population will demonstrate the ability of the FIT seat to predict outcome variables such as hospital readmissions, the need for a ventricular assist device, or death. The focus of this study should be to predict hospital readmissions, since the reduction of long-duration hospital readmissions have the greatest potential to positively impact the healthcare industry.

9.2.2 Posture Testing

One of the key challenges that will be faced with in-home deployment is automatic subject identification. Multiple individuals often use the same toilet in a household, and it is critical to only include data from a single individual when analyzing any FIT seat data, especially trend data over long periods of time. One of the most likely differentiating factors between subjects is body weight, which will require accurate weight estimation from the FIT seat measurements. This is a challenging problem because both posture and body type greatly impact the absolute weight present on the seat. Furthermore, slight differences in seating position for a subject can result in significantly different weight estimations from the FIT seat.

Machine learning techniques hold promise for robust weight and posture estimation using data from the four standoffs within the FIT seat. A posture based study will be required in order to gather training data for any machine learning based approach. The study should include a large number of subjects with different weights, heights, and body types. The more diverse the study population, the more accurate and robust the resultant weight estimation algorithm will be.

The posture based study will require each subject to partake in a single session, where multiple FIT seat recordings are taken at different pre-determined postures. Gold standard weight measurements can be used in combination with the pre-determined postures, to provide a training and verification set for machine learning based approaches. The result of this study will be an algorithm that accurately estimates weight, regardless of posture and body type, when deployed in the home or in the hospital.

9.2.3 Trend Studies

In order to further investigate the ability of the FIT seat to accurately extract blood pressure and weight, a study structured to verify trend data is required. A trend study is proposed, where gold-standard and FIT seat measurements are captured on a large number of subjects in a lab environment. There should be five measurements per subject each week, for a total of eight consecutive weeks.

Each subject will have a baseline measurement in the morning before consuming any stimulants, such as caffeine or nicotine. A maximum of two measurements should be taken each day, with at least four hours separation between measurements. The subject's blood pressure, heart rate, weight, and SpO_2 will be captured multiple times during a single session using hospital grade equipment. This data will allow the accuracy of the trends captured from the FIT seat to be quantitatively assessed across the normative population.

9.3 Future Analysis and Data Science

The data captured from the normative and heart-failure studies discussed in Chapter 5 can be hand annotated by trained experts. The resulting datasets, where each ECG and BCG feature is hand annotated, will facilitate the development and verification of advanced algorithms for use with the heart failure population and those with cardiovascular disease. Machine learning and other classification techniques can be used to identify features on ensemble averaged beats with unusual morphologies. This will also facilitate the automatic detection of arrhythmias, which is a critical feature of any cardiovascular monitoring system

The present and proposed studies have will result in a large amount of data and analyses. With accurate daily monitoring, the potential for diagnosis and prevention through prediction using advanced data science techniques is unmatched. Big data techniques utilizing in-home data can be used to predict outcome events and to provide automated diagnosis. This allows the long-term goal of the FIT seat to be realized, where the device can be deployed to one's home for unattended use. The system will continue to function independently, providing insight to the users about their health by recommending areas of improvement, providing early warning for potentially devastating events, and by automatically diagnosing subjects prior to any hospital visit or doctor checkup.

9.4 Conclusion

A fully integrated toilet seat for inconspicuous daily medical analysis has been presented. Novel algorithms have also been presented that fill in gaps within the current body of knowledge with state-of-the-art signal quality classification and delineation algorithms. The FIT seat hardware and algorithms have been verified using normative and heart failure human subject testing. Such a device has the potential to capture long-term trend data that has been previously unattainable, because it facilitates daily measurements taken at rest prior to the intake of food and stimulants at consistent times each day, with no required change in habit. This will enable new approaches and capabilities in the diagnosis and treatment of cardiovascular disease for those with heart failure and hypertension, as well as for those who are at risk of cardiotoxicity while undergoing chemotherapy treatments. There are no existing devices that has the capability to automatically and simultaneously acquire such an extensive and diverse set of measurements from a subject. The present algorithms enabling robust parameter extraction from the FIT seat, which would not be possible with the existing state-of-the-art. This device truly has the potential to revolutionize in-home cardiovascular health-care.

Bibliography

[1] Who.int. Who — cardiovascular diseases (cvds). http://www.who.int/mediacentre/factsheets/fs317/en/, 2015.

[2] Alan S Go, Dariush Mozaffarian, Véronique L Roger, Emelia J Benjamin, Jarett D Berry, Michael J Blaha, Shifan Dai, Earl S Ford, Caroline S Fox, Sheila Franco, et al. Heart disease and stroke statistics–2014 update: a report from the american heart association. *Circulation*, 129(3):e28, 2014.

[3] Centers for Medicare, Medicaid Services, et al. Cms to improve quality of care during hospital inpatient stays, 2015.

[4] Leslie R Martin, Summer L Williams, Kelly B Haskard, and M Robin DiMatteo. The challenge of patient adherence. *Therapeutics and clinical risk management*, 1(3):189, 2005.

[5] Nikolaos Dagres, Hans Kottkamp, Christopher Piorkowski, Sebastian Weis, Arash Arya, Philipp Sommer, Kerstin Bode, Jin-Hong Gerds-Li, Dimitrios Th Kremastinos, and Gerhard Hindricks. Influence of the duration of holter monitoring on the detection of arrhythmia recurrences after catheter ablation of atrial fibrillation: implications for patient follow-up. *International journal of cardiology*, 139(3):305–306, 2010.

[6] Eric B Bass, Edward I Curtiss, Vincent C Arena, Barbara H Hanusa, Alfred Cecchetti, Michael Karpf, and Wishwa N Kapoor. The duration of holter monitoring in patients with syncope: is 24 hours enough? *Archives of Internal Medicine*, 150(5):1073–1078, 1990.

[7] Heart.org. Holter monitor. http://www.heart.org/HEARTORG/Conditions/HeartAttack/SymptomsDiagnosisofHeartAttack/Holter-Monitor_UCM_446437_Article.jsp, 2015.

[8] John E Madias. The resting electrocardiogram in the management of patients with congestive heart failure: established applications and new insights. *Pacing and clinical electrophysiology*, 30(1):123–128, 2007.

[9] Erv Walter. Heart failure: Tracking weight changes - ewal.net. https://www.ewal.net/2013/01/13/heart-failure-tracking-weight-changes/, 2015.

[10] Wikipedia. Heart — Wikipedia, the free encyclopedia. http://en.wikipedia.org/w/index.php?title=Heart&oldid=739386861, 2016. [Online; accessed 21-September-2016].

[11] R. Plonsey and R.C. Barr. *Bioelectricity: a quantitative approach.* Springer Science+Business Media, LLC, 2007.

[12] Wikipedia. Electrical conduction system of the heart — Wikipedia, the free encyclopedia. http://en.wikipedia.org/w/index.php?title=Electrical%20conduction%20system%20of%20the%20heart&oldid=739034561, 2016. [Online; accessed 21-September-2016].

[13] Wikipedia. QRS complex — Wikipedia, the free encyclopedia. http://en.wikipedia.org/w/index.php?title=QRS%20complex&oldid=740174343, 2016. [Online; accessed 21-September-2016].

[14] David E. Ward. Electrocardiography: A physiologic approach. *Clinical Cardiology*, 17(5):283–283, 1994.

[15] Jaakko Malmivuo and Robert Plonsey. *Bioelectromagnetism: principles and applications of bioelectric and biomagnetic fields.* Oxford University Press, USA, 1995.

[16] L. Edenbrandt, A. Houston, and P.W. Macfarlane. Vectorcardiograms synthesized from 12-lead ecgs: A new method applied in 1792 healthy children. *Pediatric Cardiology*, 15(1):21–26, 1994.

[17] Y. Rudy, R. Plonsey, and J. Liebman. The effects of variations in conductivity and geometrical parameters on the electrocardiogram, using an eccentric spheres model. *Circulation Research*, 44(1):104–111, January 1979.

[18] R. Almeida, J.P. Martinez, A.P. Rocha, S. Olmos, and P. Laguna. Improved qt variability quantification by multilead automatic delineation. In *Computers in Cardiology, 2005*, pages 503–506, 2005.

[19] R Pallás-Areny, J Colominas-Balagué, and F J Rosell. The effect of respiration-induced heart movements on the ECG. *IEEE transactions on bio-medical engineering*, 36(6):585–90, June 1989.

[20] HC Burger and JBt Van Milaan. Heart-vector and leads. *British heart journal*, 8(3):157, 1946.

[21] HC Burger and JB Van Milaan. Heart-vector and leads. part ii. *British heart journal*, 9(3):154, 1947.

[22] Martin Burger and Joanna Tendera. Linear functionals in ecg and vcg. *Universitaet Muenster*, 2013.

[23] Ph Gabriel Steg, Stefan K James, Dan Atar, Luigi P Badano, Carina Blomstrom Lundqvist, Michael A Borger, Carlo Di Mario, Kenneth Dickstein, Gregory Ducrocq, Francisco Fernandez-Aviles, et al. Esc guidelines for the management of acute myocardial infarction in patients presenting with st-segment elevation. *European heart journal*, page ehs215, 2012.

[24] Yehuda Adler, Nili Zafrir, Tuvia Ben-Gal, Oren Ben Lulu, Charles Maynard, Samuel Sclarovsky, Ran Balicer, Aviv Mager, Boris Strasberg, Alejandro Solodky, et al. Relation between evolutionary st segment and t-wave direction and electrocardiographic prediction of mycardial infarct size and left ventricular function among patients with anterior wall q-wave acute myocardial infarction who received reperfusion therapy. *The American journal of cardiology*, 85(8):927–933, 2000.

[25] Susan Cheng, Michelle J Keyes, Martin G Larson, Elizabeth L McCabe, Christopher Newton-Cheh, Daniel Levy, Emelia J Benjamin, Ramachandran S Vasan, and Thomas J Wang. Long-term outcomes in individuals with prolonged pr interval or first-degree atrioventricular block. *Jama*, 301(24):2571–2577, 2009.

[26] Paul R. Forfia and Terence K. Trow. Diagnosis of pulmonary arterial hypertension. *Clinics in Chest Medicine*, 34(4):665 – 681, 2013. Pulmonary Arterial Hypertension.

[27] Marek Malik. Heart rate variability. *Annals of Noninvasive Electrocardiology*, 1(2):151–181, 1996.

[28] Ariel Diaz, Martial G Bourassa, Marie-Claude Guertin, and Jean-Claude Tardif. Long-term prognostic value of resting heart rate in patients with suspected or proven coronary artery disease. *European heart journal*, 26(10):967–974, 2005.

[29] Kim Fox, Jeffrey S Borer, A John Camm, Nicolas Danchin, Roberto Ferrari, Jose L Lopez Sendon, Philippe Gabriel Steg, Jean-Claude Tardif, Luigi Tavazzi, and Michal Tendera. Resting heart rate in cardiovascular disease. *Journal of the American College of Cardiology*, 50(9):823–830, 2007.

[30] Anders Opdahl, Bharath Ambale Venkatesh, Veronica RS Fernandes, Colin O Wu, Khurram Nasir, Eui-Young Choi, Andre LC Almeida, Boaz Rosen, Benilton Carvalho, Thor Edvardsen, et al. Resting heart rate as predictor for left ventricular dysfunction and heart failure: Mesa (multi-ethnic study of atherosclerosis). *Journal of the American College of Cardiology*, 63(12):1182–1189, 2014.

[31] Stefanie Hillebrand, Karin B Gast, Renée de Mutsert, Cees A Swenne, J Wouter Jukema, Saskia Middeldorp, Frits R Rosendaal, and Olaf M Dekkers. Heart rate variability and first cardiovascular event in populations without known cardiovascular disease: meta-analysis and dose–response meta-regression. *Europace*, 15(5):742–749, 2013.

[32] Phyllis K Stein, Matthew S Bosner, Robert E Kleiger, and Brooke M Conger. Heart rate variability: a measure of cardiac autonomic tone. *American heart journal*, 127(5):1376–1381, 1994.

[33] Hisako Tsuji, Martin G Larson, Ferdinand J Venditti, Emily S Manders, Jane C Evans, Charles L Feldman, and Daniel Levy. Impact of reduced heart rate variability on risk for cardiac events the framingham heart study. *Circulation*, 94(11):2850–2855, 1996.

[34] Takuya Taniguchi, Tatsuya Kawasaki, Nobuyuki Miyai, Tadaaki Kamitani, Shingo Kawasaki, and Hiroki Sugihara. [brain natriuretic peptide and qrs duration as a predictor for cardiac events in patients with heart failure]. *Journal of cardiology*, 47(6):277–283, 2006.

[35] Karl Swedberg, John Cleland, Henry Dargie, Helmut Drexler, Ferenc Follath, Michel Komajda, Luigi Tavazzi, Otto A Smiseth, Antonello Gavazzi, Axel Haverich, et al. Guidelines for the diagnosis and treatment of chronic heart failure: executive summary (update 2005). *European heart journal*, 26(11):1115–1140, 2005.

[36] Amir Kashani and S Serge Barold. Significance of qrs complex duration in patients with heart failure. *Journal of the American College of Cardiology*, 46(12):2183–2192, 2005.

[37] Roopinder Sandhu and Robert C Bahler. Prevalence of qrs prolongation in a community hospital cohort of patients with heart failure and its relation to left ventricular systolic dysfunction. *The American journal of cardiology*, 93(2):244–246, 2004.

[38] Paul R Kalra, Rakesh Sharma, Waqar Shamim, Wolfram Doehner, Roland Wensel, Aidan P Bolger, Sabine Genth-Zotz, Mariantonietta Cicoira, Andrew JS Coats, and Stefan D Anker. Clinical characteristics and survival of patients with chronic heart failure and prolonged qrs duration. *International journal of cardiology*, 86(2):225–231, 2002.

[39] Stephen Iuliano, Susan G Fisher, Pamela E Karasik, Ross D Fletcher, Steven N Singh, Department of Veterans Affairs Survival Trial of Antiarrhythmic Therapy in Congestive Heart Failure, et al. Qrs duration and mortality in patients with congestive heart failure. *American heart journal*, 143(6):1085–1091, 2002.

[40] Shen Luo, Kurt Michler, Paul Johnston, and Peter W Macfarlane. A comparison of commonly used qt correction formulae: the effect of heart rate on the qtc of normal ecgs. *Journal of electrocardiology*, 37:81–90, 2004.

[41] Bojan Vrtovec, Reynolds Delgado, Aly Zewail, Cynthia D Thomas, Barbara M Richartz, and Branislav Radovancevic. Prolonged qtc interval and high b-type natriuretic peptide levels together predict mortality in patients with advanced heart failure. *Circulation*, 107(13):1764–1769, 2003.

[42] Bernard Fermini and Anthony A Fossa. The impact of drug-induced qt interval prolongation on drug discovery and development. *Nature reviews Drug discovery*, 2(6):439–447, 2003.

[43] Dan M Roden. Drug-induced prolongation of the qt interval. *New England Journal of Medicine*, 350(10):1013–1022, 2004.

[44] Sofie AM Huybrechts, Daniel G Devos, Sebastian J Vermeersch, Dries Mahieu, Eric Achten, Tine LM de Backer, Patrick Segers, and Luc M van Bortel. Carotid to femoral pulse wave velocity: a comparison of real travelled aortic path lengths determined by mri and superficial measurements. *Journal of hypertension*, 29(8):1577–1582, 2011.

[45] Paolo Salvi, Giuseppe Lio, Carlos Labat, Enrico Ricci, Bruno Pannier, and Athanase Benetos. Validation of a new non-invasive portable tonometer for determining arterial pressure wave and pulse wave velocity: the pulsepen device. *Journal of hypertension*, 22(12):2285–2293, 2004.

[46] Gary F Mitchell. Pulse wave velocity measuring device, December 18 2001. US Patent 6,331,162.

[47] Devin B McCombie, Andrew T Reisner, and H Harry Asada. Adaptive blood pressure estimation from wearable ppg sensors using peripheral artery pulse wave velocity measurements and multi-channel blind identification of local arterial dynamics. In *Engineering in Medicine and Biology Society, 2006. EMBS'06. 28th Annual International Conference of the IEEE*, pages 3521–3524. IEEE, 2006.

[48] J Lass, IC Meigas, D Karai, R Kattai, J Kaik, and M Rossmann. Continuous blood pressure monitoring during exercise using pulse wave transit time measurement. In *Engineering in Medicine and Biology Society, 2004. IEMBS'04. 26th Annual International Conference of the IEEE*, volume 1, pages 2239–2242. IEEE, 2004.

[49] Youngzoon Yoon, Jung H Cho, and Gilwon Yoon. Non-constrained blood pressure monitoring using ecg and ppg for personal healthcare. *Journal of medical systems*, 33(4):261–266, 2009.

[50] Christer Ahlstrom, Anders Johansson, Fredrik Uhlin, Toste Länne, and Per Ask. Noninvasive investigation of blood pressure changes using the pulse wave transit time: a novel approach in the monitoring of hemodialysis patients. *Journal of Artificial Organs*, 8(3):192–197, 2005.

[51] Guanqun Zhang, Da Xu, N Bari Olivier, and Ramakrishna Mukkamala. Pulse arrival time is not an adequate surrogate for pulse transit time in terms of tracking diastolic pressure. In *2011 Annual International Conference of the IEEE Engineering in Medicine and Biology Society*, pages 6462–6464. IEEE, 2011.

[52] J Muehlsteff, XA Aubert, and G Morren. Continuous cuff-less blood pressure monitoring based on the pulse arrival time approach: The impact of posture. In *2008 30th Annual International Conference of the IEEE Engineering in Medicine and Biology Society*, pages 1691–1694. IEEE, 2008.

[53] Eduardo Pinheiro, Octavian Postolache, and Pedro Girao. Pulse arrival time and ballistocardiogram application to blood pressure variability estimation. In *Medical Measurements and Applications, 2009. MeMeA 2009. IEEE International Workshop on*, pages 132–136. IEEE, 2009.

[54] Eric S Winokur, David Da He, and Charles G Sodini. A wearable vital signs monitor at the ear for continuous heart rate and pulse transit time measurements. In *2012 Annual International Conference of the IEEE Engineering in Medicine and Biology Society*, pages 2724–2727. IEEE, 2012.

[55] Zhihao Chen, Xiufeng Yang, Ju Teng Teo, and Soon Huat Ng. Noninvasive monitoring of blood pressure using optical ballistocardiography and photoplethysmograph approaches. In *2013 35th Annual International Conference of the IEEE Engineering in Medicine and Biology Society (EMBC)*, pages 2425–2428. IEEE, 2013.

[56] Yan Li, C.C.Y. Poon, and Yuan-Ting Zhang. Analog integrated circuits design for processing physiological signals. *Biomedical Engineering, IEEE Reviews in*, 3:93–105, 2010.

[57] P Shi, S Hu, Y Zhu, J Zheng, Y Qiu, and PYS Cheang. Insight into the dicrotic notch in photoplethysmographic pulses from the finger tip of young adults. *Journal of medical engineering & technology*, 33(8):628–633, 2009.

[58] Wikipedia. Pulse oximetry — Wikipedia, the free encyclopedia. http://en.wikipedia.org/w/index.php?title=Pulse%20oximetry&oldid=737594236, 2016. [Online; accessed 21-September-2016].

[59] ISAAC STARR. Progress towards a physiological cardiology: A second essay on the ballistocardiogram. *Annals of Internal Medicine*, 63(6):1079–1105, 1965.

[60] Isaac Starr, AJ Rawson, HA Schroeder, and NR Joseph. Studies on the estimation of cardiac ouptut in man, and of abnormalities in cardiac function, from the heart's recoil and the blood's impacts; the ballistocardiogram. *American Journal of Physiology–Legacy Content*, 127(1):1–28, 1939.

[61] ISAAC STARR. Normal standards for amplitude of ballistocardiograms calibrated by force. *Circulation*, 11(6):914–926, 1955.

[62] Isaac Starr and Francis Clark Wood. Studies with the ballistocardiograph in acute cardiac infarction and chronic angina pectoris. *American Heart Journal*, 25(1):81–101, 1943.

[63] Isaac Starr. The relation of the ballistocardiogram to cardiac function. *The American journal of cardiology*, 2(6):737–747, 1958.

[64] Isaac Starr and Francis C Wood. Twenty-year studies with the ballistocardiograph the relation between the amplitude of the first record of" healthy" adults and eventual mortality and morbidity from heart disease. *Circulation*, 23(5):714–732, 1961.

[65] Edward W Bixby. A clinician's approach to the ballistocardiogram. *The American Journal of Cardiology*, 4(4):508–513, 1959.

[66] Laurent Giovangrandi, Omer T Inan, Richard M Wiard, Mozziyar Etemadi, and Gregory TA Kovacs. Ballistocardiographya method worth revisiting. In *Engineering in Medicine and Biology Society, EMBC, 2011 Annual International Conference of the IEEE*, pages 4279–4282. IEEE, 2011.

[67] D.D. He, E.S. Winokur, and C.G. Sodini. A continuous, wearable, and wireless heart monitor using head ballistocardiogram (bcg) and head electrocardiogram (ecg). In *Engineering in Medicine and Biology Society, EMBC, 2011 Annual International Conference of the IEEE*, pages 4729–4732, Aug 2011.

[68] OT Inan and GTA Kovacs. A low-noise ac-bridge amplifier for ballistocardiogram measurement on an electronic weighing scale. *Physiological measurement*, 31(7):N51, 2010.

[69] E.S. Winokur, D.D. He, and C.G. Sodini. A wearable vital signs monitor at the ear for continuous heart rate and pulse transit time measurements. In *Engineering in Medicine and Biology Society (EMBC), 2012 Annual International Conference of the IEEE*, pages 2724–2727, Aug 2012.

[70] OT Inan, M Etemadi, RM Wiard, L Giovangrandi, and GTA Kovacs. Robust ballistocardiogram acquisition for home monitoring. *Physiological measurement*, 30(2):169, 2009.

[71] DENNIS C DEUCHAR, SAMUEL A TALBOT, and Wm R Scarborough. Some observations on the relation of the high-frequency bed ballistocardiogram to that obtained from an aperiodic bed. *Circulation*, 11(2):228–239, 1955.

[72] Omer T Inan, Mozziyar Etemadi, Richard M Wiard, Gregory T a Kovacs, and Laurent Giovangrandi. Non-invasive measurement of Valsalva-induced hemodynamic changes on a bathroom scale ballistocardiograph. *Conference proceedings : ... Annual International Conference of the IEEE Engineering in Medicine and Biology Society. IEEE Engineering in Medicine and Biology Society. Conference*, 2008:674–7, January 2008.

[73] Jung Soo Kim, Young Joon Chee, Ju Wan Park, Jin Wook Choi, and Kwang Suk Park. A new approach for non-intrusive monitoring of blood pressure on a toilet seat. *Physiological measurement*, 27(2):203, 2006.

[74] JH Shin, GS Chung, KK Kim, JS Kim, BS Hwang, and KS Park. Ubiquitous house and unconstrained monitoring devices for home healthcare system. In *2007 6th International Special Topic Conference on Information Technology Applications in Biomedicine*, pages 201–204. IEEE, 2007.

[75] T Schlebusch. Unobtrusive health screening on an intelligent toilet seat. *Acta Polytechnica*, 51(5), 2011.

[76] Hyun Jae Baek, Jung Soo Kim, Ko Keun Kim, and Kwang Suk Park. System for unconstrained ecg measurement on a toilet seat using capacitive coupled electrodes: the efficacy and practicality. In *2008 30th Annual International Conference of the IEEE Engineering in Medicine and Biology Society*, pages 2326–2328. IEEE, 2008.

[77] Ko Keun Kim, Yong Kyu Lim, and Kwang Suk Park. The electrically noncontacting ecg measurement on the toilet seat using the capacitively-coupled insulated electrodes. In *Engineering in Medicine and Biology Society, 2004. IEMBS'04. 26th Annual International Conference of the IEEE*, volume 1, pages 2375–2378. IEEE, 2004.

[78] Tatsuo Togawa, Toshiyo Tamura, Jianxin Zhou, Hiroshi Mizukami, and Masayuki Ishijima. Physiological monitoring systems attached to the bed and sanitary equipments. In *Engineering in Medicine and Biology Society, 1989. Images of the Twenty-First Century., Proceedings of the Annual International Conference of the IEEE Engineering in*, pages 1461–1463. IEEE, 1989.

[79] Kwang Suk Park. Nonintrusive measurement of biological signals for ubiquitous healthcare. In *2009 Annual International Conference of the IEEE Engineering in Medicine and Biology Society*, pages 6573–6575. IEEE, 2009.

[80] JS Kim, JW Park, MS Ryu, and KS Park. Multi-channel measurement of photoplethysmography and evaluation for the optimal site of a thigh in a toilet. In *Engineering in Medicine and Biology Society, 2004. IEMBS'04. 26th Annual International Conference of the IEEE*, volume 2, pages 3366–3368. IEEE, 2004.

[81] Hui Fang Huang, Guang Shu Hu, and Li Zhu. Sparse representation-based heartbeat classification using independent component analysis. *Journal of medical systems*, 36(3):1235–47, June 2012.

[82] S Tanaka, M Nogawa, and K Yamakoshi. Fully automatic system for monitoring blood pressure from a toilet-seat using the volume-oscillometric method. In *2005 IEEE Engineering in Medicine and Biology 27th Annual Conference*, pages 3939–3941. IEEE, 2006.

[83] Jung Soo Kim, Young Joon Chee, Ju Wan Park, Jin Wook Choi, and Kwang Suk Park. A new approach for non-intrusive monitoring of blood pressure on a toilet seat. *Physiological measurement*, 27(2):203, 2006.

[84] Mitsuhiro Ogawa, Toshiyo Tamura, and Tatsuo Togawa. Fully automated biosignal acquisition in daily routine through 1 month. In *Engineering in Medicine and Biology Society, 1998. Proceedings of the 20th Annual International Conference of the IEEE*, volume 4, pages 1947–1950. IEEE, 1998.

[85] K Yamakoshi, M Kuroda, S Tanaka, I Yamaguchi, and A Kawarada. Non-conscious and automatic acquisition of body and excreta weight together with ballistocardiogram in a lavatory. In *Engineering in Medicine and Biology Society, 1996. Bridging*

Disciplines for Biomedicine. Proceedings of the 18th Annual International Conference of the IEEE, volume 1, pages 67–68. IEEE, 1996.

[86] Refik Hadzialic. Diy heart monitoring device (simple ecg), 2015.

[87] J. Rosell, J. Colominas, P. Riu, R. Pallas-Areny, and J.G. Webster. Skin impedance from 1 hz to 1 mhz. *Biomedical Engineering, IEEE Transactions on*, 35(8):649–651, Aug 1988.

[88] M.M. Puurtinen, S.M. Komulainen, P.K. Kauppinen, J.A.V. Malmivuo, and J.A.K. Hyttinen. Measurement of noise and impedance of dry and wet textile electrodes, and textile electrodes with hydrogel. In *Engineering in Medicine and Biology Society, 2006. EMBS '06. 28th Annual International Conference of the IEEE*, pages 6012–6015, Aug 2006.

[89] Y.M. Chi, Tzyy-Ping Jung, and G. Cauwenberghs. Dry-contact and noncontact biopotential electrodes: Methodological review. *Biomedical Engineering, IEEE Reviews in*, 3:106–119, 2010.

[90] J.G. Webster. *Design of Pulse Oximeters*. Series in Medical Physics and Biomedical Engineering. CRC Press, 1997.

[91] K Li and S Warren. A wireless reflectance pulse oximeter with digital baseline control for unfiltered photoplethysmograms. *IEEE transactions on biomedical circuits and systems*, 6(3):269–78, June 2012.

[92] Gazi Maruf Azmal, Adel Al-Jumaily, et al. Continuous measurement of oxygen saturation level using photoplethysmography signal. In *2006 International Conference on Biomedical and Pharmaceutical Engineering*, pages 504–507. IEEE, 2006.

[93] Texas Instruments. Msp430fr59xx mixed-signal microcontrollers. http://www.ti.com/lit/ds/symlink/msp430fr5969.pdf, March 2015.

[94] Micropower, 3-axis, digital output mems accelerometer. http://www.analog.com/media/en/technical-documentation/data-sheets/ADXL362.pdf, 2014.

[95] Jeff Rowberg. Bgscript: min current - low power baseline reference project. https://bluegiga.zendesk.com/entries/24740576-BGScript-min-current-Low-power-baseline-reference-project, 2015.

[96] Texas Instruments. 1-mhz, micro-power, low-noise, rrio,1.8-v cmos operational amplifier precision value line series. http://www.ti.com/lit/ds/symlink/opa313.pdf, January 2006.

[97] Texas Instruments. micropower, single-supply, cmos instrumentation amplifier. http://www.ti.com/lit/ds/symlink/ina2321.pdf, March 2013.

[98] Qiao Li, Roger G Mark, and Gari D Clifford. Robust heart rate estimation from multiple asynchronous noisy sources using signal quality indices and a kalman filter. *Physiological measurement*, 29(1):15, 2007.

[99] B Aldecoa Sánchez del Río, T Lopetegi, and I Romero. Assessment of different methods to estimate electrocardiogram signal quality. In *2011 Computing in Cardiology*, pages 609–612. IEEE, 2011.

[100] LN Sharma, S Dandapat, and A Mahanta. Kurtosis based multichannel ecg signal denoising and diagnostic distortion measures. In *TENCON 2009-2009 IEEE Region 10 Conference*, pages 1–5. IEEE, 2009.

[101] Taigang He, Gari Clifford, and Lionel Tarassenko. Application of independent component analysis in removing artefacts from the electrocardiogram. *Neural Computing & Applications*, 15(2):105–116, 2006.

[102] J Pan and W J Tompkins. A real-time QRS detection algorithm. *IEEE transactions on bio-medical engineering*, 32(3):230–6, March 1985.

[103] George B Moody and Roger G Mark. The impact of the mit-bih arrhythmia database. *Engineering in Medicine and Biology Magazine, IEEE*, 20(3):45–50, 2001.

[104] A Taddei, G Distante, M Emdin, P Pisani, GB Moody, C Zeelenberg, and C Marchesi. The european st-t database: standard for evaluating systems for the analysis of st-t changes in ambulatory electrocardiography. *European heart journal*, 13(9):1164–1172, 1992.

[105] Ary L. Goldberger, Luis A. N. Amaral, Leon Glass, Jeffrey M. Hausdorff, Plamen Ch. Ivanov, Roger G. Mark, Joseph E. Mietus, George B. Moody, Chung-Kang Peng, and H. Eugene Stanley. Physiobank, physiotoolkit, and physionet: Components of a new research resource for complex physiologic signals. *Circulation*, 101(23):e215–e220, 2000.

[106] Juan Pablo Martínez, Rute Almeida, Salvador Olmos, Ana Paula Rocha, and Pablo Laguna. A wavelet-based ecg delineator: evaluation on standard databases. *IEEE Transactions on biomedical engineering*, 51(4):570–581, 2004.

[107] J.P. Martinez, R. Almeida, S. Olmos, A.P. Rocha, and P. Laguna. A wavelet-based ecg delineator: evaluation on standard databases. *Biomedical Engineering, IEEE Transactions on*, 51(4):570–581, 2004.

[108] M Bahoura, M Hassani, and M Hubin. Dsp implementation of wavelet transform for real time ecg wave forms detection and heart rate analysis. *Computer methods and programs in biomedicine*, 52(1):35–44, 1997.

[109] Cuiwei Li, Chongxun Zheng, and C Tai. Detection of ECG characteristic points using wavelet transforms. *Biomedical Engineering, IEEE . . .*, 42(1), 1995.

[110] Dorthe B Saadi, George Tanev, Morten Flintrup, Armin Osmanagic, Kenneth Egstrup, Karsten Hoppe, Poul Jennum, Jørgen L Jeppesen, Helle K Iversen, and Helge BD Sorensen. Automatic real-time embedded qrs complex detection for a novel patch-type electrocardiogram recorder. *IEEE journal of translational engineering in health and medicine*, 3:1–12, 2015.

[111] Arturo Martínez, Raúl Alcaraz, and José Joaquín Rieta. Application of the phasor transform for automatic delineation of single-lead ecg fiducial points. *Physiological measurement*, 31(11):1467, 2010.

[112] Luigi Y Di Marco and Lorenzo Chiari. A wavelet-based ecg delineation algorithm for 32-bit integer online processing. *Biomedical engineering online*, 10(1):1, 2011.

[113] Cuiwei Li, Chongxun Zheng, and Changfeng Tai. Detection of ecg characteristic points using wavelet transforms. *Biomedical Engineering, IEEE Transactions on*, 42(1):21–28, Jan 1995.

[114] Jiapu Pan and Willis J. Tompkins. A real-time qrs detection algorithm. *Biomedical Engineering, IEEE Transactions on*, BME-32(3):230–236, 1985.

[115] Falco Strasser, Michael Muma, and Abdelhak M Zoubir. Motion artifact removal in ecg signals using multi-resolution thresholding. In *Signal Processing Conference (EUSIPCO), 2012 Proceedings of the 20th European*, pages 899–903. IEEE, 2012.

[116] Lisheng Xu, David Zhang, and Kuanquan Wang. Wavelet-based cascaded adaptive filter for removing baseline drift in pulse waveforms. *IEEE transactions on bio-medical engineering*, 52(11):1973–5, November 2005.

[117] Umar Farooq, Dae-Geun Jang, Jang-Ho Park, and Seung-Hun Park. PPG delineator for real-time ubiquitous applications. *Conference proceedings : ... Annual International Conference of the IEEE Engineering in Medicine and Biology Society. IEEE Engineering in Medicine and Biology Society. Conference*, 2010:4582–5, January 2010.

[118] W. Zong, T. Heldt, G.B. Moody, and R.G. Mark. An open-source algorithm to detect onset of arterial blood pressure pulses. *Computers in Cardiology, 2003*, pages 259–262, 2003.

[119] Mateo Aboy, James McNames, Tran Thong, Daniel Tsunami, Miles S Ellenby, and Brahm Goldstein. An automatic beat detection algorithm for pressure signals. *IEEE transactions on bio-medical engineering*, 52(10):1662–70, October 2005.

[120] Bing Nan Li, Ming Chui Dong, and Mang I. Vai. On an automatic delineator for arterial blood pressure waveforms. *Biomedical Signal Processing and Control*, 5(1):76–81, January 2010.

[121] Maikel Noriega, Juan Pablo Martínez, Pablo Laguna, Raquel Bailón, and Rute Almeida. Respiration effect on wavelet-based ECG T-wave end delineation strategies. *IEEE transactions on bio-medical engineering*, 59(7):1818–28, July 2012.

[122] HY Wu, Michael Rubinstein, and Eugene Shih. Eulerian video magnification for revealing subtle changes in the world. *ACM Transactions on . . .* , 2012.

[123] Lluis Capdevila, Jordi Moreno, Javier Movellan, Eva Parrado, and Juan Ramos-Castro. HRV based health&sport markers using video from the face. *Conference proceedings : ... Annual International Conference of the IEEE Engineering in Medicine and Biology Society. IEEE Engineering in Medicine and Biology Society. Conference*, 2012:5646–9, January 2012.

[124] Jeffrey B Bolkhovsky, Christopher G Scully, and Ki H Chon. Statistical analysis of heart rate and heart rate variability monitoring through the use of smart phone cameras. *Conference proceedings : ... Annual International Conference of the IEEE Engineering in Medicine and Biology Society. IEEE Engineering in Medicine and Biology Society. Conference*, 2012:1610–3, January 2012.

[125] ILAN Goldenberg, Arthur J Moss, Wojciech Zareba, et al. Qt interval: how to measure it and what is" normal". *Journal of cardiovascular electrophysiology*, 17(3):333–336, 2006.

[126] NB McLaughlin, RW Campbell, and A Murray. Accuracy of four automatic qt measurement techniques in cardiac patients and healthy subjects. *Heart*, 76(5):422–426, 1996.

[127] RA Payne, CN Symeonides, DJ Webb, and SRJ Maxwell. Pulse transit time measured from the ecg: an unreliable marker of beat-to-beat blood pressure. *Journal of Applied Physiology*, 100(1):136–141, 2006.

[128] Heiko Gesche, Detlef Grosskurth, Gert Küchler, and Andreas Patzak. Continuous blood pressure measurement by using the pulse transit time: comparison to a cuff-based method. *European journal of applied physiology*, 112(1):309–315, 2012.

[129] CCY Poon and YT Zhang. Cuff-less and noninvasive measurements of arterial blood pressure by pulse transit time. In *2005 IEEE Engineering in Medicine and Biology 27th Annual Conference*, pages 5877–5880. IEEE, 2006.

[130] Alexander S Liberson, Jeffrey S Lillie, Steven W Day, and David A Borkholder. A physics based approach to the pulse wave velocity prediction in compliant arterial segments. *Journal of Biomechanics*, 2016.

[131] Jeffrey S Lillie, Alexander S Liberson, and David A Borkholder. Quantification of hemodynamic pulse wave velocity based on a thick wall multi-layer model for blood vessels. *Journal of Fluid Flow*, 3, 2016.

[132] Jeffrey S Lillie, Alexander S Liberson, Doran Mix, Karl Q Schwarz, Ankur Chandra, Daniel B Phillips, Steven W Day, and David A Borkholder. Pulse wave velocity prediction and compliance assessment in elastic arterial segments. *Cardiovascular engineering and technology*, 6(1):49–58, 2015.

[133] Alexander S Liberson, Jeffrey S Lillie, and David A Borkholder. Numerical solution for the boussinesq type models with application to arterial flow. *Journal of Fluid Flow*, 1, 2014.

[134] Association for the Advancement of Medical Instrumentation et al. American national standard: electronic or automated sphygmomanometers. *Washington, DC: AAMI*, 1987.

[135] Marcel Ruzicka, Ayub Akbari, Eva Bruketa, Jeanne Françoise Kayibanda, Claude Baril, and Swapnil Hiremath. How accurate are home blood pressure devices in use? a cross-sectional study. *PloS one*, 11(6):e0155677, 2016.

[136] D.L. Donoho and Y. Tsaig. Recent advances in sparsity-driven signal recovery. In *Acoustics, Speech, and Signal Processing, 2005. Proceedings. (ICASSP '05). IEEE International Conference on*, volume 5, pages v/713 – v/716 Vol. 5, march 2005.

[137] D.L. Donoho. Compressed sensing. *Information Theory, IEEE Transactions on*, 52(4):1289 –1306, april 2006.

[138] E.J. Candes and T. Tao. Near-optimal signal recovery from random projections: Universal encoding strategies? *Information Theory, IEEE Transactions on*, 52(12):5406 –5425, dec. 2006.

[139] Emmanuel J. Candes, Justin K. Romberg, and Terence Tao. Stable signal recovery from incomplete and inaccurate measurements. *Communications on Pure and Applied Mathematics*, 59(8):1207–1223, 2006.

[140] E.J. Candes, J. Romberg, and T. Tao. Robust uncertainty principles: exact signal reconstruction from highly incomplete frequency information. *Information Theory, IEEE Transactions on*, 52(2):489 – 509, feb. 2006.

[141] M. Balouchestani. Low-power wireless sensor network with compressed sensing theory. In *Fly by Wireless Workshop (FBW), 2011 4th Annual Caneus*, pages 1–4, June 2011.

[142] a M R Dixon, E G Allstot, D Gangopadhyay, and D J Allstot. Compressed Sensing System Considerations for ECG and EMG Wireless Biosensors. *IEEE transactions on biomedical circuits and systems*, 6(2):156–66, April 2012.

[143] E.J. Candes and M.B. Wakin. An introduction to compressive sampling. *Signal Processing Magazine, IEEE*, 25(2):21 –30, march 2008.

[144] F. Chen, A.P. Chandrakasan, and V.M. Stojanovic. Design and analysis of a hardware-efficient compressed sensing architecture for data compression in wireless sensors. *Solid-State Circuits, IEEE Journal of*, 47(3):744–756, March 2012.

[145] J.N. Laska, S. Kirolos, M.F. Duarte, T.S. Ragheb, R.G. Baraniuk, and Y. Massoud. Theory and implementation of an analog-to-information converter using random demodulation. In *Circuits and Systems, 2007. ISCAS 2007. IEEE International Symposium on*, pages 1959–1962, May 2007.

[146] M. Mishali, Y.C. Eldar, O. Dounaevsky, and E. Shoshan. Xampling: analog to digital at sub-Nyquist rates. *IET Circuits, Devices & Systems*, 5(1):8, 2011.

[147] M. Mishali and Y.C. Eldar. From theory to practice: Sub-nyquist sampling of sparse wideband analog signals. *Selected Topics in Signal Processing, IEEE Journal of*, 4(2):375–391, April 2010.

[148] H. Mamaghanian, N. Khaled, D. Atienza, and P. Vandergheynst. Design and exploration of low-power analog to information conversion based on compressed sensing. *Emerging and Selected Topics in Circuits and Systems, IEEE Journal on*, 2(3):493–501, Sept 2012.

[149] Akanksha Mishra, Falgun N. Thakkar, Chintan Modi, and Rahul Kher. Selecting the Most Favorable Wavelet for Compressing ECG Signals Using Compressive Sensing Approach. *2012 International Conference on Communication Systems and Network Technologies*, pages 128–132, May 2012.

[150] E.G. Allstot, A.Y. Chen, A.M.R. Dixon, D. Gangopadhyay, and D.J. Allstot. Compressive sampling of ecg bio-signals: Quantization noise and sparsity considerations. In *Biomedical Circuits and Systems Conference (BioCAS), 2010 IEEE*, pages 41 –44, nov. 2010.

[151] H. Mamaghanian, N. Khaled, D. Atienza, and P. Vandergheynst. Compressed sensing for real-time energy-efficient ecg compression on wireless body sensor nodes. *Biomedical Engineering, IEEE Transactions on*, 58(9):2456 –2466, sept. 2011.

[152] K Kanoun, H Mamaghanian, N Khaled, and D Atienza. A real-time compressed sensing-based personal electrocardiogram monitoring system. *2011 Design, Automation & Test in Europe*, pages 1–6, March 2011.

[153] L.F. Polania, R.E. Carrillo, M. Blanco-Velasco, and K.E. Barner. Compressed sensing based method for ecg compression. In *Acoustics, Speech and Signal Processing (ICASSP), 2011 IEEE International Conference on*, pages 761 –764, may 2011.

[154] Selin Aviyente. Compressed sensing framework for eeg compression. In *Statistical Signal Processing, 2007. SSP '07. IEEE/SP 14th Workshop on*, pages 181 –184, aug. 2007.

[155] Zhilin Zhang, Tzyy-Ping Jung, Scott Makeig, and Bhaskar D Rao. Compressed sensing of EEG for wireless telemonitoring with low energy consumption and inexpensive hardware. *IEEE transactions on bio-medical engineering*, 60(1):221–4, January 2013.

[156] P.K. Baheti and H. Garudadri. An ultra low power pulse oximeter sensor based on compressed sensing. In *Wearable and Implantable Body Sensor Networks, 2009. BSN 2009. Sixth International Workshop on*, pages 144 –148, june 2009.

[157] Pawan K. Baheti, Harinath Garudadri, and Somdeb Majumdar. Blood oxygen estimation from compressively sensed photoplethysmograph. In *Wireless Health 2010*, WH '10, pages 10–14, New York, NY, USA, 2010. ACM.

[158] M. Tavakoli, L. Turicchia, and R. Sarpeshkar. An ultra-low-power pulse oximeter implemented with an energy-efficient transimpedance amplifier. *Biomedical Circuits and Systems, IEEE Transactions on*, 4(1):27–38, Feb 2010.

[159] K Glaros and E.M. Drakakis. A sub-mw fully-integrated pulse oximeter front-end. *Biomedical Circuits and Systems, IEEE Transactions on*, 7(3):363–375, 2013.

[160] Alan V. Oppenheim, Ronald W. Schafer, and John R. Buck. *Discrete-time signal processing (2nd ed.)*. Prentice-Hall, Inc., Upper Saddle River, NJ, USA, 1999.

[161] Emily G. Allstot, Andrew Y. Chen, Anna M. R. Dixon, Daibashish Gangopadhyay, Heather Mitsuda, and David J. Allstot. Compressed sensing of ECG bio-signals using one-bit measurement matrices. *2011 IEEE 9th International New Circuits and systems conference*, pages 213–216, June 2011.

[162] Anna M.R. Dixon, Emily G. Allstot, Andrew Y. Chen, Daibashish Gangopadhyay, and David J. Allstot. Compressed sensing reconstruction: Comparative study with applications to ECG bio-signals. *2011 IEEE International Symposium of Circuits and Systems (ISCAS)*, pages 805–808, May 2011.

[163] D. Angelosante, G.B. Giannakis, and E. Grossi. Compressed sensing of time-varying signals. In *Digital Signal Processing, 2009 16th International Conference on*, pages 1 –8, july 2009.

[164] Nicholas J. Conn and David Borkholder. A comparison of reconstruction methods for compressed sensing of the photoplethysmogram. In *10th international conference on Sampling Theory and Applications (SampTA 2013)*, pages 204–207, Bremen, Germany, July 2013.

[165] Nicholas J. Conn and David A. Borkholder. Wavelet based photoplethysmogram foot delineation for heart rate variability applications. In *Signal Processing in Medicine and Biology Symposium (SPMB), 2013 IEEE*, pages 1–5, Dec 2013.

[166] Texas Instruments. Integrated analog front-end for pulse oximeters. http://www.ti.com/lit/ds/symlink/afe4490.pdf, May 2013.

[167] John Allen. Photoplethysmography and its application in clinical physiological measurement. *Physiological measurement*, 28(3):R1–39, March 2007.

[168] Daniel Torres. Build a wrist heart-rate monitor using an ultra-low-power mcu. *Electronic Design*, July 2013.

[169] M. Fereniec, M. Kacprzak, R. Maniewski, A. ZbieC, and D. Ircha. The 64 channel system for high resolution ecg mapping. In *Computers in Cardiology 2001*, pages 513–515, 2001.

[170] C.M. Lopez, A. Andrei, S. Mitra, M. Welkenhuysen, W. Eberle, C. Bartic, R. Puers, R.F. Yazicioglu, and G.G.E. Gielen. An implantable 455-active-electrode 52-channel cmos neural probe. *Solid-State Circuits, IEEE Journal of*, 49(1):248–261, Jan 2014.